การไหลที่มีผิวอิสระผ่านสิ่งกีดขวางใต้น้ำ

ว่าที่ร้อยโท ภณัฐ ก้วยเจริญพานิชก์

FREE-SURFACE FLOWS OVER SUBMERGED OBSTACLES

Acting Lt. Panat Guayjarernpanishk

A Dissertation Submitted in Partial Fulfillment of the Requirements

for the Degree of Doctor of Philosophy Program in Mathematics

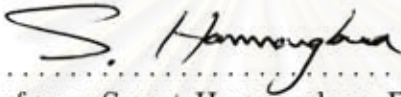Department of Mathematics

Faculty of Science
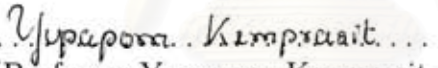
Chulalongkorn University
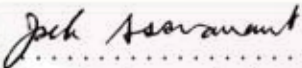
Academic Year 2008

Thesis Title   FREE-SURFACE FLOWS OVER SUBMERGED OBSTACLES

By   Acting Lt. Panat Guayjarernpanishk

Field of Study   Mathematics

Advisor   Associate Professor Jack Asavanant, Ph.D.

Accepted by the Faculty of Science, Chulalongkorn University in Partial Fulfillment of the Requirements for the Doctoral Degree

.... Dean of the Faculty of Science
(Professor Supot Hannongbua, Dr.rer.nat.)

THESIS COMMITTEE

.... Chairman
(Professor Yupaporn Kemprasit, Ph.D.)

.... Advisor
(Associate Professor Jack Asavanant, Ph.D.)

.... Examiner
(Assistant Professor Songkiat Sumetkijakan, Ph.D.)

.... Examiner
(Khamron Mekchay, Ph.D.)

.... External Examiner
(Associate Professor Ekachai Juntasaro, Ph.D.)

ภณัฐ ก้วยเจริญพานิชก์ :   การไหลที่มีผิวอิสระผ่านสิ่งกีดขวางใต้น้ำ.
(FREE-SURFACE FLOWS OVER SUBMERGED OBSTACLES)
อ.ที่ปรึกษาวิทยานิพนธ์หลัก : รศ. ดร. จักษ์ อัศวานันท์, 124 หน้า.

เราพิจารณาการไหลที่มีผิวอิสระผ่านสิ่งกีดขวางใต้น้ำ ภายใต้ผลกระทบของแรงโน้มถ่วง และแรงตึงผิว ของไหลที่พิจารณาเป็นของไหลที่ไม่มีความหนืด และไม่มีการบีบอัดตัว สมมติ-ฐานเกี่ยวกับการไหล คือ การไหลเป็นการไหลแบบสม่ำเสมอ ใน 2 มิติ และไม่มีการหมุนวน การไหลจะถูกจำแนกโดยพารามิเตอร์ต่อไปนี้ คือ Froude number F Bond number Bo ระยะ-ห่างระหว่างสิ่งกีดขวาง x_d และความสูงของสิ่งกีดขวาง hob ปัญหาไม่เชิงเส้นอย่างเต็มรูปถูกแก้ด้วยวิธีเชิงตัวเลข โดยใช้ เทคนิคของสมการปริพันธ์เชิงขอบ หลังจากการเปลี่ยนปัญหาให้เป็นแบบภินทนะแล้ว   เราสามารถหาคำตอบของระบบสมการพีชคณิตแบบไม่เชิงเส้นนี้ด้วยระเบียบวิธีของนิวตัน นอกจากนี้เรายังได้ศึกษาปัญหาไม่เชิงเส้นอย่างอ่อนของการไหลแบบสม่ำเสมอ และการไหลที่ขึ้นกับเวลา และคำตอบของปัญหาดังกล่าวนี้ได้ถูกนำมาเปรียบเทียบกับคำตอบของปัญ-หาไม่เชิงเส้นอย่างเต็มรูป   ในงานวิทยานิพนธ์นี้ได้รวบรวมคำตอบของปัญหาการไหลผ่านสิ่งกีด-ขวางหนึ่งสิ่งในรูปของแผนผังของคำตอบสำหรับสิ่งกีดขวางที่มีความสูงเป็น บวก และ ลบ บน-ระนาบ (F, hob) และได้นำเสนอคำตอบรูปแบบใหม่ของการไหลผ่านสิ่งกีดขวางสองสิ่ง

ภาควิชา คณิตศาสตร์   ลายมือชื่อนิสิต ....
สาขาวิชา คณิตศาสตร์   ลายมือชื่ออ.ที่ปรึกษาวิทยานิพนธ์หลัก ....
ปีการศึกษา 2551

4773827523 : MAJOR MATHEMATICS
KEYWORDS: FREE-SURFACE FLOW / OBSTACLE / BOUNDARY INTE-GRAL EQUATION TECHNIQUE / SURFACE TENSION / fKdV / PSEU-DOSPECTRAL METHOD

PANAT GUAYJARERNPANISHK: FREE-SURFACE FLOWS OVER SUBMERGED OBSTACLES. ADVISOR: ASSOC. PROF. JACK ASA-VANANT, Ph.D., 124 pp.

We consider free-surface flows over submerged obstacles under the effects of gravity and surface tension. The fluid is treated as inviscid and incompressible. The flow is assumed to be steady, two-dimensional, and irrotational. The flow is characterized by the following parameters: Froude number F, Bond number Bo, distance between the obstacles x_d, and height of the obstacles hob. Fully nonlinear problem is solved numerically by using the boundary integral equation technique. After the discretization, we obtain a system of nonlinear algebraic equations which can be solved by the Newton's method. In addition, the weakly nonlinear problem of steady and time-dependent flows are investigated and compared with the fully nonlinear results. In this thesis, special case of flows over a single obstacle is summarized in the solution diagram of (F, hob)-plane for bump ($hob > 0$) and dip ($hob < 0$). New family of solutions of free-surface flows over two obstacles are proposed.

Department: **Mathematics**

Field of Study: **Mathematics**

Academic Year: **2008**

Student's Signature Panat. Guayjarernpanishk.

Advisor's Signature .... Jack Asavanant

ACKNOWLEDGEMENTS

CONTENTS

LIST OF TABLES

LIST OF FIGURES

CHAPTER I

INTRODUCTION

Flow over submerged obstacles is one of the classical problems in fluid mechanics. It concerns several related physical applications ranging from the flow of water over rocks to atmospheric/oceanic stratified flows encountering topographic obstacles, or even a moving pressure distribution on a free surface.

Free surface flows over an obstacle have been investigated by many researchers for various bottom topography. Lamb [42] considered linear problem of free-surface flow over a submerged semi-elliptical obstacle. He obtained solutions with a train of waves on the downstream for subcritical flow and solutions without waves for supercritical flow. Forbes and Schwartz [27] used the boundary integral method to find fully nonlinear solutions of subcritical and supercritical flows over a semi-circular obstacle. Their findings confirmed and extended the previous results of Lamb. Forbes [23] computed numerical solutions of critical flow over a semi-circular obstacle for which the flow was in subcritical regime ahead of the obstacle and supercritical regime behind the obstacle. This type of solution is generally referred as "hydraulic fall". Vanden-Broeck [60] showed numerically that there exist two types of supercritical flow for which the first type of solution corresponds to those obtained by the perturbation of uniform flow, and the other by the perturbation of solitary wave. Both profiles were symmetric with respect to the obstacle. Supercritical and critical flows over a submerged triangular obstacle were investigated by Dias and Vanden-Broeck [17]. They employed a series

truncation technique and calculated numerically the solutions. They illustrated, for critical regime, that the flow behavior near the apex of the triangle was similar to the flow over a wedge as the size of the triangle increases to the limiting case. They also conjectured, for supercritical regime, that the flow could approach a limiting configuration with a stagnation point on the free surface with a 120° angle.

Shen *et al.* [57], Shen and Shen [56] and Shen [55] studied weakly nonlinear problem of stationary solutions of flow over an obstacle. Like in the fully nonlinear problem, they found two branches of solutions for supercritical flow and showed that Forbes's solution [23] was a limit of the cnoidal wave solution. Zhang and Zhu [66] proposed a model based on a nonlinear integral equation in terms of hodograph variables for free-surface flow over an arbitrary bottom obstruction. Their results did not suffer the upstream spurious waves as compared to those obtained by Forbes and Schwartz [27]. Later, Dias and Vanden-Broeck [16] proposed new solution in the critical flow regime and referred as the "generalized hydraulic fall". This solution was characterized by downstream supercritical flow with a train of waves on the upstream side. The presence of these waves in their numerical solution was the result of removing the upstream radiation condition.

When the fluid is subjected to the interaction of gravity and surface tension, the flow pattern can be sophisticated and the problem is generally difficult to solve. Forbes [22] was among the first to proposed numerical solutions of nonlinear flows over a semi-circular obstruction under the effect of gravity and surface tension. Three different branches of solution were presented in comparison with the results of linear problem. Sketches of typical free-surface profiles over a single obstacle are shown in Figure 1.1.

In case of flows over two obstacles, Pratt [54] investigated this problem

experimentally and theoretically using weakly nonlinear analysis. Though his experiments showed that there were only three stationary critical flow solutions (see Figure 1.2 (d)-(f)), he suggested that there could be up to nine possible steady flow configurations. Later, Belward [3] computed numerical solutions of a critical flow for which the hydraulic fall occurred at the leftmost obstacle with downstream supercritical flow. It should be noted that, for this solution, the flow pattern in the neighborhood of the rightmost obstacle was similar to that of the perturbation from uniform stream as in the case of flow over an obstacle. This flow configuration had been found in the experiments of Pratt [54] as shown in Figure 1.2(f). Recently, Binder, Vanden-Broeck and Dias [9] showed also that there exist two types of solution in subcritical flow regime, and one type in supercritical flow regime as illustrated in Figure 1.2 (a)-(c).

In this thesis, we consider the steady free-surface flows over submerged obstacles at the bottom of a channel. The fluid is assumed to be inviscid and incompressible; and the flow is irrotational. Flow domain is bounded below by a horizontal rigid bottom, except at the presence of obstacles, and above by a free surface. The conditions of incompressibility and irrotationlity of the fluid motion imply the existence of potential function and stream function. The fluid domain in the physical plane is transformed onto the complex plane. Gravity and surface tension are included in the dynamic boundary condition. The fully non-linear problem is solved numerically by the boundary integral equation technique. This integral equation provides a relationship between the flow variables on the free surface. One of the advantages of this technique is that mesh points in the numerical scheme need only be placed on the free surface and the bottom rather than throughout the entire flow domain. We obtain the numerical solutions by solving a system of nonlinear algebraic equations on the free surface using New-

ton's method. Details of the formulation and the numerical procedure of the fully nonlinear problem are given in chapter II. The weakly nonlinear problem associated with the stationary and time-dependent forced Korteweg-de Vries equations are presented in chapter III. In chapter IV, we recapture the big picture of free-surface flows over a single obstacle problem. For a simple understanding in this thesis, we shall denote a positive obstacle as "bump"and a negative obstacle as "dip". Solutions of the fully nonlinear and the weakly nonlinear problems are calculated and compared for each case to constitute a check on these numerical results. Solution diagrams are consequently presented to shows the existence of different flow regimes. Finally, free-surface flows over two submerged obstacles are discussed in chapter V.

(a) Subcritical flow   (b) Supercritical flow

(c) Hydraulic fall   (d) Generalized hydraulic fall
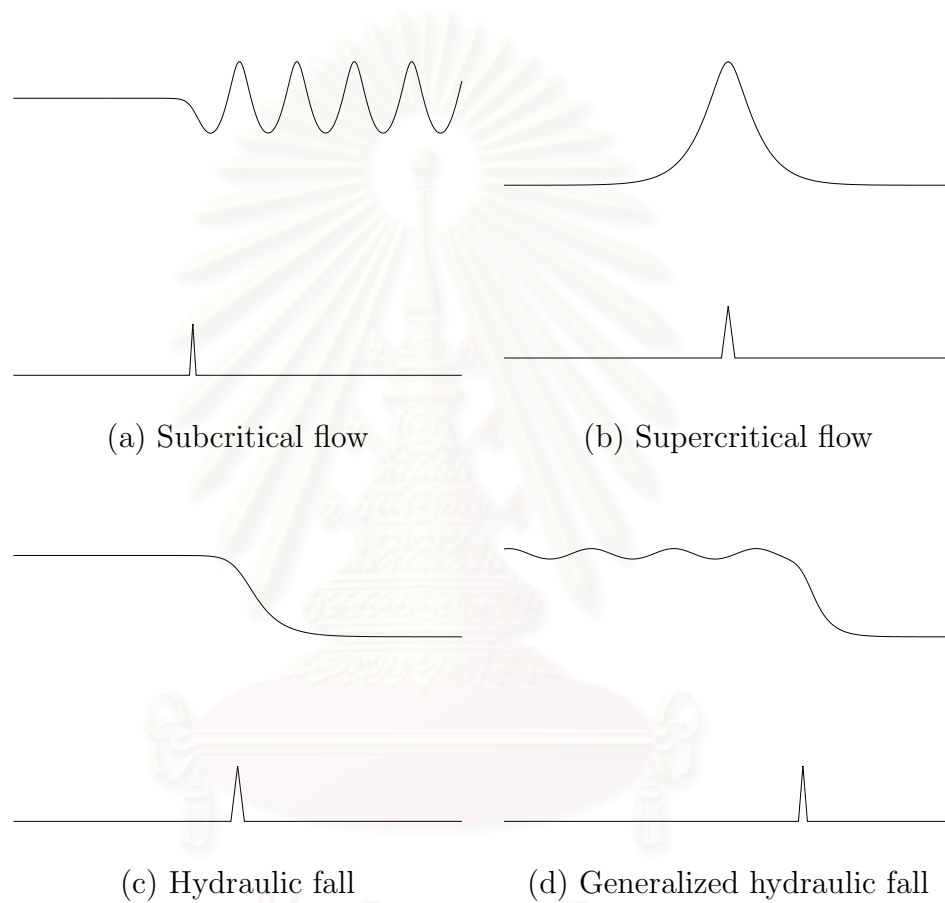
Figure 1.1: Sketches of four basic free-surface flows over a single obstacle: (a) Subcritical and uniform flow on upstream with waves on downstream. (b) Supercritical flow. (c) Critical flow with upstream subcritical and downstream supercritical known as the "hydraulic fall". (d) "Generalized hydraulic fall" solution in critical flow regime.
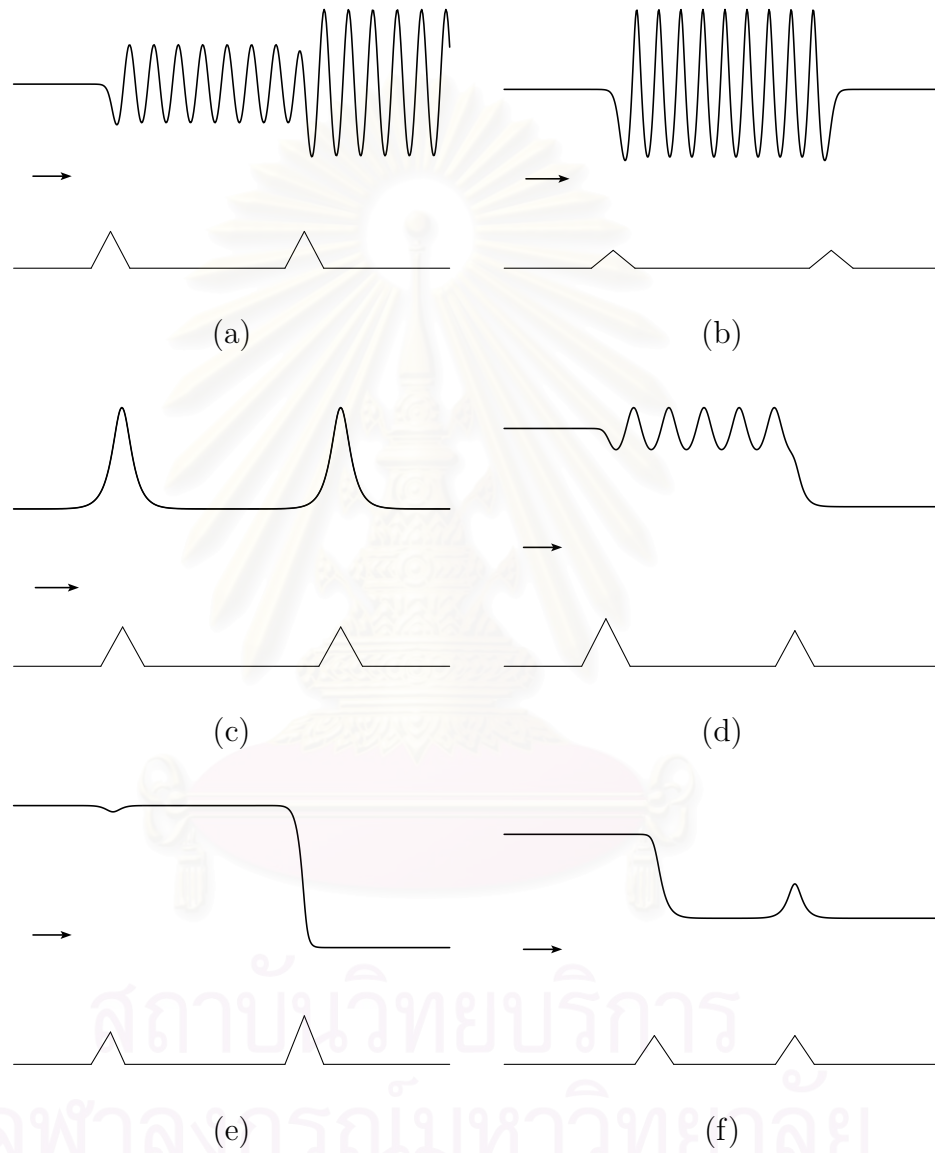
Figure 1.2: Sketches of the basic free-surface flows over two triangular obstacles for which (a) and (b) are in subcritical regimes, (c) is in supercritical regime, and (d)-(f) are in critical regimes.

CHAPTER II

FULLY NONLINEAR PROBLEM

In this chapter, mathematical formulation and numerical procedure for the fully nonlinear problem of free-surface flows over two submerged obstacles are presented. The problem is formulated as an integral equation by using a relationship between the flow variables on the free surface based on the boundary integral equation technique (Forbes and Schwartz [27], Forbes [22], Zhang and Zhu [66], Belward [3], Dias and Vanden-Broeck [16], Tooley and Vanden-Broeck [58], Binder, Vanden-Broeck and Dias [9], Binder and Vanden-Broeck [8], and others). This integral equation is then discretized as a system of nonlinear algebraic equations and solved numerically by using Newton's method. Details of the mathematical formulation and the numerical procedure are given in §2.1 and §2.2, respectively.

2.1 Mathematical Formulation

Steady two-dimensional free-surface flows over two submerged obstacles at the channel bottom are considered. The fluid is assumed to be inviscid and incompressible; and the flow is irrotational. Flow domain is bounded below by a horizontal bottom CD, except at the presence of obstacles, and above by a free surface AB. Sketch of the physical domain is shown in Figure 2.1. Flow direction is chosen to be from left to right.

We introduce Cartesian coordinates (x, y) with the x-axis along the horizontal bottom and the y-axis directed vertically upwards through the apex of the
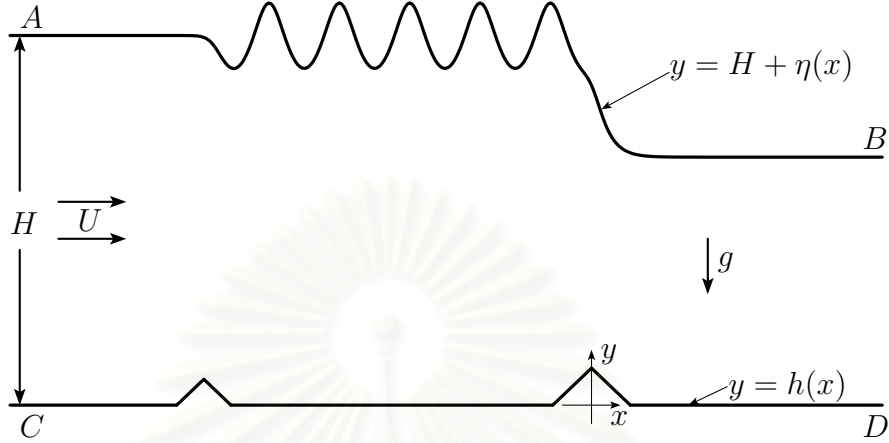
Figure 2.1: Sketch of free-surface flow over two obstacles in physical plane.

rightmost obstacle. Gravity g is acting in the negative y-direction. Far upstream as $x \to -\infty$, the flow approaches a uniform stream with constant velocity U and constant depth H.

We denote the free surface by $y = H + \eta(x)$ where $\eta(x)$ is the elevation of free surface from the undisturbed flow level $y = H$. The bottom is described by $y = h(x)$. On the horizontal segments of the bottom, $h \equiv 0$. At the obstacles, it is assumed that $h(x)$ is either a positive or negative continuous function. Under this requirement, the solutions are found to be qualitatively similar for different obstacle shapes. For simplicity, we consider the isosceles triangular shaped obstacles whose base length equals to twice its height. Let I_i, J_i and K_i denote the upstream corner, the apex, and the downstream corner positions of the obstacle i, respectively (see Figure 2.2). Here $i = 1, 2$ refer to the leftmost and the rightmost obstacles, respectively. The obstacle height hob_i is defined as vertical distance of the apex away from the horizontal bottom. The distance between two obstacles
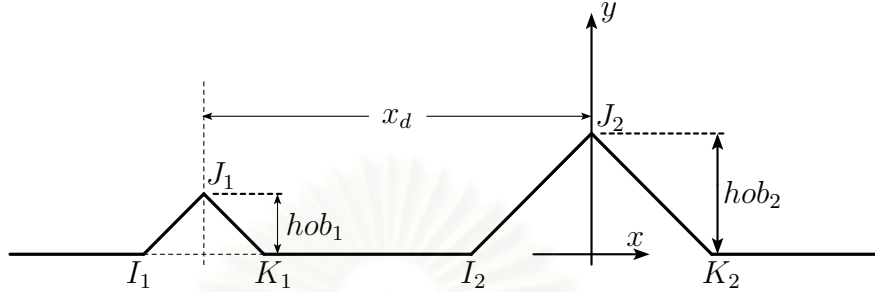
Figure 2.2: Geometry of the obstacles.

is defined by

$$x_d = x_{J_2} - x_{J_1}. \tag{2.1}$$

The velocity components in the x- and y- directions are denoted by u and v, respectively.

2.1.1 Dynamic and Kinematic Boundary Conditions

For inviscid fluid, the flow is governed by the *Euler equations*

$$\rho \frac{D\mathbf{q}}{Dt} = -\nabla p + \rho \mathbf{F}.$$

Here ρ is the fluid density, $\mathbf{q}(\mathbf{x}, t) = u\mathbf{i} + v\mathbf{j}$ is the velocity vector of fluid motion, $\frac{D}{Dt} = \frac{\partial}{\partial t} + \mathbf{q} \cdot \nabla$ is the total (or material) derivative, p is the fluid pressure, and $\mathbf{F}$ is the external or body force. In this study, the effects of gravity and surface tension are both taken into accounts. For steady irrotational flow of an incompressible fluid, the *Euler equations* can be reduced to

$$\frac{1}{2}(u^2 + v^2) + \frac{p}{\rho} + gy - \frac{T}{\rho}\kappa = B^* \tag{2.2}$$

along a streamline. Equation (2.2) is known as the **Bernoulli equation** or **dynamic boundary condition** on the free boundary. On the free surface, p is given

as constant atmospheric pressure. Here T is the coefficient of surface tension, κ is the curvature of the free surface, and B^* is the Bernoulli constant. The curvature is defined by $\kappa = \dfrac{\eta''(x)}{\left(1+\left(\eta'(x)\right)^2\right)^{3/2}}$. Equation (2.2) can be rewritten as

$$\frac{1}{2}(u^2 + v^2) + gy - \frac{T}{\rho}\kappa = B^{**}, \tag{2.3}$$

where $B^{**} = B^* - \dfrac{p}{\rho}$.

On the rigid bottom $y = h(x)$, the normal velocity must vanish. This implies that the **kinematic boundary condition** on this boundary is

$$uh_x = v \qquad \text{on} \ \ y = h(x). \tag{2.4}$$

2.1.2 Dimensionless Variables

It is convenient to normalize the physical problem by introducing appropriate scaling variables. This can be done by choosing far upstream velocity U as the unit velocity and far upstream depth H as the unit length. The dimensionless variables are

$$u^* = \frac{u}{U}, \qquad\qquad v^* = \frac{v}{U},$$
$$x^* = \frac{x}{H}, \qquad\qquad y^* = \frac{y}{H},$$
$$\eta^* = \frac{\eta}{H}, \qquad\qquad h^* = \frac{h}{H}.$$

After dropping the asterisks, the nondimensional forms of equations (2.3) and (2.4) can readily be obtained as

$$u^2 + v^2 + \frac{2}{F^2}y - \frac{2}{F^2}\kappa Bo = \bar{B} \qquad \text{on} \ \ y = 1 + \eta, \tag{2.5}$$

$$uh_x = v \qquad \text{on} \ \ y = h(x). \tag{2.6}$$

Here $F = \frac{U}{\sqrt{gH}}$ is the upstream Froude number, $Bo = \frac{T}{\rho g H^2}$ is the Bond number and $\bar{B} = \frac{B^{**}}{U^2}$ is the dimensionless Bernoulli constant. In reference to the linear

wave theory, the flow regimes can be defined as follows. If $F < 1$, the flow is subcritical. If $F > 1$, the flow is supercritical. If $F < 1$ on one side and $F > 1$ on the other side, the flow is critical. We determine the constant term on the right hand side of (2.5) by using the uniform flow condition at far upstream. This gives

$$u^2 + v^2 + \frac{2}{F^2}(y - 1) - \frac{2}{F^2}\kappa Bo - 1 = 0 \quad \text{on} \quad y = 1 + \eta. \tag{2.7}$$

2.1.3 Potential Function and Stream Function

The problem can be greatly simplified by the use of complex function theory. From the assumption of incompressibility, conservation of fluid mass implies

$$\frac{\partial u}{\partial x} + \frac{\partial v}{\partial y} = 0. \tag{2.8}$$

A differentiable function $\psi(x, y)$ can be chosen as

$$u = \frac{\partial \psi}{\partial y} \quad \text{and} \quad v = -\frac{\partial \psi}{\partial x} \tag{2.9}$$

so that (2.8) is automatically satisfied. The function ψ is known as the **stream function**. For irrotational flow, we have the following relationship

$$\nabla \times \mathbf{q} = \frac{\partial v}{\partial x} - \frac{\partial u}{\partial y} = 0.$$

This equation can be satisfied by letting

$$\mathbf{q} = u(x, y)\mathbf{i} + v(x, y)\mathbf{j} = \frac{\partial \phi}{\partial x}\mathbf{i} + \frac{\partial \phi}{\partial y}\mathbf{j} = \nabla \phi, \tag{2.10}$$

where the differentiable function $\phi = \phi(x, y)$ is known as the **potential function**. From (2.9) and (2.10), we can deduce that

$$\frac{\partial \phi}{\partial x} = \frac{\partial \psi}{\partial y} \quad \text{and} \quad \frac{\partial \phi}{\partial y} = -\frac{\partial \psi}{\partial x}. \tag{2.11}$$

Relations (2.11) are the well known **Cauchy-Riemann equations** in the theory of functions of complex variables.
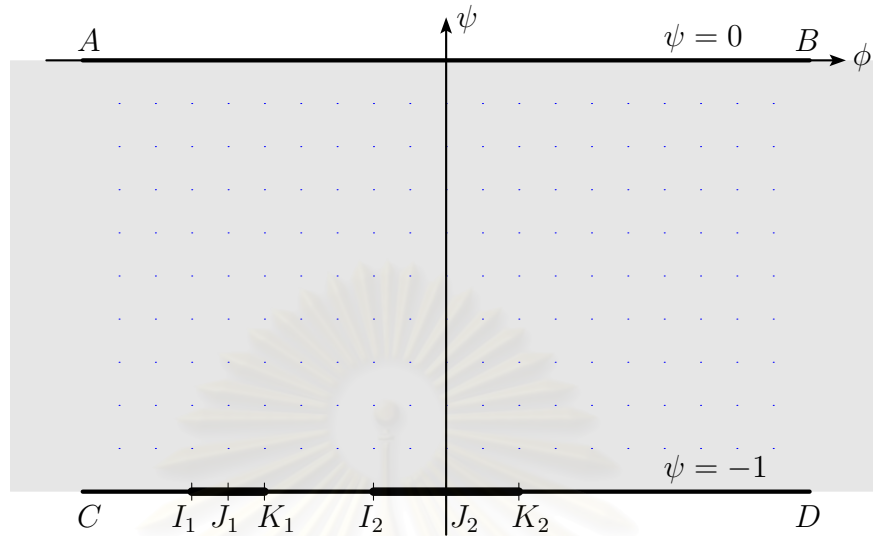
Figure 2.3: Sketch of flow domain in the f-plane.

Next, we introduce the complex potential function f by

$$f(x, y) = \phi(x, y) + i\psi(x, y),$$

and the complex velocity w by

$$w(x, y) \equiv u - iv = \frac{df}{dz}.$$

Here $z = x + iy$.

Without loss of generality, we choose the streamline $\psi = 0$ on the free surface and $\phi = 0$ at the point $x = 0$ on the bottom (J_2). By the definition of v in (2.9), the bottom is another streamline with $\psi = -1$. The values of ϕ at the apex of obstacles J_i are denoted by ϕ_{J_i} and those at the upstream I_i and downstream K_i corners of the obstacles by ϕ_{I_i} and ϕ_{K_i} for $i = 1, 2$. The flow configuration in the f-plane is an infinite strip as shown in Figure 2.3. This concludes the mathematical formulation of the problem. We seek w as an analytic function of f in the strip $-1 < \psi < 0$. This function must approach 1 as $\phi \to -\infty$, and satisfy (2.6) and (2.7).
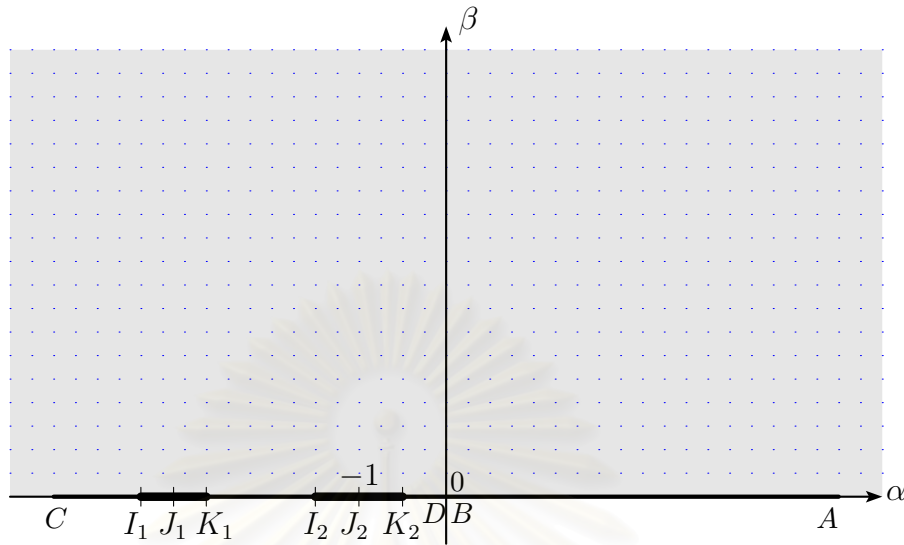
Figure 2.4: Sketch of flow in the upper half ζ-plane.

2.1.4 Conformal Mapping

To obtain the required integral equation, we map conformally the flow domain from the complex f-plane onto **upper half** of the complex ζ-plane by

$$\zeta = \alpha + i\beta = e^{-\pi f}.$$

The free surface and the bottom are mapped onto positive and negative real axes of the ζ-plane, respectively (see Figure 2.4). All the reference points in the complex f- and ζ-planes are listed in Table 2.1.

Let us introduce a new complex function $\hat{\tau} - i\hat{\theta} = \ln\left(\frac{df}{dz}\right)$, the so-called **hodograph variables** or **logarithmic velocity**. It is related to the complex velocity by

$$w = u - iv = e^{\hat{\tau} - i\hat{\theta}}. \tag{2.12}$$

Here $\hat{\theta}(\alpha, \beta)$ represents the direction of the velocity $(-\pi \leq \hat{\theta} \leq \pi)$ and $e^{\hat{\tau}}$ is the flow speed $(e^{\hat{\tau}} = \sqrt{u^2 + v^2})$. In ζ-plane, the kinematic boundary condition (2.6)

(x, y) plane	f-plane	ζ-plane
A	$\psi = 0, \phi = \phi_A = -\infty$	$\alpha = \alpha_A = \infty, \beta = 0$
B	$\psi = 0, \phi = \phi_B = \infty$	$\alpha = \alpha_B = 0, \beta = 0$
C	$\psi = -1, \phi = \phi_C = -\infty$	$\alpha = \alpha_C = -\infty, \beta = 0$
D	$\psi = -1, \phi = \phi_D = \infty$	$\alpha = \alpha_D = 0, \beta = 0$
I_1	$\psi = -1, \phi = \phi_{I_1}$	$\alpha = \alpha_{I_1}, \beta = 0$
J_1	$\psi = -1, \phi = \phi_{J_1}$	$\alpha = \alpha_{J_1}, \beta = 0$
K_1	$\psi = -1, \phi = \phi_{K_1}$	$\alpha = \alpha_{K_1}, \beta = 0$
I_2	$\psi = -1, \phi = \phi_{I_2}$	$\alpha = \alpha_{I_2}, \beta = 0$
J_2	$\psi = -1, \phi = \phi_{J_2} = 0$	$\alpha = \alpha_{J_2} = -1, \beta = 0$
K_2	$\psi = -1, \phi = \phi_{K_2}$	$\alpha = \alpha_{K_2}, \beta = 0$

Table 2.1: Values of reference points in the f-plane and the ζ-plane.

on the bottom $(-\infty < \alpha < 0)$ can be expressed as

$$
\hat{\theta}(\alpha, -1) = \begin{cases} \theta_1^{up} & , \alpha_{I_1} < \alpha < \alpha_{J_1}, \\[2mm] \theta_1^{do} & , \alpha_{J_1} < \alpha < \alpha_{K_1}, \\[2mm] \theta_2^{up} & , \alpha_{I_2} < \alpha < \alpha_{J_2}, \\[2mm] \theta_2^{do} & , \alpha_{J_2} < \alpha < \alpha_{K_2}, \\[2mm] 0 & , \text{otherwise} \end{cases} \tag{2.13}
$$

where θ_i^{up} and θ_i^{do} are the inclined acute angles of upstream and downstream side of the obstacle i^{th} with $\theta_i^{do} = -\theta_i^{up}$ for $i = 1, 2$.
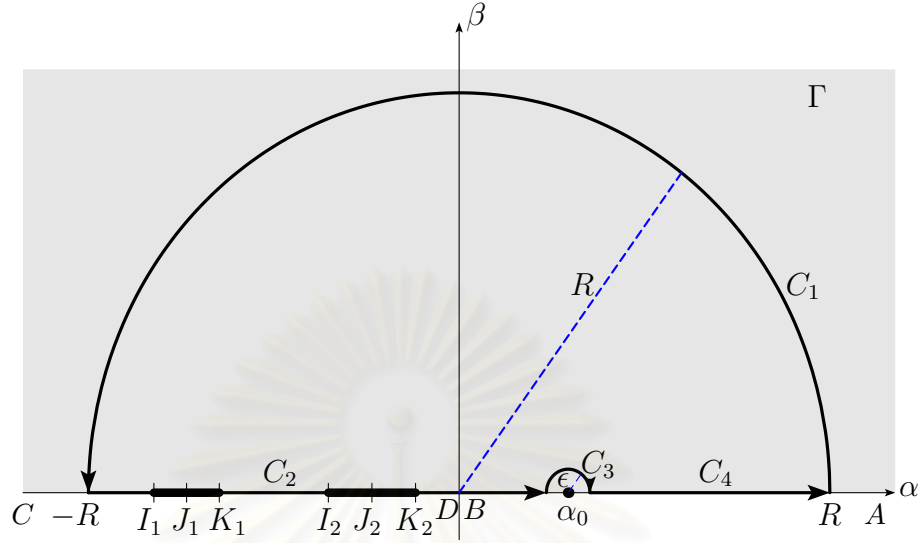
Figure 2.5: Contour Γ in the complex ζ-plane.

2.1.5 Boundary Integral Equation

In this section, an integral equation relating $\hat{\tau}$ and $\hat{\theta}$ on the free surface and the bottom in ζ-plane is derived. Firstly, we consider a contour integral of the form

$$\oint_\Gamma \frac{\hat{\tau}(\alpha,\beta) - i\hat{\theta}(\alpha,\beta)}{\zeta - \zeta_0} d\zeta$$

where ζ_0 is a point on the free surface or the bottom ($\zeta_0 = \alpha_0$). The path Γ consists of (see Figure 2.5)

$C_1 :=$ semi-circular arc of radius R centered at the origin,

$C_2 :=$ contour line from $-R$ to $\alpha_0 - \epsilon$,

$C_3 :=$ semi-circular arc of radius ϵ centered at α_0, and

$C_4 :=$ contour line from $\alpha_0 + \epsilon$ to R.

That is

$$
\oint_\Gamma \frac{\hat{\tau}(\alpha,\beta) - i\hat{\theta}(\alpha,\beta)}{\zeta - \alpha_0} d\zeta = \int_{C_1} \frac{\hat{\tau}(\alpha,\beta) - i\hat{\theta}(\alpha,\beta)}{\zeta - \alpha_0} d\zeta + \int_{-R}^{\alpha_0 - \epsilon} \frac{\hat{\tau}(\alpha,0) - i\hat{\theta}(\alpha,0)}{\alpha - \alpha_0} d\alpha
$$
$$
+ \int_{C_3} \frac{\hat{\tau}(\alpha,\beta) - i\hat{\theta}(\alpha,\beta)}{\zeta - \alpha_0} d\zeta
$$
$$
+ \int_{\alpha_0 + \epsilon}^{R} \frac{\hat{\tau}(\alpha,0) - i\hat{\theta}(\alpha,0)}{\alpha - \alpha_0} d\alpha. \tag{2.14}
$$

From Cauchy theorem, integral over the closed contour Γ in (2.14) is zero. That is

$$\int_{C_1} \frac{\hat{\tau}(\alpha,\beta) - i\hat{\theta}(\alpha,\beta)}{\zeta - \alpha_0} d\zeta + \int_{-R}^{\alpha_0-\epsilon} \frac{\hat{\tau}(\alpha,0) - i\hat{\theta}(\alpha,0)}{\alpha - \alpha_0} d\alpha + \int_{C_3} \frac{\hat{\tau}(\alpha,\beta) - i\hat{\theta}(\alpha,\beta)}{\zeta - \alpha_0} d\zeta$$

$$+ \int_{\alpha_0+\epsilon}^{R} \frac{\hat{\tau}(\alpha,0) - i\hat{\theta}(\alpha,0)}{\alpha - \alpha_0} d\alpha = 0. \tag{2.15}$$

On the contour C_3, we have $\zeta = \alpha_0 + \epsilon e^{i\lambda}$ such that

$$\lambda = 0 \quad \text{at} \quad \zeta = \alpha_0 + \epsilon,$$

$$\lambda = \pi \quad \text{at} \quad \zeta = \alpha_0 - \epsilon.$$

Then the integral on the contour C_3 can be written as

$$\int_{C_3} \frac{\hat{\tau}(\alpha,\beta) - i\hat{\theta}(\alpha,\beta)}{\zeta - \alpha_0} d\zeta$$

$$= \int_{\pi}^{0} \frac{\hat{\tau}(\alpha_0 + \epsilon\cos\lambda, \epsilon\sin\lambda) - i\hat{\theta}(\alpha_0 + \epsilon\cos\lambda, \epsilon\sin\lambda)}{\epsilon e^{i\lambda}} i\epsilon e^{i\lambda} d\lambda$$

$$= -i \int_0^{\pi} \left[\hat{\tau}(\alpha_0 + \epsilon\cos\lambda, \epsilon\sin\lambda) - i\hat{\theta}(\alpha_0 + \epsilon\cos\lambda, \epsilon\sin\lambda) \right] d\lambda. \tag{2.16}$$

Using (2.16), (2.15) becomes

$$\int_{C_1} \frac{\hat{\tau}(\alpha,\beta) - i\hat{\theta}(\alpha,\beta)}{\zeta - \alpha_0} d\zeta + \int_{-R}^{\alpha_0-\epsilon} \frac{\hat{\tau}(\alpha,0) - i\hat{\theta}(\alpha,0)}{\alpha - \alpha_0} d\alpha$$

$$- i \int_0^{\pi} \left[\hat{\tau}(\alpha_0 + \epsilon\cos\lambda, \epsilon\sin\lambda) - i\hat{\theta}(\alpha_0 + \epsilon\cos\lambda, \epsilon\sin\lambda) \right] d\lambda$$

$$+ \int_{\alpha_0+\epsilon}^{R} \frac{\hat{\tau}(\alpha,0) - i\hat{\theta}(\alpha,0)}{\alpha - \alpha_0} d\alpha = 0.$$

Taking limit as $\epsilon \to 0$, we have

$$\hat{\tau}(\alpha_0, 0) - i\hat{\theta}(\alpha_0, 0) = \frac{1}{i\pi} \int_{C_1} \frac{\hat{\tau}(\alpha,\beta) - i\hat{\theta}(\alpha,\beta)}{\zeta - \alpha_0} d\zeta$$

$$+ \frac{1}{i\pi} \int_{-R}^{R} \frac{\hat{\tau}(\alpha,0) - i\hat{\theta}(\alpha,0)}{\alpha - \alpha_0} d\alpha. \tag{2.17}$$

As $|\alpha| \to \infty$ or $R \to \infty$, we have $w \to 1$ or $e^{\hat{\tau}-i\hat{\theta}} \to 1$ implying $\hat{\tau} - i\hat{\theta} \to 0$ and hence the first integral on the right hand side of (2.17) vanishes. The integral

equation (2.17) can now be reduced to

$$\hat{\tau}(\alpha_0, 0) - i\hat{\theta}(\alpha_0, 0) = \frac{1}{i\pi} \int_{-\infty}^{\infty} \frac{\hat{\tau}(\alpha, 0) - i\hat{\theta}(\alpha, 0)}{\alpha - \alpha_0} d\alpha. \qquad (2.18)$$

This integral is of Cauchy principal value. By taking the real part of (2.18), we obtain

$$\bar{\tau}(\alpha_0) = -\frac{1}{\pi} \int_{-\infty}^{\infty} \frac{\bar{\theta}(\alpha)}{\alpha - \alpha_0} d\alpha \qquad (2.19)$$

where $\bar{\tau}(\alpha)$ and $\bar{\theta}(\alpha)$ denote the values of $\hat{\tau}$ and $\hat{\theta}$ on the free surface and the bottom.

After applying the kinematic boundary condition (2.13), the integral in (2.19) on an interval $(-\infty, 0)$ can be simplified as follows.

$$\int_{-\infty}^{0} \frac{\bar{\theta}(\alpha)}{\alpha - \alpha_0} d\alpha = \int_{-\infty}^{\alpha_{I_1}} \frac{\bar{\theta}(\alpha)}{\alpha - \alpha_0} d\alpha + \int_{\alpha_{I_1}}^{\alpha_{J_1}} \frac{\bar{\theta}(\alpha)}{\alpha - \alpha_0} d\alpha + \int_{\alpha_{J_1}}^{\alpha_{K_1}} \frac{\bar{\theta}(\alpha)}{\alpha - \alpha_0} d\alpha$$

$$+ \int_{\alpha_{K_1}}^{\alpha_{I_2}} \frac{\bar{\theta}(\alpha)}{\alpha - \alpha_0} d\alpha + \int_{\alpha_{I_2}}^{\alpha_{J_2}} \frac{\bar{\theta}(\alpha)}{\alpha - \alpha_0} d\alpha + \int_{\alpha_{J_2}}^{\alpha_{K_2}} \frac{\bar{\theta}(\alpha)}{\alpha - \alpha_0} d\alpha$$

$$+ \int_{\alpha_{K_2}}^{0} \frac{\bar{\theta}(\alpha, 0)}{\alpha - \alpha_0} d\alpha$$

$$= \theta_1^{up} \ln \left| \frac{\alpha_{J_1} - \alpha_0}{\alpha_{I_1} - \alpha_0} \right| + \theta_1^{do} \ln \left| \frac{\alpha_{K_1} - \alpha_0}{\alpha_{J_1} - \alpha_0} \right|$$

$$+ \theta_2^{up} \ln \left| \frac{\alpha_{J_2} - \alpha_0}{\alpha_{I_2} - \alpha_0} \right| + \theta_2^{do} \ln \left| \frac{\alpha_{K_2} - \alpha_0}{\alpha_{J_2} - \alpha_0} \right|$$

$$= \theta_1^{up} \ln \left| \frac{(\alpha_{J_1} - \alpha_0)^2}{(\alpha_{I_1} - \alpha_0)(\alpha_{K_1} - \alpha_0)} \right| + \theta_2^{up} \ln \left| \frac{(\alpha_{J_2} - \alpha_0)^2}{(\alpha_{I_2} - \alpha_0)(\alpha_{K_2} - \alpha_0)} \right|.$$

Finally, equation (2.19) can be rewritten as

$$\bar{\tau}(\alpha_0) = -\frac{\theta_1^{up}}{\pi} \ln \left| \frac{(\alpha_{J_1} - \alpha_0)^2}{(\alpha_{I_1} - \alpha_0)(\alpha_{K_1} - \alpha_0)} \right| - \frac{\theta_2^{up}}{\pi} \ln \left| \frac{(\alpha_{J_2} - \alpha_0)^2}{(\alpha_{I_2} - \alpha_0)(\alpha_{k_2} - \alpha_0)} \right|$$

$$- \frac{1}{\pi} \int_{0}^{\infty} \frac{\bar{\theta}(\alpha)}{\alpha - \alpha_0} d\alpha. \qquad (2.20)$$

This provides a relation between $\bar{\tau}$ and $\bar{\theta}$ on the free surface and the bottom.

To determine the free surface and the bottom profile, we consider the identity

$$\frac{d}{d\zeta}(x + iy) = w^{-1} = \frac{\left(e^{\bar{\tau} - i\bar{\theta}}\right)^{-1}}{-\pi e^{-\pi f}} = -\frac{e^{-\bar{\tau}}}{\pi \zeta}(\cos \bar{\theta} + i \sin \bar{\theta}).$$

Taking real and imaginary parts for $\beta = 0$, we have

$$\frac{\partial x}{\partial \alpha} = -\frac{e^{-\bar{\tau}(\alpha)}}{\pi \alpha} \cos \bar{\theta}(\alpha)$$

and

$$\frac{\partial y}{\partial \alpha} = -\frac{e^{-\bar{\tau}(\alpha)}}{\pi \alpha} \sin \bar{\theta}(\alpha).$$

On AB $(0 < \alpha_0 < \infty)$, free-surface profile can be obtained from

$$x(\alpha_0) = x_A + \frac{1}{\pi} \int_{\alpha_0}^{\infty} \frac{e^{-\bar{\tau}(\alpha)}}{\alpha} \cos \bar{\theta}(\alpha) d\alpha, \tag{2.21}$$

and

$$y(\alpha_0) = 1 + \frac{1}{\pi} \int_{\alpha_0}^{\infty} \frac{e^{-\bar{\tau}(\alpha)}}{\alpha} \sin \bar{\theta}(\alpha) d\alpha. \tag{2.22}$$

Here x_A is the x coordinate at point A.

On CD $(-\infty < \alpha_0 < 0)$, the bottom profile is determined from

$$x(\alpha_0) = -\frac{1}{\pi} \int_{\alpha_{J_2}}^{\alpha_0} \frac{e^{-\bar{\tau}(\alpha)}}{\alpha} \cos \bar{\theta}(\alpha) d\alpha, \tag{2.23}$$

and

$$y(\alpha_0) = \frac{1}{\pi} \int_{\alpha_0}^{0} \frac{e^{-\bar{\tau}(\alpha)}}{\alpha} \sin \bar{\theta}(\alpha) d\alpha. \tag{2.24}$$

Next we are required to calculate the curvature κ of the free surface. It is convenient to express κ in terms of the hodograph variables as follows. We rewrite the first and the second derivatives of η as

$$\eta'(x) = \eta_\alpha \alpha_x = \tan \bar{\theta}$$

and

$$\begin{aligned}
\eta''(x) &= (\tan \bar{\theta})_\alpha \alpha_x \\
&= \left(\sec^2 \bar{\theta} \frac{\partial \bar{\theta}}{\partial \alpha} \right) \left(-\frac{\pi \alpha}{e^{-\bar{\tau}} \cos \bar{\theta}} \right) \\
&= \sec^3 \bar{\theta} \left(-\pi \alpha e^{\bar{\tau}} \frac{\partial \bar{\theta}}{\partial \alpha} \right).
\end{aligned}$$

Accordingly, the curvature κ is

$$
\begin{aligned}
\kappa &= \frac{\eta''(x)}{\left(1 + \left(\eta'(x)\right)^2\right)^{3/2}} \\
&= \frac{\sec^3 \bar{\theta}\left(-\pi\alpha e^{\bar{\tau}} \frac{\partial \bar{\theta}}{\partial \alpha}\right)}{(1 + \tan^2 \bar{\theta})^{3/2}} \\
&= -\pi\alpha e^{\bar{\tau}} \frac{\partial \bar{\theta}}{\partial \alpha}.
\end{aligned} \tag{2.25}
$$

From (2.25) and $\sqrt{u^2 + v^2} = e^{\bar{\tau}}$, equation (2.7) becomes

$$
e^{2\bar{\tau}} + \frac{2}{F^2}(y - 1) + \frac{2}{F^2}\pi\alpha e^{\bar{\tau}} \frac{\partial \bar{\theta}}{\partial \alpha} Bo - 1 = 0. \tag{2.26}
$$

Equations (2.20), (2.21)-(2.24) and (2.26) define a system of nonlinear integral equations for unknowns $\bar{\theta}$ on the free surface.

2.2 Numerical Procedure

In this section, we describe numerical approach for the nonlinear problem derived in previous section. This numerical procedure has been successfully used by Zhang and Zhu [66], Vanden-Broeck [61], and others for solving nonlinear integral equations.

Firstly, we write the hodograph variables in terms of the independent variable ϕ by the change of variables

$$
\alpha = \chi_\phi e^{-\pi\phi},
$$

where

$$
\chi_\phi = \begin{cases} 1 & \text{, if } \phi \text{ is on the free surface,} \\ -1 & \text{, if } \phi \text{ is on the bottom.} \end{cases}
$$

Values of α for the corresponding values of ϕ at the apex and the corners of obstacles are given in Table 2.2. For simplicity, we use the notation $\tau(\phi) = \bar{\tau}(\chi_\phi e^{-\pi\phi}), \theta(\phi) = \bar{\theta}(\chi_\phi e^{-\pi\phi}), x(\phi) = x(\chi_\phi e^{-\pi\phi})$ and $y(\phi) = y(\chi_\phi e^{-\pi\phi})$.

I_1	$\alpha_{I_1} = -e^{-\pi\phi_{I_1}}$
J_1	$\alpha_{J_1} = -e^{-\pi\phi_{J_1}}$
K_1	$\alpha_{K_1} = -e^{-\pi\phi_{K_1}}$
I_2	$\alpha_{I_2} = -e^{-\pi\phi_{I_2}}$
J_2	$\alpha_{J_2} = -e^{-\pi\phi_{J_2}}$
K_2	$\alpha_{K_2} = -e^{-\pi\phi_{K_2}}$

Table 2.2: Values of α at the apexs and corners of obstacles.

Equation (2.20) becomes

$$\tau(\phi_0) = \bar{\tau}(\alpha_0) = -\frac{\theta_1^{up}}{\pi} \ln \left| \frac{\left(e^{-\pi\phi_{J_1}} + \chi_{\phi_0} e^{-\pi\phi_0}\right)^2}{\left(e^{-\pi\phi_{I_1}} + \chi_{\phi_0} e^{-\pi\phi_0}\right)\left(e^{-\pi\phi_{K_1}} + \chi_{\phi_0} e^{-\pi\phi_0}\right)} \right|$$
$$- \frac{\theta_2^{up}}{\pi} \ln \left| \frac{\left(e^{-\pi\phi_{J_2}} + \chi_{\phi_0} e^{-\pi\phi_0}\right)^2}{\left(e^{-\pi\phi_{I_2}} + \chi_{\phi_0} e^{-\pi\phi_0}\right)\left(e^{-\pi\phi_{K_2}} + \chi_{\phi_0} e^{-\pi\phi_0}\right)} \right|$$
$$- \int_{-\infty}^{\infty} \frac{\theta(\phi)e^{-\pi\phi}}{e^{-\pi\phi} - \chi_{\phi_0} e^{-\pi\phi_0}} d\phi. \tag{2.27}$$

The third term on the right hand side of equation (2.26) can be rewritten as

$$\frac{2}{F^2}\pi\alpha e^{\bar{\tau}} \frac{\partial \bar{\theta}}{\partial \alpha} Bo = \frac{2}{F^2}\pi e^{-\pi\phi} e^{\tau} \frac{\partial \theta}{\partial \phi} \frac{\partial \phi}{\partial \alpha} Bo$$
$$= -\frac{2}{F^2} e^{\tau} \frac{\partial \theta}{\partial \phi} Bo,$$

and (2.26) becomes

$$e^{2\tau(\phi)} + \frac{2}{F^2}(y(\phi) - 1) - \frac{2}{F^2} e^{\tau(\phi)} \frac{\partial \theta(\phi)}{\partial \phi} Bo - 1 = 0. \tag{2.28}$$

Finally, the free-surface profile can be calculated from

$$x(\phi_0) = x_A + \int_{-\infty}^{\phi_0} e^{-\tau(\phi)} \cos \theta(\phi) d\phi, \tag{2.29}$$

$$y(\phi_0) = 1 + \int_{-\infty}^{\phi_0} e^{-\tau(\phi)} \sin \theta(\phi) d\phi, \tag{2.30}$$

and the bottom profile is determined from

$$x(\phi_0) = \int_0^{\phi_0} e^{-\tau(\phi)} \cos\theta(\phi)d\phi, \tag{2.31}$$

$$y(\phi_0) = -\int_{\phi_0}^{\infty} e^{-\tau(\phi)} \sin\theta(\phi)d\phi. \tag{2.32}$$

To solve the problem numerically, the free surface must be truncated at ϕ_1 and ϕ_{N+1} for the corresponding far upstream $x \to -\infty$, and far downstream $x \to \infty$, respectively. The truncated free surface is then discretized into N equally segments with

$$\phi_I = \left(-\frac{N}{2} + I - 1\right)\Delta, \quad I = 1, 2, \ldots, N+1.$$

Here $\Delta > 0$ is the mesh spacing, N is an even integer, and the unknown variables on the free surface are

$$\theta_I = \theta(\phi_I), \quad I = 1, 2, \ldots, N+1.$$

Next, we evaluate the values τm_I of $\tau(\phi)$ at the midpoints

$$\phi m_I = \frac{\phi_I + \phi_{I+1}}{2}, \quad I = 1, 2, \ldots, N \tag{2.33}$$

by applying trapezoidal rule to the integral in (2.27) with summation over the points ϕ_I. Symmetry of the quadrature and of the distribution of mesh points enable us to evaluate the integral which is of Cauchy principal value as if it were an ordinary integral (see Appendix). Then we replace (2.27) by

$$
\begin{aligned}
\tau(\phi_0) = & -\frac{\theta_1^{up}}{\pi}\ln\left|\frac{\left(e^{-\pi\phi_{J_1}} + \chi_{\phi_0}e^{-\pi\phi_0}\right)^2}{\left(e^{-\pi\phi_{I_1}} + \chi_{\phi_0}e^{-\pi\phi_0}\right)\left(e^{-\pi\phi_{K_1}} + \chi_{\phi_0}e^{-\pi\phi_0}\right)}\right| \\
& -\frac{\theta_2^{up}}{\pi}\ln\left|\frac{\left(e^{-\pi\phi_{J_2}} + \chi_{\phi_0}e^{-\pi\phi_0}\right)^2}{\left(e^{-\pi\phi_{I_2}} + \chi_{\phi_0}e^{-\pi\phi_0}\right)\left(e^{-\pi\phi_{K_2}} + \chi_{\phi_0}e^{-\pi\phi_0}\right)}\right| \\
& -\int_{\phi_1}^{\phi_{N+1}}\frac{\theta(\phi)e^{-\pi\phi}}{e^{-\pi\phi} - \chi_{\phi_0}e^{-\pi\phi_0}}d\phi.
\end{aligned}
$$

Following Hocking and Vanden-Broeck [39], the above integral can be re-written as

$$\int_{\phi_1}^{\phi_{N+1}} \frac{\theta(\phi)e^{-\pi\phi}}{e^{-\pi\phi} - \chi_{\phi_0}e^{-\pi\phi_0}}d\phi = \int_{\phi_1}^{\phi_{N+1}} \frac{\left(\theta(\phi) - \theta(\phi_0)\right)e^{-\pi\phi}}{e^{-\pi\phi} - \chi_{\phi_0}e^{-\pi\phi_0}}d\phi$$
$$+ \int_{\phi_1}^{\phi_{N+1}} \frac{\theta(\phi_0)}{e^{-\pi\phi} - \chi_{\phi_0}e^{-\pi\phi_0}}e^{-\pi\phi}d\phi$$
$$= \int_{\phi_1}^{\phi_{N+1}} \frac{\left(\theta(\phi) - \theta(\phi_0)\right)e^{-\pi\phi}}{e^{-\pi\phi} - \chi_{\phi_0}e^{-\pi\phi_0}}d\phi$$
$$- \frac{\theta(\phi_0)}{\pi} \ln\left|\frac{e^{-\pi\phi_{N+1}} - \chi_{\phi_0}e^{-\pi\phi_0}}{e^{-\pi\phi_1} - \chi_{\phi_0}e^{-\pi\phi_0}}\right|$$

before applying the trapezoidal rule. The value of τm_I can be calculated from

$$\tau m_I = \tau(\phi m_I) = -\frac{\theta_1^{up}}{\pi}\ln\left|\frac{\left(e^{-\pi\phi_{J_1}} + e^{-\pi\phi m_I}\right)^2}{\left(e^{-\pi\phi_{I_1}} + e^{-\pi\phi m_I}\right)\left(e^{-\pi\phi_{K_1}} + e^{-\pi\phi m_I}\right)}\right|$$
$$- \frac{\theta_2^{up}}{\pi}\ln\left|\frac{\left(e^{-\pi\phi_{J_2}} + e^{-\pi\phi m_I}\right)^2}{\left(e^{-\pi\phi_{I_2}} + e^{-\pi\phi m_I}\right)\left(e^{-\pi\phi_{K_2}} + e^{-\pi\phi m_I}\right)}\right|$$
$$- \sum_{j=1}^{N+1} \frac{\left(\theta_j - \theta(\phi m_I)\right)e^{-\pi\phi_j}}{e^{-\pi\phi_j} - e^{-\pi\phi m_I}}\omega_j\Delta$$
$$+ \frac{\theta(\phi m_I)}{\pi}\ln\left|\frac{e^{-\pi\phi_{N+1}} - e^{-\pi\phi m_I}}{e^{-\pi\phi_1} - e^{-\pi\phi m_I}}\right|.$$

Here

$$w_j = \begin{cases} \frac{1}{2}, & \text{if } j = 0 \text{ and } N+1, \\ 1, & \text{otherwise}, \end{cases}$$

and $\theta(\phi m_I)$ is the value of θ at the midpoint I and evaluated by the four-point interpolation, denoted by θm_I. That is

$$\theta m_1 = \frac{5}{16}\theta_1 + \frac{15}{16}\theta_2 - \frac{5}{16}\theta_3 + \frac{1}{16}\theta_4,$$
$$\theta m_I = -\frac{1}{16}\theta_{I-1} + \frac{9}{16}\theta_I + \frac{9}{16}\theta_{I+1} - \frac{1}{16}\theta_{I+2}, \quad I = 2, 3, ..., N-1$$

and

$$\theta m_N = \frac{5}{16}\theta_{N+1} + \frac{15}{16}\theta_N - \frac{5}{16}\theta_{N-1} + \frac{1}{16}\theta_{N-2}.$$

Next we evaluate $x_I = x(\phi_I)$ and $y_I = y(\phi_I)$ by applying the trapezoidal rule to equations (2.29) and (2.30), respectively. This gives

$$x_1 = x_A,$$

$$y_1 = 1,$$

$$x_I = x_{I-1} + e^{-\tau m_{I-1}} \cos(\theta m_{I-1})\, \Delta,$$

$$y_I = y_{I-1} + e^{-\tau m_{I-1}} \sin(\theta m_{I-1})\, \Delta, \quad I = 2, 3, \ldots, N+1.$$

For x_A, we assume that x_A is equal to the x value at $\phi = \phi_1$ on the bottom since the flow is essentially uniform far upstream. This technique was also used by Goh and Tuck [29], and Zhang and Zhu [66]. We then determine y at the midpoints (2.33) by using four-point interpolation formula. The dynamic boundary condition (2.28) is satisfied by substituting these values of τ and y at the midpoints. The derivative in (2.28) is approximated at the midpoints (2.33) by using five-point finite difference formula with $O(\Delta^4)$. This yields N nonlinear algebraic equations. A radiation condition is required to close the system. Based on the direction of the flow velocity on the upstream free surface, we set

$$\theta_1 = 0. \tag{2.34}$$

In order to calculate the shape of obstacles, we define the equally spaced mesh points between the apex J_i and the downstream corner K_i of the obstacle i by

$$\phi_{i,j}^{JK} = \phi_{J_i} + (j-1)\Delta_i^{KJ}, \qquad j = 1, 2, \ldots, NB+1$$

and the midpoints by

$$\phi m_{i,j}^{JK} = \frac{\phi_{i,j}^{JK} + \phi_{i,j+1}^{JK}}{2}, \qquad j = 1, 2, \ldots, NB. \tag{2.35}$$

Here

$$\Delta_i^{KJ} = \frac{\phi_{K_i} - \phi_{J_i}}{NB},$$

and NB is an even integer. Then the values of y on the downstream $J_i K_i$ of the obstacle can be obtained by integrating numerically (2.32). This gives

$$y\left(\phi^{JK}_{i,NB+1}\right) = y\left(\phi_{K_i}\right) = 0,$$

$$y\left(\phi^{JK}_{i,j}\right) = y\left(\phi^{JK}_{i,j+1}\right) - e^{-\tau m^{JK}_{i,j}} \sin\theta^{do}_i \Delta^{KJ}_i$$

for $j = NB, NB-1, \ldots, 1$. Here $\tau m^{JK}_{i,j}$ is the value of τ at the midpoints (2.35). Similarly, we can calculate y on the upstream $I_i J_i$ of the obstacle by using equally spaced mesh points from ϕ_{I_i} and ϕ_{J_i}. The following conditions must be imposed to ensure the obstacle geometry:

$$y\left(\phi_{J_i}\right) = hob_i \tag{2.36}$$

$$\text{and} \qquad y\left(\phi_{I_i}\right) = 0, \tag{2.37}$$

for $i = 1, 2$. Here the values of ϕ_{I_i} and ϕ_{K_i} are to be found as parts of the solution for given values of ϕ_{J_i}. Values of x on the bottom are also calculated in order to find positions of obstacle on the bottom. For given values of ϕ_{J_i} the distance x_d between two obstacles is defined by

$$x_d = x(\phi_{J_2}) - x(\phi_{J_1}).$$

The values of $x(\phi_{J_2})$ and $x(\phi_{J_1})$ can be obtained by integrating numerically (2.31). In this study, we set the difference $|\phi_{J_2} - \phi_{J_1}| = 20$ or $\phi_{J_1} = -20$ for all calculations.

For given values of F, Bo, hob_1 and hob_2, we obtain the system of $N+5$ nonlinear equations for (2.28), (2.34), (2.36) and (2.37) with $N+5$ unknowns: $\theta_I, I = 1, 2, \ldots, N+1$, $\phi_{I_1}, \phi_{K_1}, \phi_{I_2}$ and ϕ_{K_2}. This system is solved by Newton's method.

Numerical accuracy is tested by varying the number of mesh points N and the mesh spacing Δ. For $N = 1600$, the computed profiles with $\Delta = 0.05$ and $\Delta = 0.10$ are shown in Figure 2.6. On the other hand, Figure 2.7 shows a
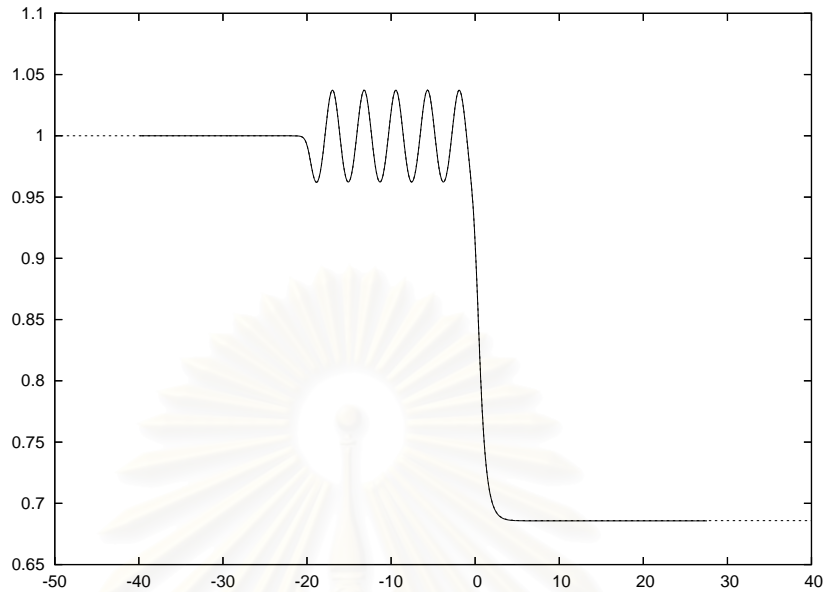
Figure 2.6: Typical free-surface profiles for $F = 0.7470, Bo = 0.0, hob_1 = 0.10$ and $hob_2 = 0.20$ when $N = 1600$. The solid line is for $\Delta = 0.05$ and the dashed line is for $\Delta = 0.10$.

comparison of computed profiles when $N = 800$ and 1600 for a fixed $\Delta = 0.10$. A quantitative examination can be conducted by defining the root mean squared error $(RMSE)$ between two free-surface profiles i and j as

$$RMSE = \sqrt{\frac{1}{M} \sum_{k=1}^{M} (y_i(x_k) - y_j(x_k))^2}.$$

The values of $RMSE$ of the results are shown in Table 2.3. In this study, we choose $N = 800$ and $\Delta = 0.10$ in all calculations.
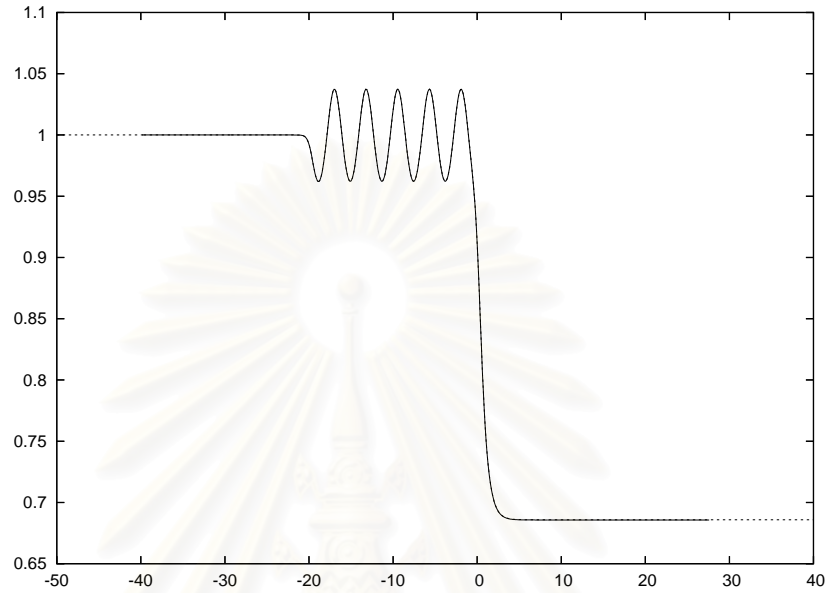
Figure 2.7: Typical free-surface profiles for $F = 0.7470, Bo = 0.0, hob_1 = 0.10$ and $hob_2 = 0.20$ when $\Delta = 0.10$. The solid line is for $N = 800$ and the dashed line is for $N = 1600$.

	$N = 1600, \Delta = 0.05$ and $N = 1600, \Delta = 0.10$	$N = 800, \Delta = 0.10$ and $N = 1600, \Delta = 0.10$
$RMSE$	1.84×10^{-4}	1.68×10^{-4}

Table 2.3: The root mean squared error $RMSE$ for the free-surface profiles with different values of N and Δ.

CHAPTER III

WEAKLY NONLINEAR PROBLEM

When the Froude number F is close to 1, water waves are generally of small amplitude and can be described by the weakly nonlinear theories. It is now very well accepted that the forced Korteweg-de Vries (fKdV) equation is an appropriate model for many applications in weakly nonlinear free-surface flow problems. The fKdV equation was used as a model equation of free-surface flows over obstacles by Akylas [2], Pratt [54], Grimshaw and Smyth [33], Shen, Shen and Sun [57], Shen and Shen [56], Shen [55], Milewski and Vanden-Broeck [50], Dias and Vanden-Broeck [16], Binder, Vanden-Broeck and Dias [9] and many others.

In this chapter, the forced Korteweg-de Vries (fKdV) equation for the steady flow and the time dependent problems of gravity-capillary free-surface flows over obstacles are formulated in §3.1. In §3.2, numerical procedure for the steady flow and time dependent problems are presented.

3.1 Derivation of the Forced Korteweg-de Vries (fKdV) Equation

Two-dimensional free-surface flows over obstacles in a channel of finite depth are considered. We assume that the fluid is inviscid and incompressible, and the flow is irrotational. Effects of gravity g and surface tension T are introduced in the free-surface condition. The flow is uniform with constant velocity U and constant

depth H at far upstream. We introduce Cartesian coordinates (x, y) with x-axis along the horizontal bottom and y-axis vertically upwards through the apex of the rightmost obstacle. Gravity is acting in the negative y-direction.

We denote the free surface by $y = H + \eta(x, t)$ where $\eta(x, t)$ is the elevation of free surface from the undisturbed flow level $y = H$ at position x and time t. The function $y = h(x)$ represents the bottom topography. The derivation is based on long wavelength and small obstacle asymptotics. The governing equations in terms of the potential function $\phi(x, y, t)$ are

$$\phi_{xx} + \phi_{yy} = 0, \qquad -\infty < x < \infty, h(x) < y < H + \eta(x, t), \qquad (3.1)$$

with dynamic and kinematic conditions at the free surface $y = H + \eta(x, t)$

$$\phi_t + \frac{1}{2}(\phi_x^2 + \phi_y^2) + g\eta - \frac{T\eta_{xx}}{(1 + \eta_x^2)^{3/2}} = 0, \qquad (3.2)$$

$$\eta_t + \phi_x \eta_x = \phi_y, \qquad (3.3)$$

and kinematic condition at the bottom $y = h(x)$

$$\phi_x h_x = \phi_y. \qquad (3.4)$$

Let's introduce the dimensionless variables

$$\phi' = \frac{\phi}{UH}, \qquad (x', y') = \frac{(x, y)}{H}, \qquad t' = \frac{U}{H}t,$$
$$\eta' = \frac{\eta}{H}, \qquad h' = \frac{h}{H}.$$

Substituting these variables into equations (3.1)-(3.4) and dropping the primes, the normalized governing equations are

$$\phi_{xx} + \phi_{yy} = 0, \qquad -\infty < x < \infty, h(x) < y < 1 + \eta(x), \qquad (3.5)$$

$$F^2 \phi_t + \frac{F^2}{2}(\phi_x^2 + \phi_y^2) + \eta - Bo\frac{\eta_{xx}}{(1 + \eta_x^2)^{3/2}} = 0, \text{ at } y = 1 + \eta(x), \qquad (3.6)$$

$$\eta_t + \phi_x \eta_x = \phi_y, \qquad \qquad \text{at } y = 1 + \eta(x), \qquad (3.7)$$

$$\phi_x h_x = \phi_y, \qquad \qquad \text{at } y = h(x). \qquad (3.8)$$

Here $F = \frac{U}{\sqrt{gH}}$ is the Froude number, $Bo = \frac{T}{\rho g H^2}$ is the Bond number.

Next, we change the variables (x, t) to the new variables (ξ, τ) by

$$\xi = \epsilon^{1/2}(x - t) \quad \text{and} \quad \tau = \epsilon^{3/2} t,$$

where $\epsilon = \left(\frac{H}{L}\right)^2 \ll 1$ is a small positive parameter, and L is the characteristic length in the long waves assumption. Equations (3.6)-(3.8) become

$$\epsilon \phi_{\xi\xi} + \phi_{yy} = 0, \qquad -\infty < \xi < \infty, h(\xi) < y < 1 + \eta(\xi, \tau), \tag{3.9}$$

$$\epsilon^{1/2} F^2 \left(\epsilon \phi_\tau - \phi_\xi\right) + \frac{F^2}{2}(\epsilon \phi_\xi^2 + \phi_y^2) + \eta - Bo\frac{\epsilon \eta_{\xi\xi}}{\left(1 + \epsilon \eta_\xi^2\right)^{3/2}} = 0, \text{ at } y = 1 + \eta(\xi, \tau),$$

$$\tag{3.10}$$

$$\epsilon^{3/2} \eta_\tau - \epsilon^{1/2} \eta_\xi + \epsilon \phi_\xi \eta_\xi = \phi_y, \qquad \text{at } y = 1 + \eta(\xi, \tau), \tag{3.11}$$

$$\epsilon \phi_\xi h_\xi = \phi_y, \qquad\qquad\qquad \text{at } y = h(\xi). \tag{3.12}$$

For small obstacle of order ϵ^2, the bottom profile can be expressed by

$$y = \epsilon^2 \bar{h}(\xi),$$

and consequently (3.12) becomes

$$\epsilon^3 \phi_\xi \bar{h}_\xi = \phi_y. \tag{3.13}$$

Asymptotically, we expand ϕ, η and F^2 as

$$\phi = \epsilon^{1/2} \left[\frac{\xi}{\epsilon} + \phi_0(\xi, y, \tau) + \epsilon \phi_1(\xi, y, \tau) + \epsilon^2 \phi_2(\xi, y, \tau) + \dots\right],$$

$$\eta = \epsilon A(\xi, \tau) + \epsilon^2 \eta_2(\xi, \tau) + \epsilon^3 \eta_3(\xi, \tau) + \dots,$$

$$F^2 = 1 + \epsilon \lambda.$$

At the free surface $y = 1 + \epsilon A + \epsilon^2 \eta_2 + \dots$, the derivatives ϕ_ξ, ϕ_τ and ϕ_z can

be expanded around $y = 1$ as

$$\phi_\xi = \epsilon^{1/2}\left[\frac{1}{\epsilon} + \phi_{0\xi} + \epsilon\left\{\phi_{1\xi} + A\phi_{0\xi y} + A_\xi\phi_{0y}\right\}\right.$$
$$\left. + \epsilon^2\left\{\phi_{2\xi} + A\phi_{1\xi y} + A_\xi\phi_{1y} + \eta_2\phi_{0\xi y} + \eta_{2\xi}\phi_{0y} + \frac{1}{2}A^2\phi_{0\xi yy} + AA_\xi\phi_{0yy}\right\} + O(\epsilon^3)\right],$$

$$\phi_\tau = \epsilon^{1/2}\left[\phi_{0\tau} + \epsilon\left\{\phi_{1\tau} + A\phi_{0\tau y} + A_\tau\phi_{0y}\right\}\right.$$
$$\left. + \epsilon^2\left\{\phi_{2\tau} + A\phi_{1\tau y} + A_\tau\phi_{1y} + \eta_2\phi_{0\tau y} + \eta_{2\tau}\phi_{0y} + \frac{1}{2}A^2\phi_{0\tau yy} + AA_\tau\phi_{0yy}\right\} + O(\epsilon^3)\right],$$

$$\phi_y = \epsilon^{1/2}\left[\phi_{0y} + \epsilon\left\{\phi_{1y} + A\phi_{0yy}\right\} + \epsilon^2\left\{\phi_{2y} + A\phi_{1yy} + \eta_2\phi_{0yy} + \frac{1}{2}A^2\phi_{0yyy}\right\} + O(\epsilon^3)\right].$$

Substituting these expansions into equations (3.9)-(3.13), we obtain a sequence of equations and boundary conditions for all order of ϵ.

At zeroth order $O(1)$:

$$\phi_{0yy} = 0$$

with
$$\phi_{0\xi} + \frac{1}{2}\phi_{0y}^2 + A = 0, \qquad \phi_{0y} = 0, \qquad \text{at } y = 1$$

and
$$\phi_{0y} = 0, \qquad \text{at } y = 0.$$

These imply that

$$\phi_0 = M(\xi, \tau),$$

and

$$A = -M_\xi.$$

At first order $O(\epsilon)$:

$$\phi_{0\xi\xi} + \phi_{1yy} = 0$$

with
$$\phi_{0\tau} - \phi_{1\xi} + \eta_2 - \lambda\phi_{0\xi} + \frac{1}{2}\phi_{0\xi}^2 - BoA_{\xi\xi} = 0, \qquad A_\xi = \phi_{1y}, \quad \text{at } y = 1$$

and
$$\phi_{1y} = 0, \qquad \text{at } y = 0.$$

These imply that

$$\phi_1 = -\frac{y^2}{2}M_{\xi\xi} + N(\xi, \tau)$$

and

$$N_\xi = M_\tau + (\frac{1}{2} - Bo)A_{\xi\xi} + \eta_2 - \lambda A + \frac{1}{2}A^2.$$

At second order $O(\epsilon^2)$:

$$\phi_{1\xi\xi} + \phi_{2yy} = 0$$

with $\qquad\qquad A_\tau - \eta_{2\xi} + A_\xi\phi_{0\xi} = \phi_{2y} + A\phi_{1yy}, \qquad$ at $y = 1$,

and $\qquad\qquad\qquad\qquad \bar{h}_\xi = \phi_{2y}, \qquad\qquad\qquad$ at $y = 0$.

We have

$$\phi_2 = \frac{y^4}{4!}M_{\xi\xi\xi} - \frac{y^2}{2}N_{\xi\xi} + \bar{h}_\xi y + P(\xi, \tau).$$

Using these $\phi_0, \phi_1, \phi_2, A$, and η_2 in the kinematic condition at $y = 1$, we obtain a relation for A on the free surface:

$$2A_\tau - 3AA_\xi + \lambda A_\xi - \left(\frac{1}{3} - Bo\right)A_{\xi\xi\xi} = \bar{h}_\xi. \qquad (3.14)$$

This equation is the well-known *forced Korteweg-de Vries (fKdV) equation*. Rewriting (3.14), we have

$$A_\tau - \frac{3}{4}\left(A^2\right)_\xi + \frac{(F^2 - 1)}{2}A_\xi - \frac{\left(\frac{1}{3} - Bo\right)}{2}A_{\xi\xi\xi} = \frac{1}{2}h_\xi. \qquad (3.15)$$

In case of steady flow problem, the time derivative in (3.15) is omitted and $\xi = x$. Upon the integration with respect to x under the condition that far upstream flow is uniform, equation (3.15) is reduced to

$$\frac{3}{2}A^2 - \left(F^2 - 1\right)A + \left(\frac{1}{3} - Bo\right)A_{xx} = -h. \qquad (3.16)$$

Equation (3.16) is called the *stationary forced Korteweg-de Vries (sfKdV) equation*.

In case of no forcing ($h \equiv 0$), equation (3.16) can be multiplied by A_x and integrated with respect to x under the far upstream constraint. In doing so, we obtain

$$\left(\frac{1}{3} - Bo\right)A_x^2 = (F^2 - 1)A^2 - A^3 + C, \qquad (3.17)$$

Physical Space   **Fourier Space**

$$\Psi_t = \mathcal{L}(\Psi) \xrightarrow{\text{FFT}} \widehat{\Psi}_t = \widehat{\mathcal{L}}(\widehat{\Psi})$$

$$\downarrow \text{RK4}$$

$$\Psi^{n+1} \xleftarrow{\text{IFFT}} \widehat{\Psi}^{n+1}$$
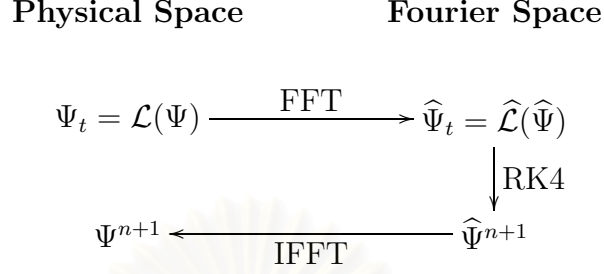
Figure 3.1: Schematic diagram of the transformations in the Fourier-PS method. Here $\mathcal{L}$ is the difference operators, the subscript t denotes time derivatives, the superscript $n+1$ indicates next time step.

where C is a constant of integration. It should be noted that, the two fixed points of equation (3.17) in the phase plane diagram correspond to $A = 0$ and $A = \frac{2}{3}(F^2 - 1)$. This shall be discussed further in chapters 4 and 5.

3.2 Numerical Procedure

Equation (3.15) can be solved numerically by using a combination of the Fourier pseudospectral method in space and the Runge-Kutta method in time. This is generally called the "*Fourier-pseudospectral*" (**Fourier-PS**) method. This method is well suited for dispersive wave problems such as (3.15). At the boundaries of domain $(-L, L)$, periodic conditions must be imposed.

Let $\widehat{A} = \widehat{A}(k, \tau)$ and $\widehat{h} = \widehat{h}(k)$ be the Fourier transform of $A(\xi, \tau)$ and $h(\xi)$, respectively. The transformed equation of (3.15) is

$$\widehat{A}_\tau = \frac{3}{4} i k \widehat{A^2} - \frac{F^2 - 1}{2} i k \widehat{A} + \frac{\frac{1}{3} - Bo}{2} (ik)^3 \widehat{A} + \frac{1}{2} i k \widehat{h}. \qquad (3.18)$$

Here k is called the *Nyquist* or *reflection* frequency or *wave number*. The numerical procedure follows closely to that of Milewski and Tabak [49]. Schematic illustration of the Fourier-PS method is depicted in Figure 3.1. First, we discretize

ξ into N equally spaced grid points $\xi_0, \xi_1, \ldots, \xi_{N-1}$ where N is an even integer. Let A_j^n denote the value of A at grid point ξ_j and time t^n, and k_j denotes the Nyquist frequency at grid point ξ_j such that

$$\left[k_0, k_1, k_2, \ldots, k_{\frac{N}{2}-1}, k_{\frac{N}{2}}, k_{\frac{N}{2}+1}, k_{\frac{N}{2}+2}, \ldots, k_{N-2}, k_N \right]$$
$$= \frac{\pi}{L} \left[0, 1, 2, \ldots, \frac{N}{2} - 1, 0, -\frac{N}{2} + 1, -\frac{N}{2} + 2, \ldots, -2, -1 \right].$$

The initial value of A_j is set as $A_j^0 = 0$, for all $j \in \{0, 1, \ldots, N-1\}$.

For given values of F, Bo and $h(\xi)$, we can find A_j^{n+1} as follows.

1. Calculate $\widehat{A_j^n}$ by the Fast Fourier Transform (FFT).

2. Use the Runge-Kutta method of order 4 (RK4) to calculate $\widehat{A_j^{n+1}}$ from equation (3.18).

3. Calculate A_j^{n+1} from $\widehat{A_j^{n+1}}$ by the inverse Fast Fourier Transform (IFFT).

To find steady flow solutions of (3.16), we solve the initial-value problem (3.16) with initial conditions

$$\lim_{x \to -\infty} A(x) = \lim_{x \to -\infty} A_x(x) = 0$$

by the RK4. First, we define a new function w such that $w(x) = A_x(x)$ satisfying a system of first-order differential equations

$$A_x = g(x, A, w) = w,$$
$$w_x = f(x, A, w) = \frac{3}{1 - 3Bo} \left[(F^2 - 1)A - \frac{3}{2}A^2 - h \right].$$

Next, we discretize the physical domain into $M + 1$ mesh points with spacing Δ. The value of A and w at x_{i+1} can be calculated from

$$A_{i+1} = A_i + \frac{1}{6}(r_1 + 2r_2 + 2r_3 + r_4),$$
$$w_{i+1} = w_i + \frac{1}{6}(k_1 + 2k_2 + 2k_3 + k_4),$$

where

$$r_1 = \Delta \cdot f(x_i, A_i, w_i), \qquad\qquad k_1 = \Delta \cdot g(x_i, A_i, w_i),$$

$$r_2 = \Delta \cdot f(x_i + \tfrac{1}{2}\Delta, A_i + \tfrac{1}{2}r_1, w_i + \tfrac{1}{2}k_1), \quad k_2 = \Delta \cdot g(x_i + \tfrac{1}{2}\Delta, A_i + \tfrac{1}{2}r_1, w_i + \tfrac{1}{2}k_1),$$

$$r_3 = \Delta \cdot f(x_i + \tfrac{1}{2}\Delta, A_i + \tfrac{1}{2}r_2, w_i + \tfrac{1}{2}k_2), \quad k_3 = \Delta \cdot g(x_i + \tfrac{1}{2}\Delta, A_i + \tfrac{1}{2}r_2, w_i + \tfrac{1}{2}k_2),$$

$$r_4 = \Delta \cdot f(x_i + \Delta, A_i + r_3, w_i + k_3), \qquad k_4 = \Delta \cdot g(x_i + \Delta, A_i + r_3, w_i + k_3).$$

A plot of A versus A_x is called *phase portrait* (phase plane or Poincaré diagram in some literatures). As we shall see later, the phase portraits can be used to explain qualitative descriptions of flow over obstacles.

CHAPTER IV

FREE-SURFACE FLOWS OVER A SINGLE OBSTACLE

In this chapter, we use the numerical procedure described in previous chapters to compute fully nonlinear and weakly nonlinear solutions of free-surface flows over a single obstacle when $Bo \geq 0$. Here we set $hob1 = 0$. Since the results are qualitatively similar for different shapes of obstacle, the isosceles triangular obstacle with the base length twice its height is considered in this study. The obstacle is classified as "bump" if $hob2 > 0$, and "dip" if $hob2 < 0$.

4.1 Flow without Surface Tension ($Bo = 0$)

Bump ($hob2 > 0$)

For subcritical flow $F < 1$, there exist two types of solutions for which the first type "SUB1" is characterized by a train of nonlinear waves behind the obstacle. This solution was earlier found by Forbes and Schwartz [27] (see Figure 4.1(a)). The second type "SUB2" is called "drag-free" or "depression wave" solution as shown in Figure 4.2(a).

As the Froude number F decreases to its critical value F_c (along the solid curve in Figure 4.6), the amplitude of the nonlinear waves of the SUB1 solution decreases and ultimately vanishes. When $F < F_c$, only the second type of solution SUB2 can be found. There is a unique critical value F_c associated with each bump size which determines the continuation of nonsymmetric (SUB1) and symmetric

(SUB2) solutions. For the corresponding phase trajectory in Figure 4.2(b), we start at the fixed point $\eta = 0$ with a downward jump onto an inner periodic orbit. After moving half circle clockwise, the orbit takes another downward jump returning to the same fixed point $\eta = 0$. It should be noted that the train of nonlinear waves on the downstream of time-dependent weakly nonlinear result does not vanishes, e.g., amplitude of the waves remains finite (see in Figure 4.2(c)). This indicates that the SUB2 solution is not stable in time. In 1982, Forbes [24] presented the SUB2 solution for flows over a semi-elliptic obstacle whose length l of obstacle is much larger than its height h, i.e., $h \ll l$. It was found that, for some values of l, the free-surface profile possesses a single "trapped wave" in the region above the obstacle (cf. Figure 2 in [24]). In the present findings, the SUB2 solution can be found for small F and the condition $h \ll l$ is irrelevant. For fully nonlinear problem, the SUB1 solution exists in the region between the dashed line with circle and the solid line with square and the SUB2 solution exists on the left of the solid line with square in Figure 4.6. Figures 4.1 (c)-(e) show the corresponding weakly nonlinear solutions of SUB1.

For supercritical flow $F > 1$, there is a two-parameter family of solutions depending on the height of obstacle $hob2$ and the Froude number F which is similar to the case of subcritical flow. The profiles are symmetric with respect to the obstacle center ($x = 0$). This solution is characterized by an elevation wave associated with the bump. Two types of supercritical solutions can be found for which one is a perturbation of uniform flow (Forbes and Schwartz [27]), the so-called "SUP1", where as the other is a perturbation of a solitary wave (Vanden-Broeck [60]), the so-called "SUP2". Typical free-surface profiles of SUP1 and SUP2 are shown in Figure 4.3(a) for $hob2 = 0.30$ and $F = 1.35$. The solid curve is a profile of SUP1 solution and the dotted curve is a profile of SUP2

(a)

(b)

(c)

(d)

(e)

Figure 4.1: Typical free-surface profiles of SUB1 for a bump. (a) Fully nonlinear profile for $F = 0.70$ and $hob2 = 0.10$. (b) Plot of $y - 1$ versus $\frac{dy}{dx} = \tan\theta$ of the fully nonlinear phase trajectory. (c) Weakly nonlinear profile. (d) Weakly nonlinear phase portrait. (e) Time evolution of the SUB1 solution.

(a)

(b)

(c)

Figure 4.2: Typical free-surface profiles of SUB2 for a bump. (a) Fully nonlinear profile for $F = 0.20$ and $hob2 = 0.10$. (b) Plot of $y - 1$ versus $\frac{dy}{dx} = \tan \theta$ of the fully nonlinear phase trajectory. (c) Time evolution of the SUB2 solution.

solution. Fully nonlinear phase trajectories of these solutions are illustrated in Figure 4.3(b). The solid and dotted curves represent trajectories of SUP1 and SUP2, respectively. Figure 4.3(c) is a solution profile of time-dependent fKdV equation for $hob2 = 0.30$ and $F = 1.35$ with zero initial condition $(A(\xi, 0) = 0)$. This solution is SUP1 solution type. The flow is strong enough that all transient waves are swept downstream so that the free surface with elevated profile in the vicinity of the obstacle remains stationary. For SUP2 solution type, Choi *et al.* [13] employed the initial condition

$$A(\xi, 0) = (F^2 - 1 - c)\text{sech}^2\left\{\sqrt{3(F^2 - 1 - c)}(\xi - \xi_0)/2\right\}$$

to calculate the SUP2 time dependent fKdV solution (cf. Figure 10 in [13]). Here c is the wave speed, and ξ_0 is the phase shift.

Unlike these flow regimes, when the Froude number is close to its critical value $F = 1$, the solution of flow over an obstacle depends only on one parameter. If the obstacle height $hob2$ is chosen as parameter, then the Froude number F shall be part of the solution. This type of solution is traditionally called the "hydraulic fall" and denoted by "CRI" in this thesis. Typical fully nonlinear free-surface profile is shown in Figure 4.4(a). A qualitative comparison between weakly nonlinear phase space in Figure 4.4(d) and fully nonlinear trajectory in Figure 4.4(b) shows good agreement. As the height of the obstacle increases, flow near the obstacle apex possesses similar behavior as the case of flow over a wedge (see Figure 4.5). From the numerical calculations, it is found that the hydraulic fall solutions exist on the basis of one-to-one correspondence of the Froude number and the height of obstacle which lies on the dashed line with circle in Figure 4.6.

Regions of existence of different types of solutions are illustrated in Figure 4.6. In summary, for pure gravity flow $(Bo = 0)$ over a bump, there exist two types of subcritical and supercritical flows, and a one-to-one correspondence of F

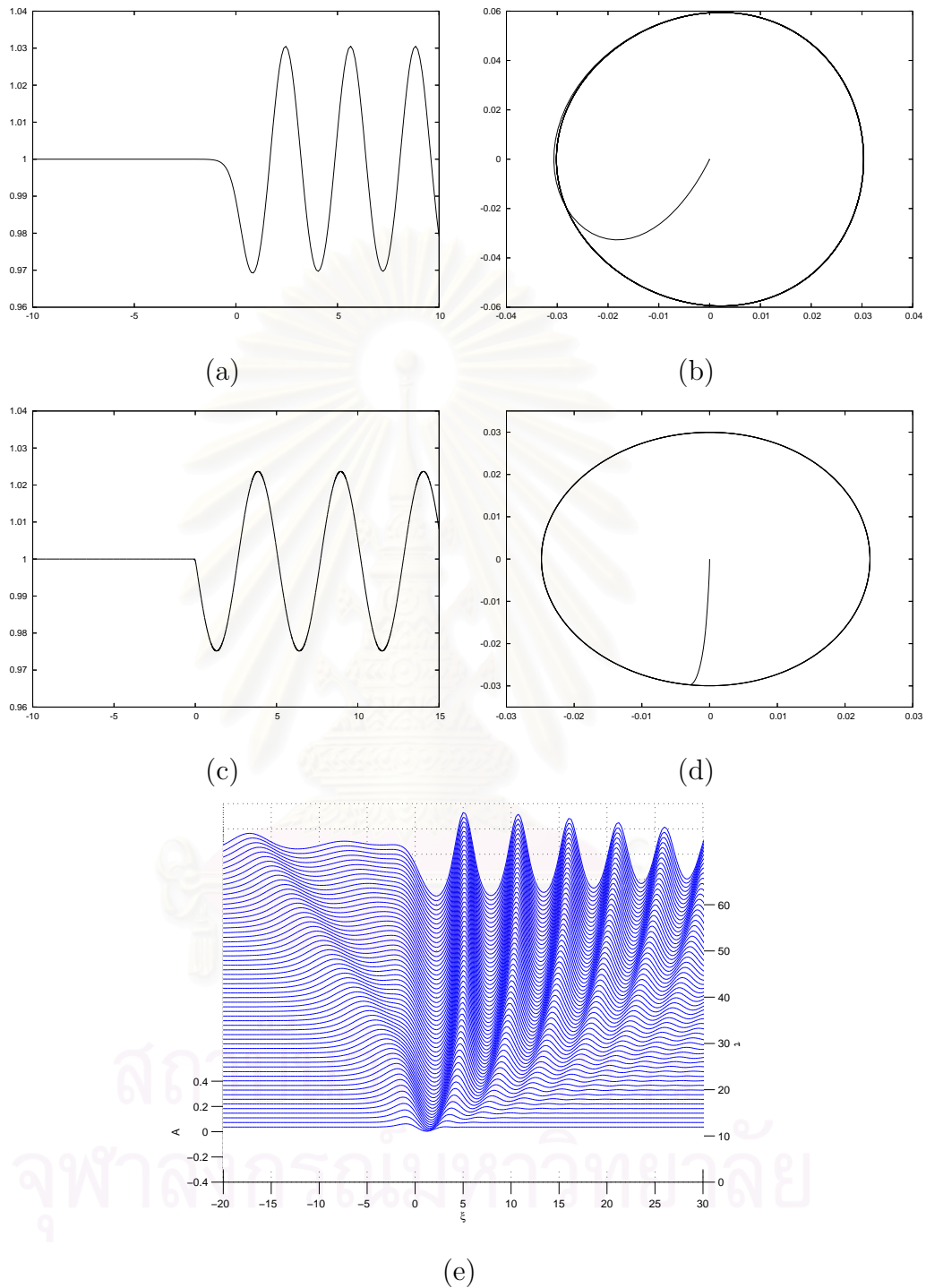Figure 4.3: Typical free-surface profiles of supercritical flow over a bump. (a) Fully nonlinear profile for $F = 1.35$ and $hob2 = 0.30$. (b) Plot of $y - 1$ versus $\frac{dy}{dx} = \tan \theta$ of the fully nonlinear phase trajectories. The solid curve is a profile of SUP1 solution and the dotted curve is a profile of SUP2 solution. (c) Time evolution of the solution for $F = 1.50$ and $hob2 = 0.30$.
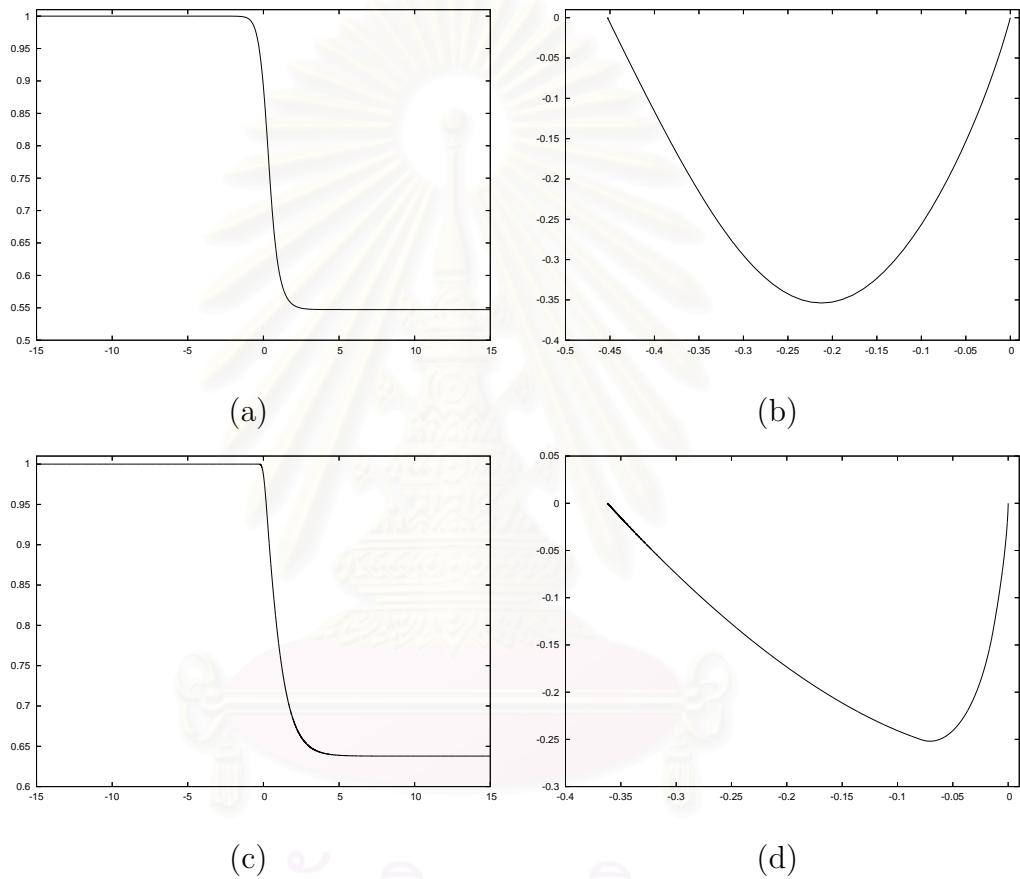
Figure 4.4: Typical free-surface profiles of critical flow over a bump for $hob2 = 0.30$. (a) Fully nonlinear profile with $F = 0.622$. (b) Plot of $y - 1$ versus $\frac{dy}{dx} = \tan\theta$ of the fully nonlinear phase trajectory. (c) Weakly nonlinear profile with $F = 0.676$. (d) Weakly nonlinear phase portrait.
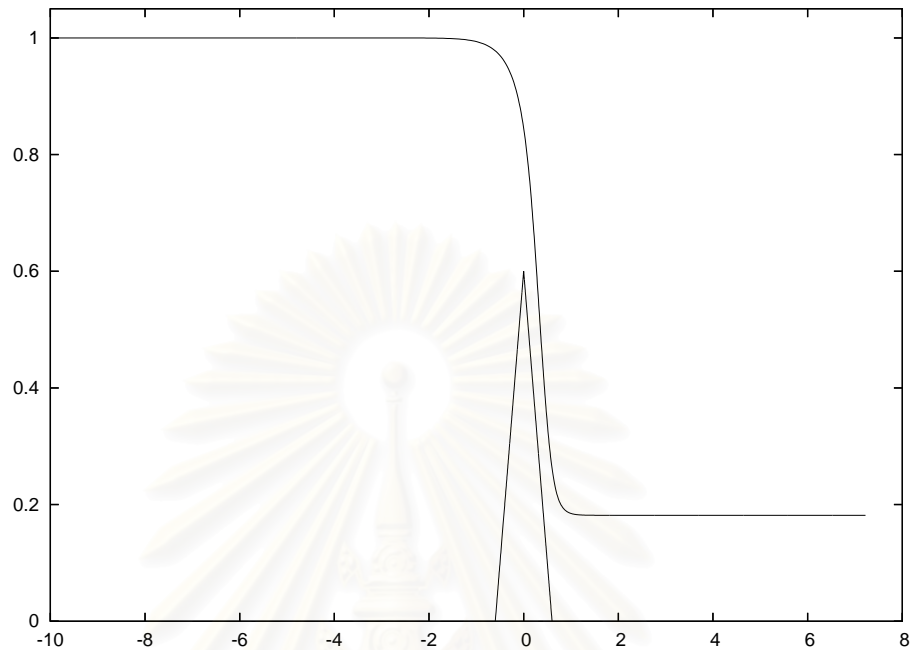
Figure 4.5: Typical free-surface profile of the critical flow with $F = 0.2356$ for $hob2 = 0.60$.
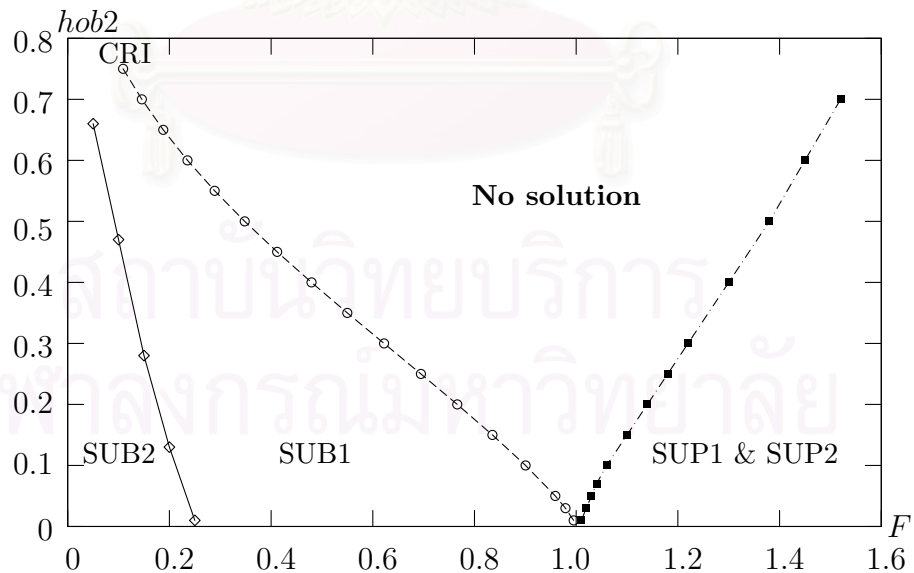
Figure 4.6: Solution diagram in $(F, hob2)$-plane of free-surface flows over a single bump. The horizontal axis is the Froude number F and the vertical axis is the dimensionless height of the rightmost obstacle $hob2$.

and $hob2$ for the hydraulic fall solutions.

Dip $(hob2 < 0)$

For subcritical flow, there exist two types of solutions for which one is characterized by a train of nonlinear waves and shall be called "SUB1", and the other by an elevation wave and shall be referred as "SUB2". The SUB1 solution is shown in Figure 4.7(a) for $F = 0.60$ and $hob2 = -0.20$. A train of nonlinear wave on the downstream of obstacle is similar to the bump case except in the dip region where the free surface is uplifted. A comparison of fully nonlinear and weakly nonlinear phase trajectories in Figure 4.7 (b) and (d) shows qualitatively good agreement. The SUB2 solution takes on the form of symmetric elevation wave with respect to the obstacle center. Typical fully nonlinear profile of SUB2 is shown in Figure 4.8(a).

For supercritical flow, there exists a unique depression wave solution which can be viewed as perturbation of a uniform stream as shown in Figure 4.9(a) and shall be called "SUP". All of the above solutions of flows over a dip are found to be qualitatively in good agreement with the weakly nonlinear results as shown in Figures 4.7-4.9 (c), respectively.

In case of critical flow, the upstream free surface is elevated in the region of dip and followed by a hydraulic fall on the downstream of the obstacle and shall be referred as "CRI". Typical profile of this CRI solution for $F = 0.82$ and $hob2 = -0.45$ is shown in Figure 4.10(a). A qualitative comparison of fully nonlinear and weakly nonlinear phase trajectories in Figure 4.10 (b) and (d) shows good agreement. Figure 4.10(c) shows a weakly nonlinear solution for $F = 0.79$ and $hob2 = -0.25$. For the time-dependent fKdV solution, there is a periodic generation of upstream waves, and a hydraulic fall over the obstacle (see Figure
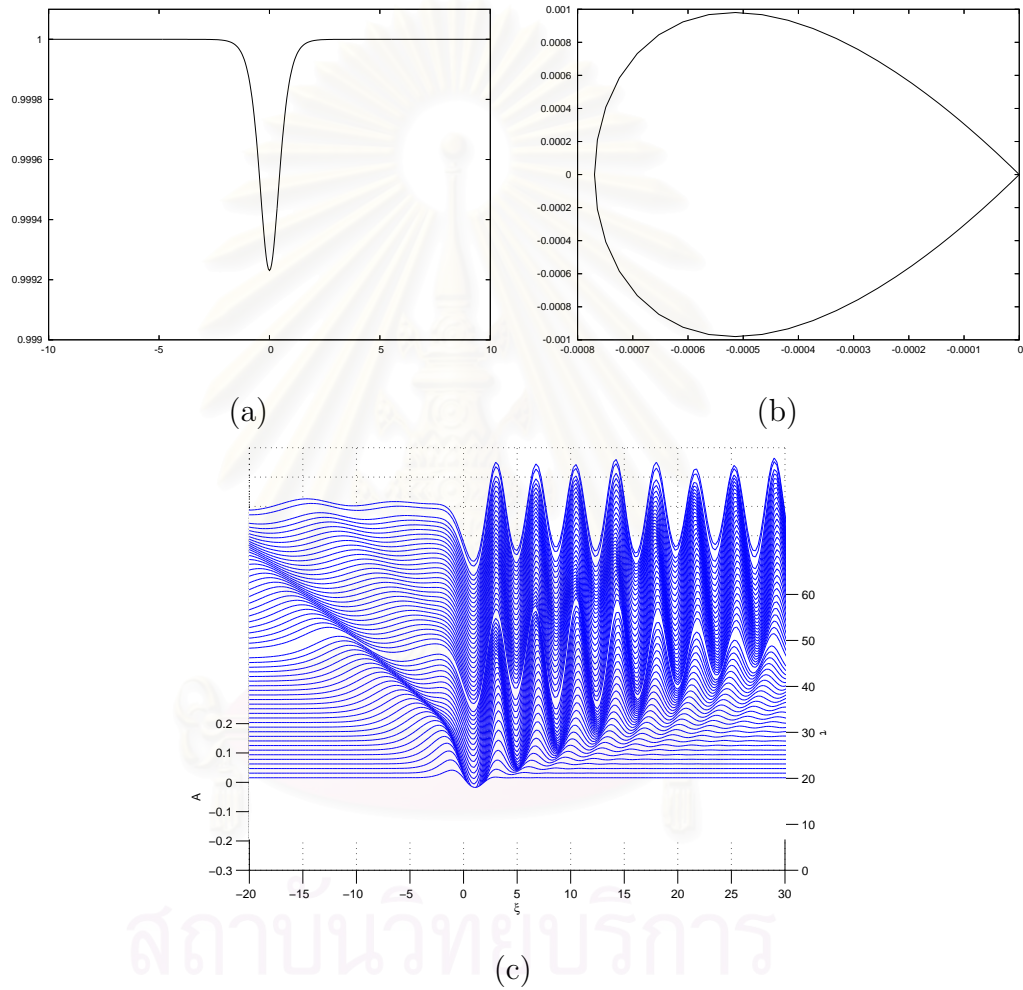
(a)

(b)

(c)

(d)

(e)

Figure 4.7: Typical free-surface profiles of SUB1 for a dip. (a) Fully nonlinear profile for $F = 0.60$ and $hob2 = -0.20$. (b) Plot of $y - 1$ versus $\frac{dy}{dx} = \tan\theta$ of the fully nonlinear phase trajectory. (c) Weakly nonlinear profile for $F = 0.60$ and $hob2 = -0.11$. (d) Weakly nonlinear phase portrait. (e) Time evolution of the SUB1 solution for $F = 0.60$ and $hob2 = -0.20$.

(a)

(b)

(c)
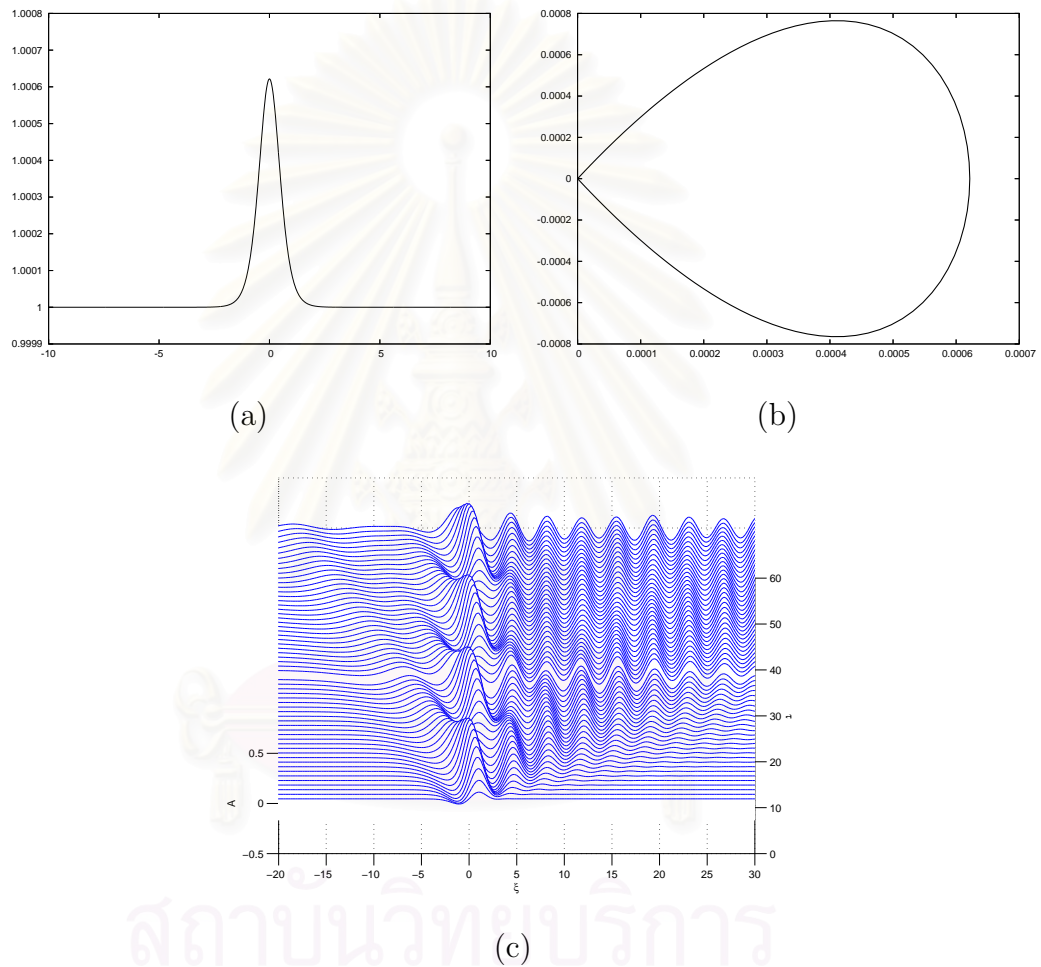
Figure 4.8: Typical free-surface profiles of SUB2 for a dip. (a) Fully nonlinear profile for $F = 0.20$ and $hob2 = -0.20$. (b) Plot of $y - 1$ versus $\frac{dy}{dx} = \tan\theta$ of the fully nonlinear phase trajectory. (c) Time evolution of the SUB2 solution.
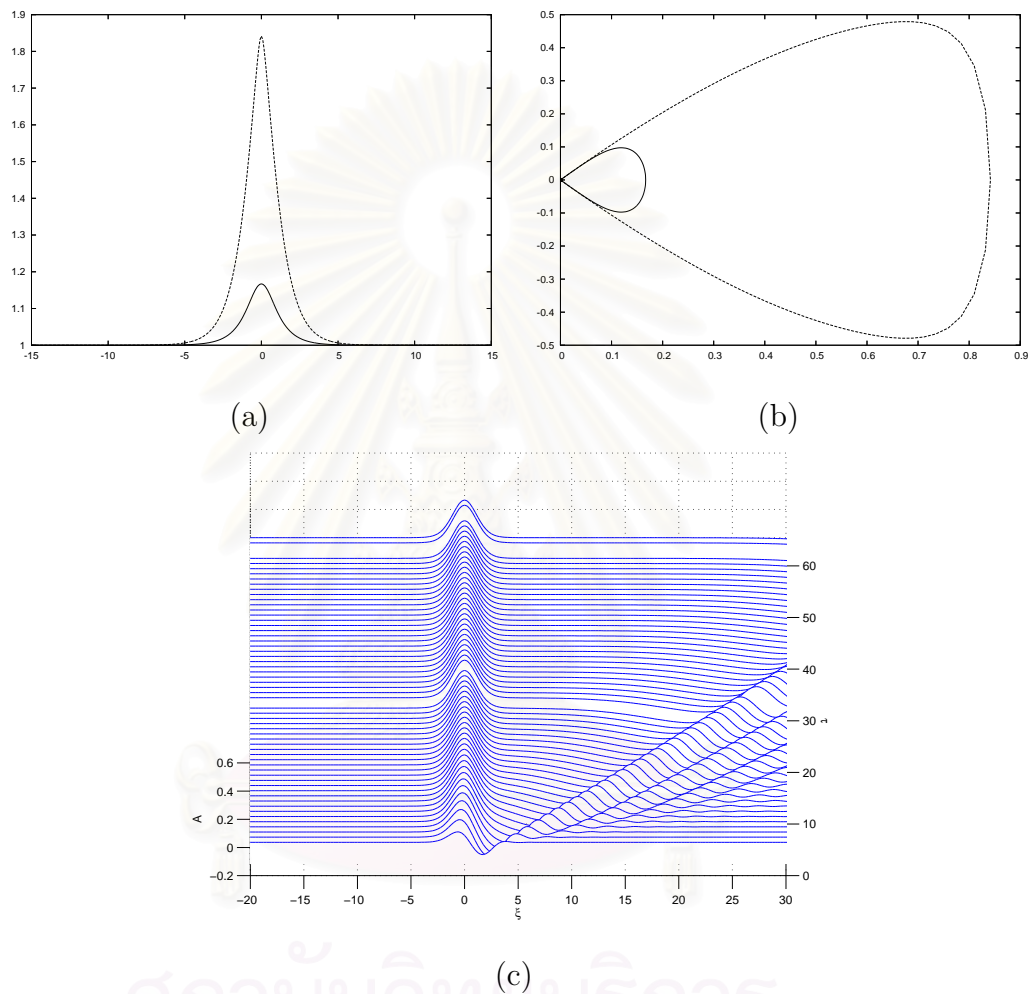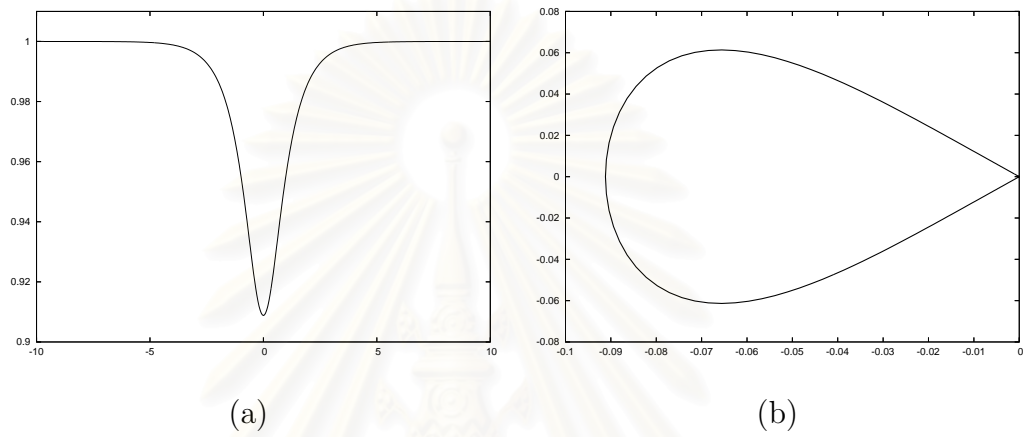
(a)

(b)
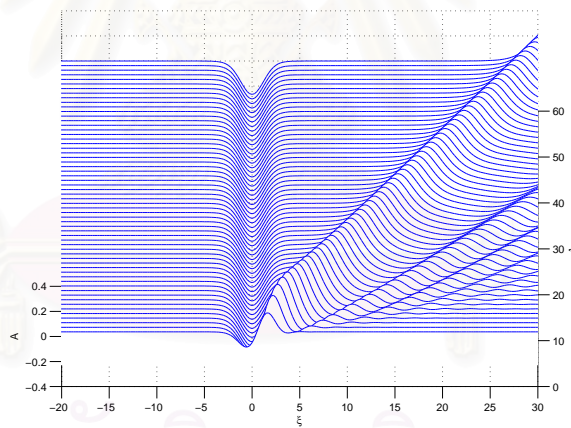
(c)

Figure 4.9: Typical free-surface profiles of supercritical flow over a dip. (a) Fully non-linear profile for $F = 1.50$ and $hob2 = -0.50$. (b) Plot of $y - 1$ versus $\frac{dy}{dx} = \tan\theta$ of the fully nonlinear phase trajectory. (c) Time evolution of the SUP solution.

4.10(e)). Figure 4.11 illustrates regions of existence of solutions for subcritical, supercritical, and critical flow regimes in the presence of a dip.

4.2 Flow under Gravity and Surface Tension ($Bo > 0$)

When surface tension is considered together with gravity in the problem, there is an additional parameter *Bond number Bo* that can play significant role on small amplitude waves. For flows over a single obstacle, solutions are found to be qualitatively similar to the case of gravity flow.

Bump ($hob2 > 0$)

For subcritical flow, the solution with downstream waves was previously proposed by Forbes [22]. His solution contained nonphysical waves of small amplitude on the upstream side. In our computation, upstream radiation condition is imposed to remove these unwanted numerical phenomenon. In Figure 4.12(a), the amplitude of a train of nonlinear waves increases with decreasing wavelength as the Bond number increases for the SUB1 solution. Comparison of weakly nonlinear and fully nonlinear solutions with the phase trajectories are shown in Figure 4.12. Typical profiles of nonlinear free surface of the SUB2 solution, when $F = 0.50$ and $hob2 = 0.15$, is shown in Figure 4.13(a). It is found that solution for small Bond number exhibits a sharper trough at $x = 0$ than those of large Bond number. As shown in Figure 4.14, the effect of surface tension can be seen from the amplitude of downstream waves. In particular, subcritical flow solution changes from SUB1 to SUB2 as the Bond number increases.

Effect of surface tension on supercritical flow regime, SUP1 and SUP2, are shown in Figure 4.15-4.17, respectively. The maximum free-surface elevation for $hob2 = 0.10$ is slightly greater than that obtained in the case $Bo = 0$ of SUP1
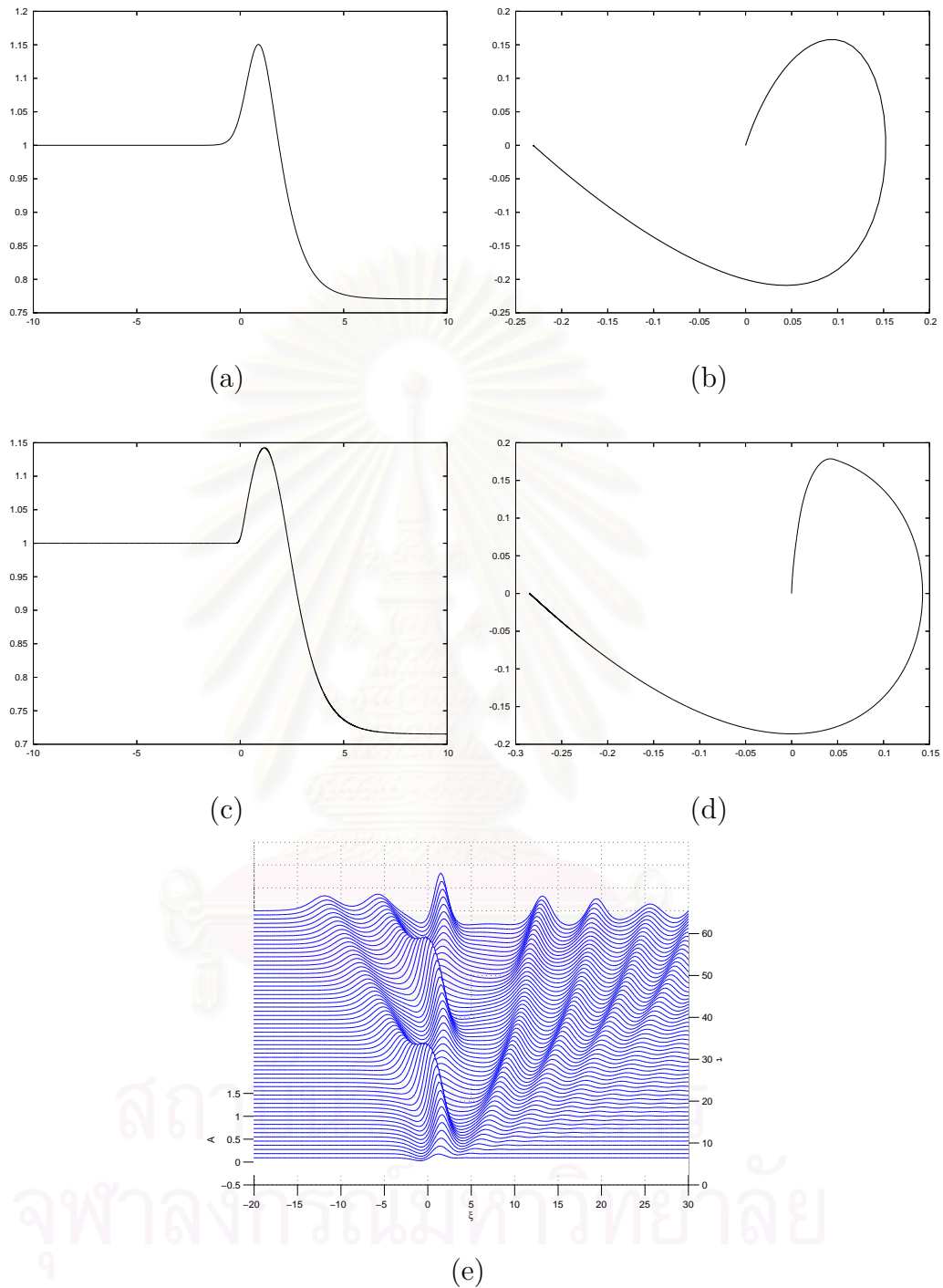
Figure 4.10: Typical free-surface profiles of critical flow over a dip. (a) Fully nonlinear profile for $F = 0.82$ and $hob2 = -0.45$. (b) Plot of $y - 1$ versus $\frac{dy}{dx} = \tan\theta$ of the fully nonlinear phase trajectory. (c) Weakly nonlinear profile f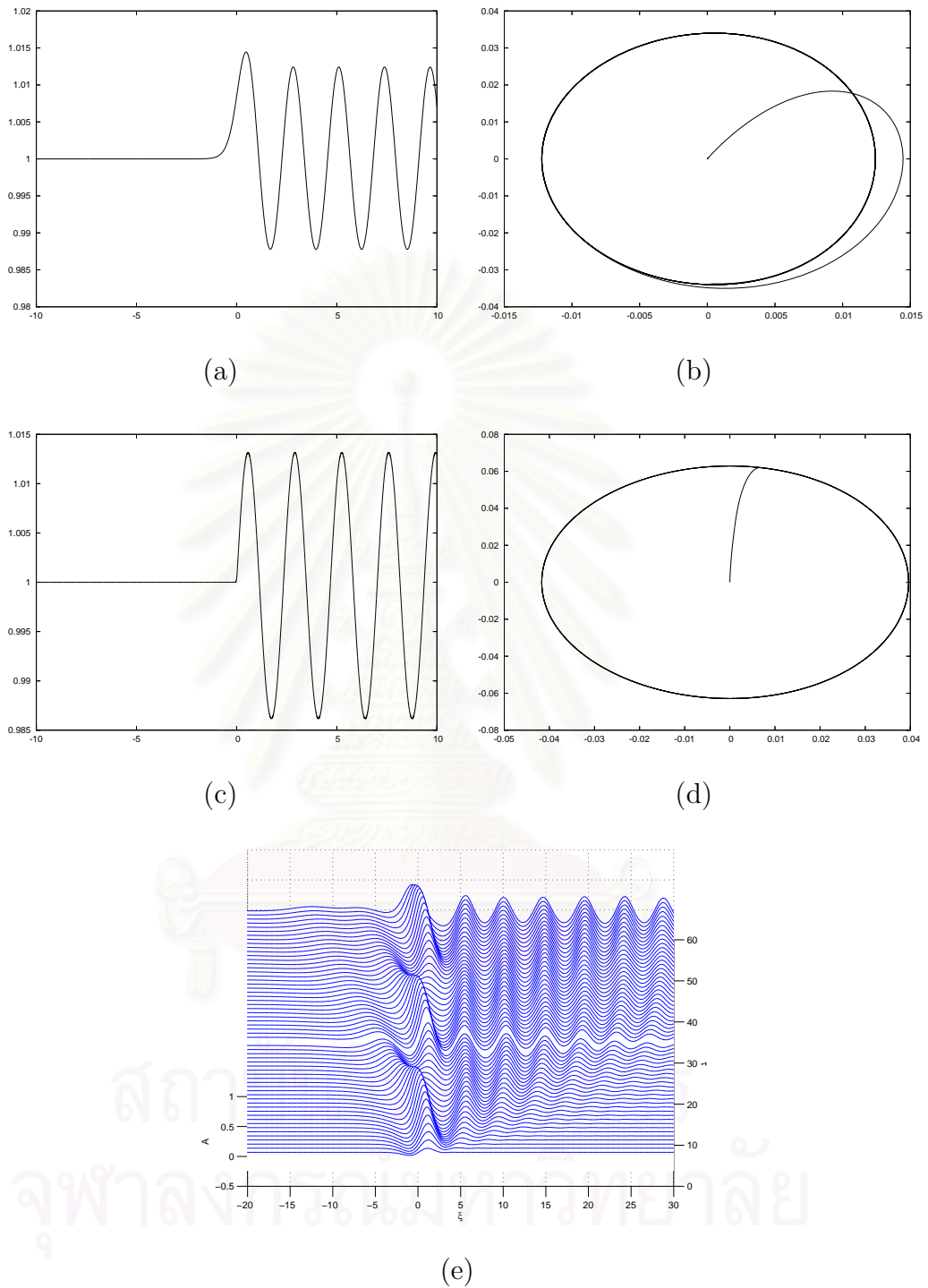or $F = 0.79$ and $hob2 = -0.25$. (d) Weakly nonlinear phase portrait. (e) Time evolution of the critical solution for $F = 0.90$ and $hob2 = -0.25$.
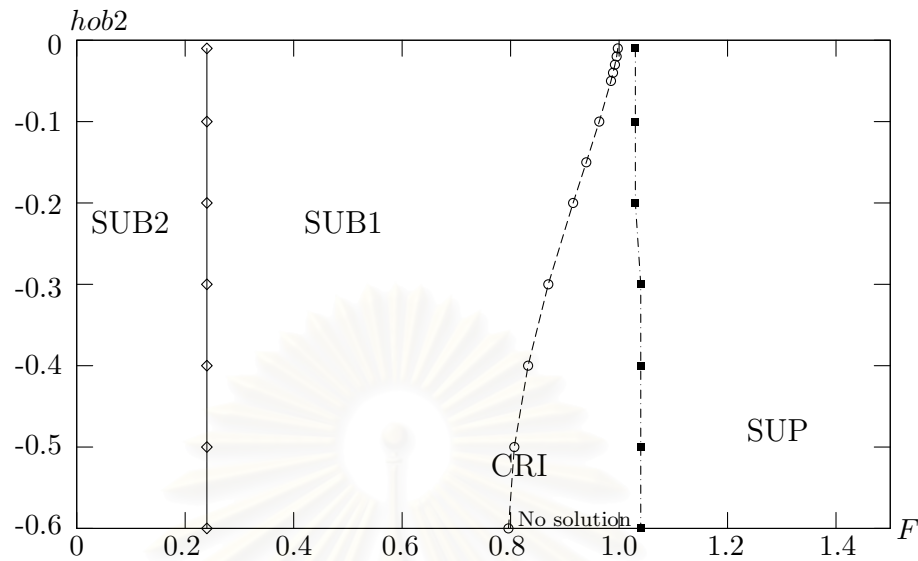
Figure 4.11: Solution diagram in $(F, hob2)$-plane of free-surface flows over a single dip. The horizontal axis is the Froude number F and the vertical axis is the dimensionless height of the rightmost obstacle $hob2$. The Froude number on solid line with square and dash-pointed line are 0.24 and 1.04, respectively.

solution (see Figure 4.15). This behavior is similar to the results of Forbes [22]. For the SUP2 solution, nonuniformity of the surface tension effect is found in the numerical results. That is, the maximum level of elevation wave increases when the height of obstacle is small (see Figure 4.16) but decreases when the height of obstacle is large (see Figure 4.17) as the Bond number increases in both cases.

For a given Bond number, free-surface profile on upstream side of critical flows changes from the flat profile to the shape of half wave packet as $hob2$ decreases to its critical height hob^* (see Figure 4.18(a)). For $hob2 < hob^*$, critical solution does not exist. Fully nonlinear phase trajectories of these results are shown in Figure 4.18(b). The trajectory starts at the fixed point $\eta = 0$. It then jumps downwards to the solitary wave orbit and returns to the fixed point $\eta = \frac{2}{3}(F^2 - 1)$. Figure 4.18(c) shows the effect of surface tension for a given value of $hob2$. Similar behavior can also be found as in the previous case for a given
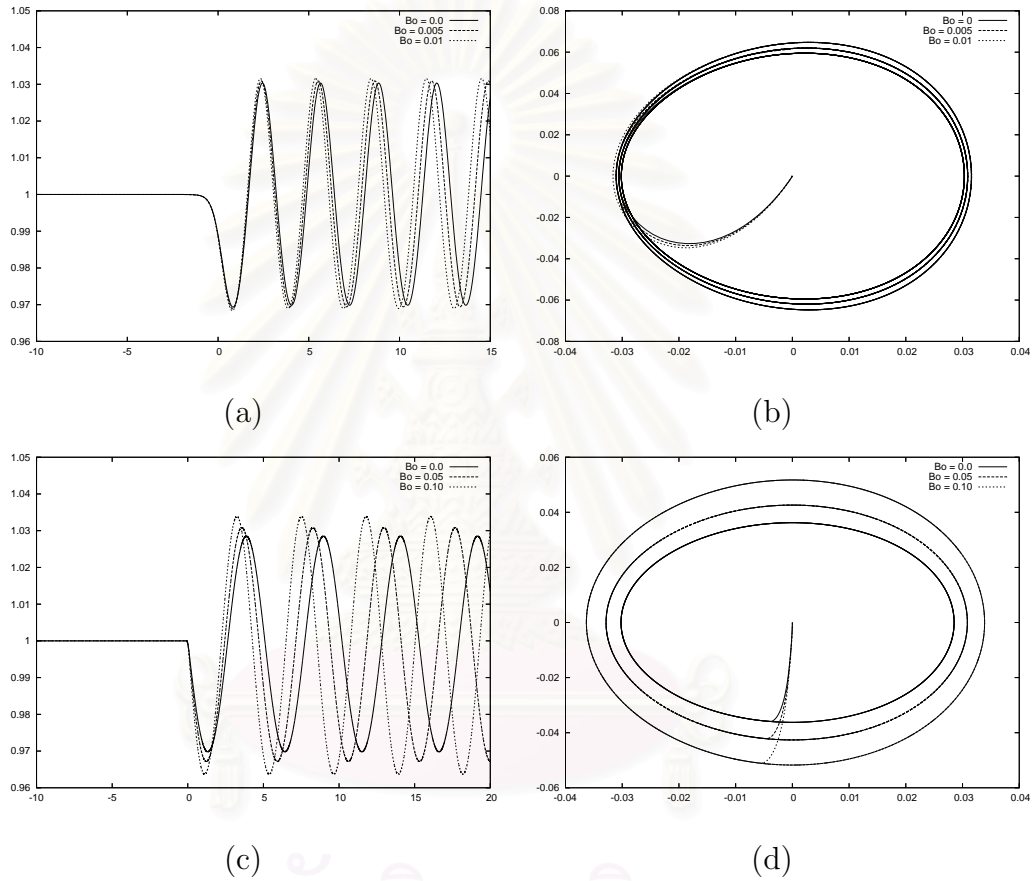
Figure 4.12: Typical free-surface profiles of SUB1 for a bump. (a) Fully nonlinear profiles for $hob2 = 0.10, F = 0.70$ and $Bo = 0, 0.005$ and 0.01. (b) Plots of $y - 1$ versus $\frac{dy}{dx} = \tan\theta$ of the fully nonlinear phase trajectories. (c) Weakly nonlinear profiles for $hob2 = 0.11, F = 0.70$ and $Bo = 0, 0.05$ and 0.10. (d) Weakly nonlinear phase portraits.
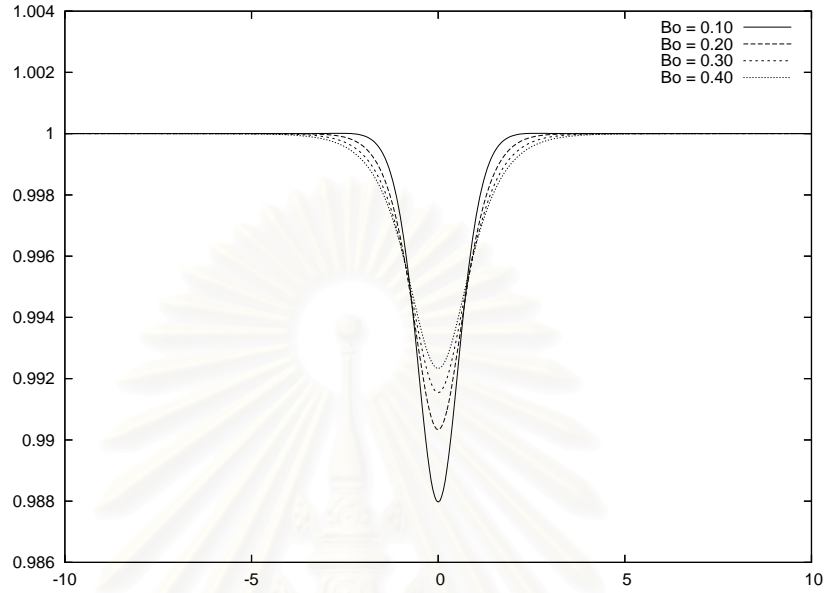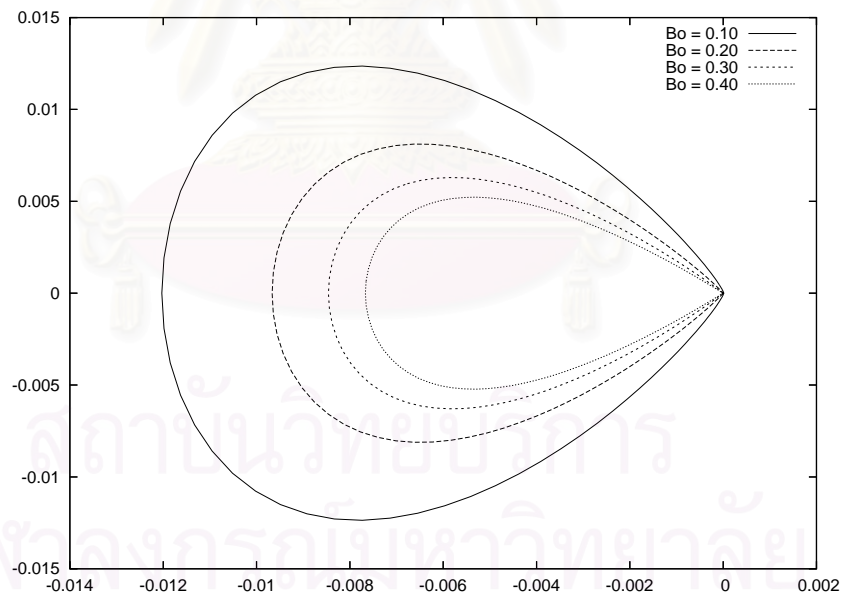
Figure 4.13: Typical free-surface profiles of SUB2 for a bump. (a) Fully nonlinear profiles for $hob2 = 0.15, F = 0.50$ and $Bo = 0.10, 0.20, 0.30$ and 0.40. (b) Plots of $y - 1$ versus $\frac{dy}{dx} = \tan\theta$ of the fully nonlinear phase trajectories.

(a) $Bo = 0$

(b) $Bo = 0.20$

(c) $Bo = 0.40$

(d) $Bo = 0.70$
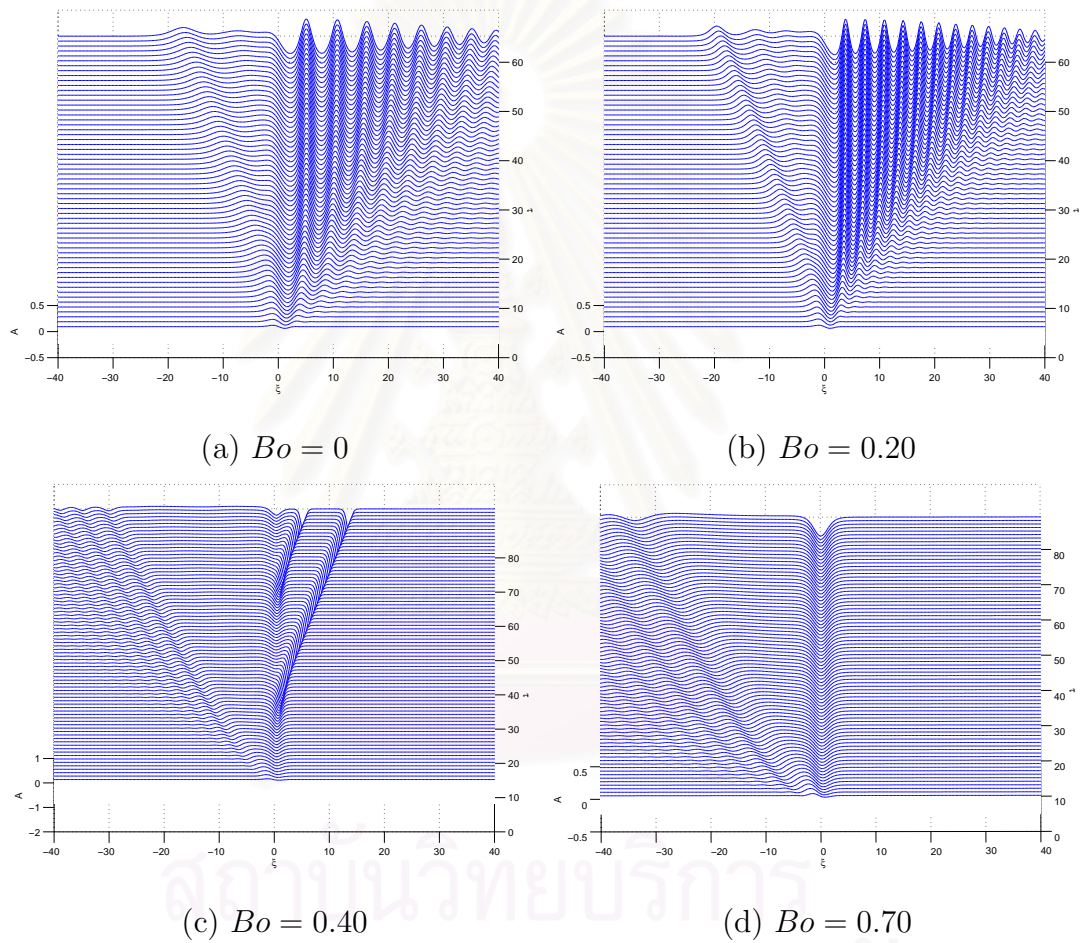
Figure 4.14: Time evolution of gravity-capillary subcritical solutions for $hob2 = 0.10$ and $F = 0.70$.

(a)

(b)

Figure 4.15: Typical free-surface profiles of SUP1 for a bump. (a) Fully nonlinear profiles for $F = 1.20, hob2 = 0.25$ and $Bo = 0, 0.05$ and 0.10. (b) Plots of $y - 1$ versus $\frac{dy}{dx} = \tan\theta$ of the fully nonlinear phase trajectories.
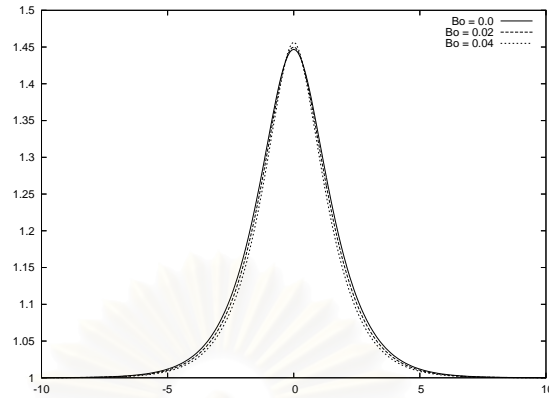
(a)
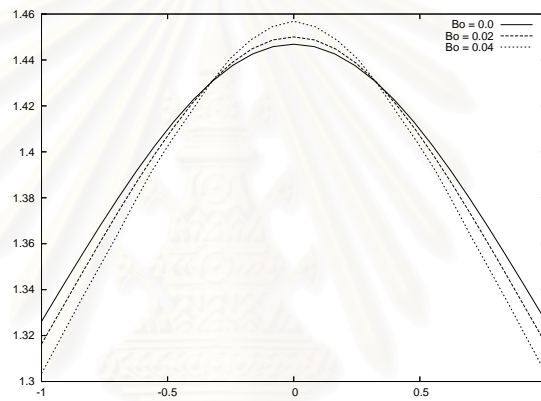
(b)
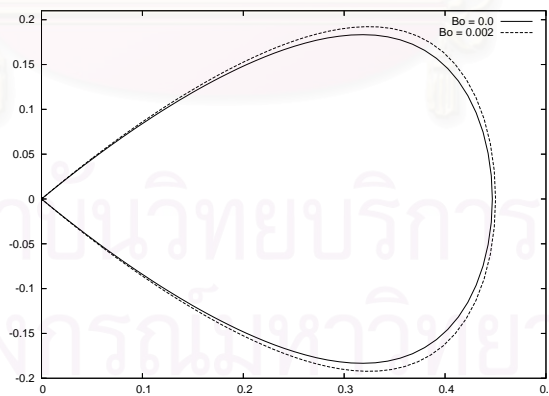
(c)

Figure 4.16: Typical free-surface profiles of SUP2 when $F = 1.20$ and $hob2 = 0.10$. (a) Fully nonlinear profiles for $Bo = 0.0, 0.02$ and 0.04. (b) Free-surface profiles in the vicinity of the obstacle. (c) Plots of $y - 1$ versus $\frac{dy}{dx} = \tan \theta$ of the fully nonlinear phase trajectories.

(a)

(b)

(c)

Figure 4.17: Typical free-surface profiles of SUP2 when $F = 1.20$ and $hob2 = 0.25$. (a) Fully nonlinear profiles for $Bo = 0.0, 0.02$ and 0.04. (b) Free-surface profiles in the vicinity of the obstacle. (c) Plots of $y - 1$ versus $\frac{dy}{dx} = \tan\theta$ of the fully nonlinear phase trajectories.

(a) $Bo = 0.10$

(b)

(c) $hob = 0.20$.

(d)
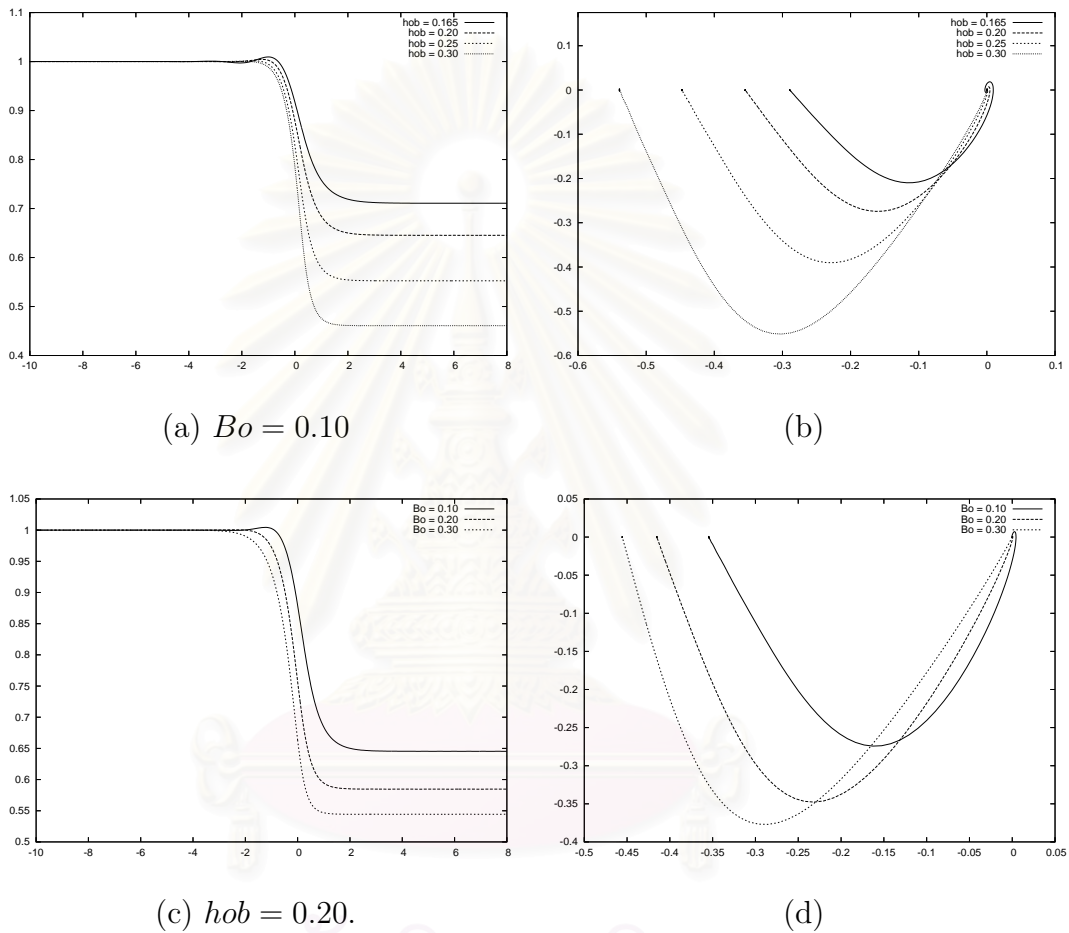
Figure 4.18: Typical free-surface profiles of critical flows. (a) Fully nonlinear profiles for $Bo = 0.10$ and $hob2 = 0.165, 0.20, 0.25, 0.30$. The critical height hob^* is 0.165. (b) Plots of $y - 1$ versus $\frac{dy}{dx} = \tan\theta$ of the fully nonlinear phase trajectories. (c) Fully nonlinear profiles for $hob2 = 0.20$ and $Bo = 0.10, 0.20, 0.30$. The critical Bond number Bo^* is 0.10. (d) Plots of $y - 1$ versus $\frac{dy}{dx} = \tan\theta$ of the fully nonlinear phase trajectories.
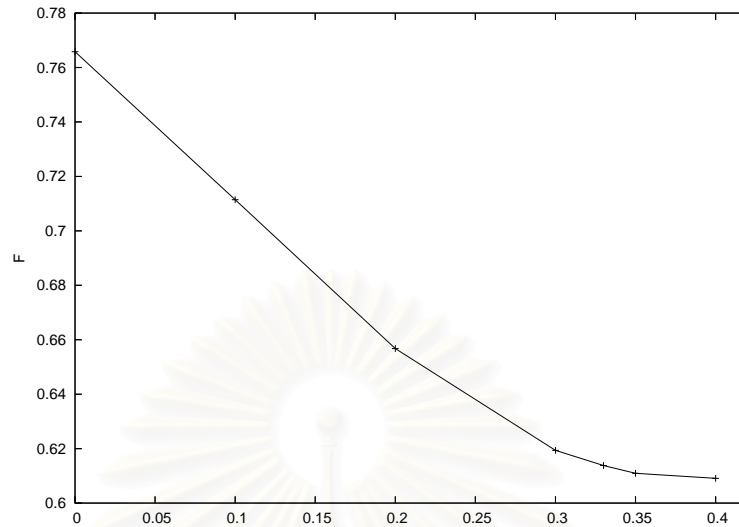
Figure 4.19: Relationship between the Froude number F and the Bond number Bo of critical free-surface flows over a bump for $hob2 = 0.20$.

Bond number with various values of the height of obstacle. In particular, when the Bond number decreases to its critical value Bo^*, the profile on upstream side change from the flat profile to the shape of half wave packet. It is found that the Froude number F, which is part of the solution, is a decreasing function of the Bond number Bo. Figure 4.19 shows the relationship between the Froude number F and the Bond number Bo for $hob2 = 0.20$. Weakly nonlinear results and weakly nonlinear phase portraits for critical flows are shown in Figure 4.20(a) and (b) for $hob2 = 0.10$ and $Bo = 0.10, 0.20$ and 0.30, respectively. It should be noted that the free-surface profile on upstream side of weakly nonlinear solution does not change from the flat profile to the shape of half wave packet.

Dip $(hob2 < 0)$

For given values of $hob2$ and F, the amplitude and wavelength of the SUB1 solution over a dip decrease as the Bond number increases. Typical free-surface profiles are shown in Figure 4.21(a). This solution can be found only for small values of
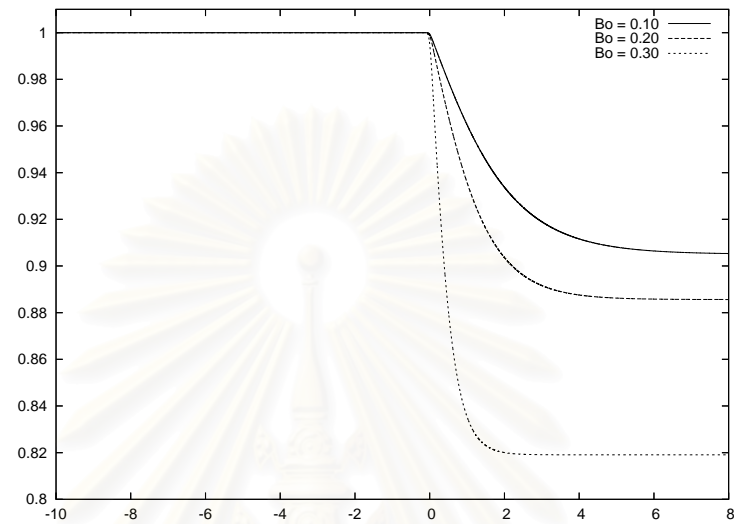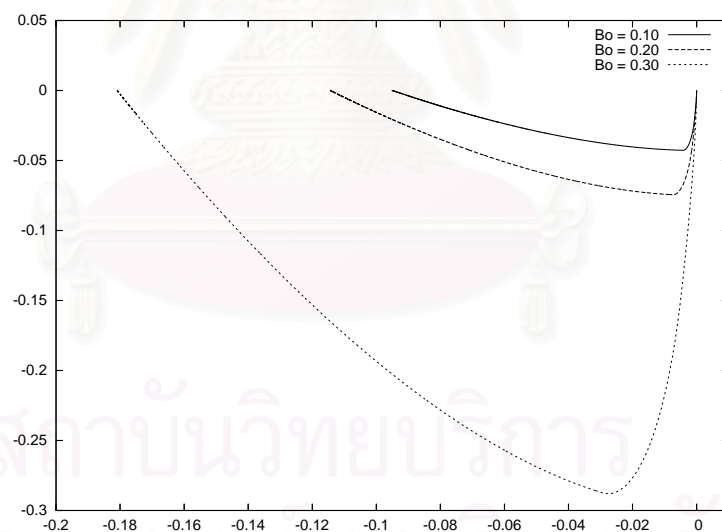
Figure 4.20: Weakly nonlinear free-surface profiles of critical flow over a bump. (a) Weakly nonlinear profiles for $hob2 = 0.10$ and $Bo = 0.10, 0.20$, and 0.30. (b) Plots of A versus A_x of the weakly nonlinear phase portraits.

the Bond number. When the Bond number increases ($Bo = 0.05 \rightarrow 0.19$), the maximum wave elevation over a dip for the SUB2 solution decreases (see Figure 4.21(c)). In particular, as the Bond number increases, solution type of the subcritical flows over a dip changes from SUB1 to SUB2 which is similar to the case of flows over a bump (see Figure 4.22).

In case of supercritical free-surface flows over a dip, surface tension plays a role on the amplitude of the depression wave as shown in Figure 4.23(a). The minimum level of flow over a dip is found to be a decreasing function of the Bond number. Figure 4.23(b) shows the phase trajectories of fully nonlinear solutions of supercritical flows over a dip for various values of Bo. Each phase trajectory starts from a fixed point $\eta = 0$ with downstream jump onto a solitary wave orbit. After moving clockwise along the solitary wave orbit, we have another downward jump returning to the same fixed point $\eta = 0$. As Bo increases, the diameter of solitary wave orbit increases with the implication of the decreasing value of the minimum level of flow.

In case of critical flow, as the Bond number increases, the maximum wave elevation over a dip increases whereas the far downstream level decreases as shown in Figure 4.24(a). Typical profile of weakly nonlinear solution and its phase space are illustrated in Figure 4.24 (c) and (d), respectively. Here, the Froude number F is treated as part of the solution which is an inverse proportion of the far downstream free surface elevation. Figure 4.25 shows that the Froude number is a decreasing function of the Bond number that is similar to the case of flows over a bump.
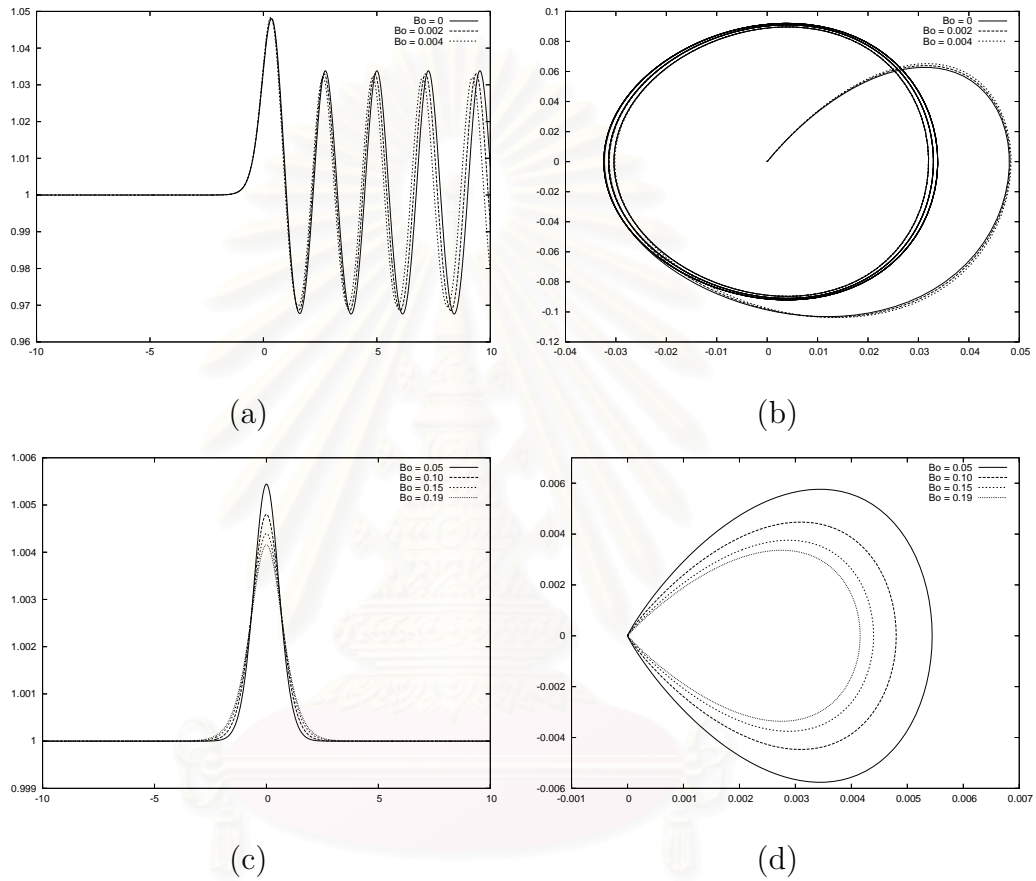
Figure 4.21: Typical free-surface profiles of SUB1 and SUB2 for gravity-capillary waves over a dip. (a) Fully nonlinear profiles of SUB1 for $hob2 = -0.40, F = 0.60$ and $Bo = 0.0, 0.002$ and 0.004. (b) Plots of $y - 1$ versus $\frac{dy}{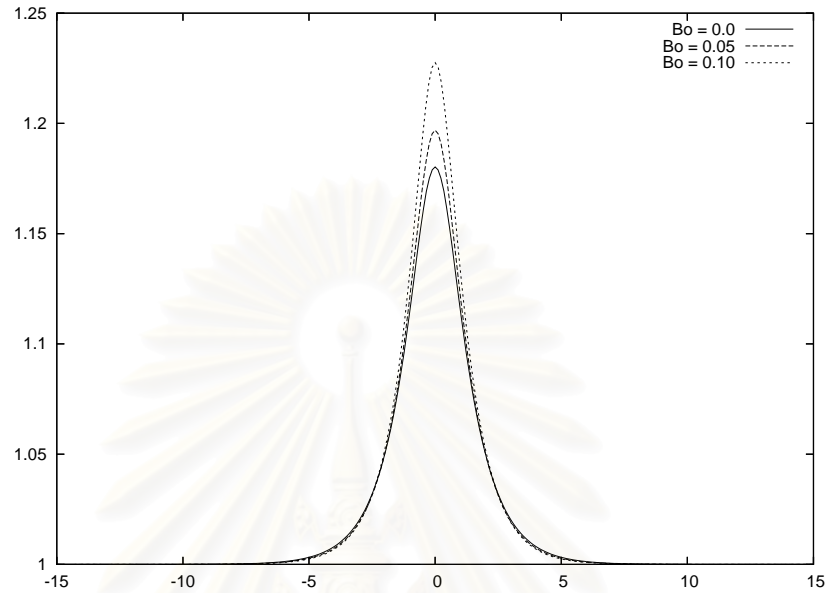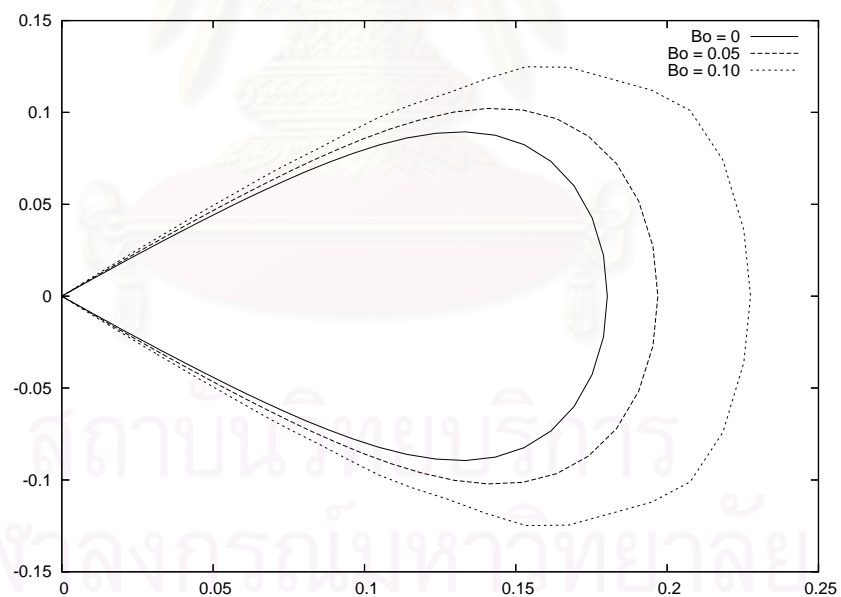dx} = \tan\theta$ of the fully n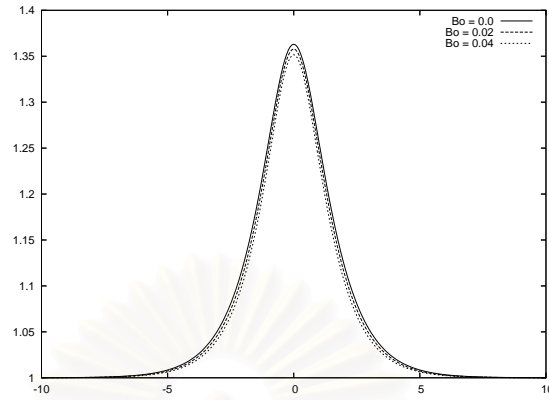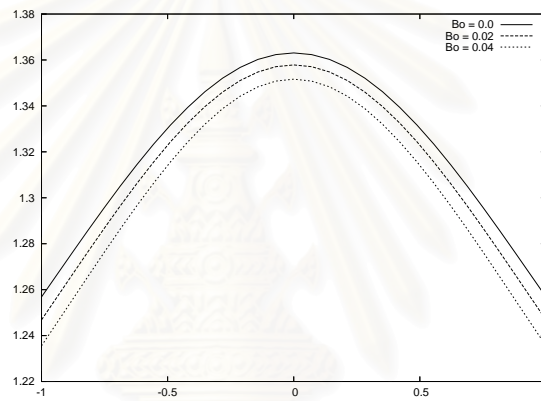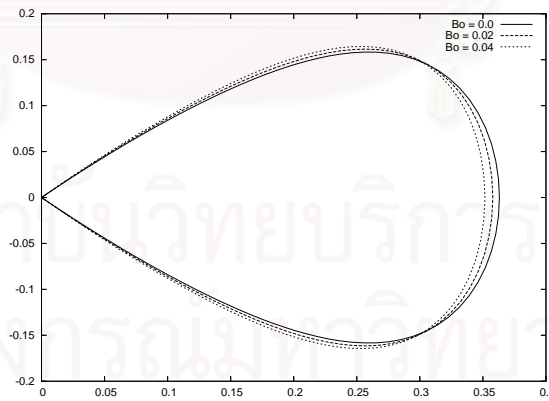onlinear phase trajectories. (c) Fully nonlinear profiles of SUB2 for $hob2 = -0.30, F = 0.40$ and $Bo = 0.05, 0.10, 0.15$ and 0.19. (d) Plots of $y - 1$ versus $\frac{dy}{dx} = \tan\theta$ of the fully nonlinear phase trajectories.

(a) $Bo = 0$

(b) $Bo = 0.10$

(c) $Bo = 0.20$

(d) $Bo = 0.50$
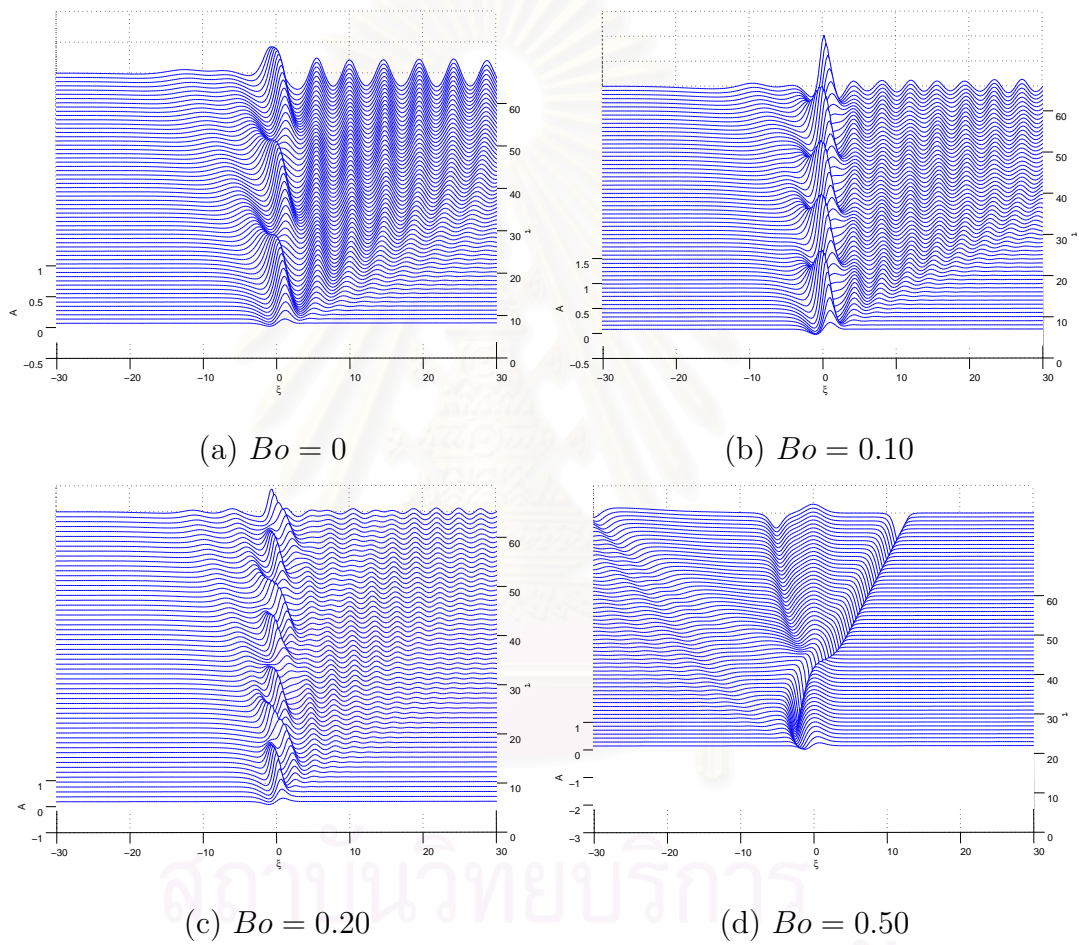
Figure 4.22: Time evolution of the gravity-capillary subcritical solutions for $hob2 = -0.40$ and $F = 0.60$.

<div align="center">(a)   (b)</div>
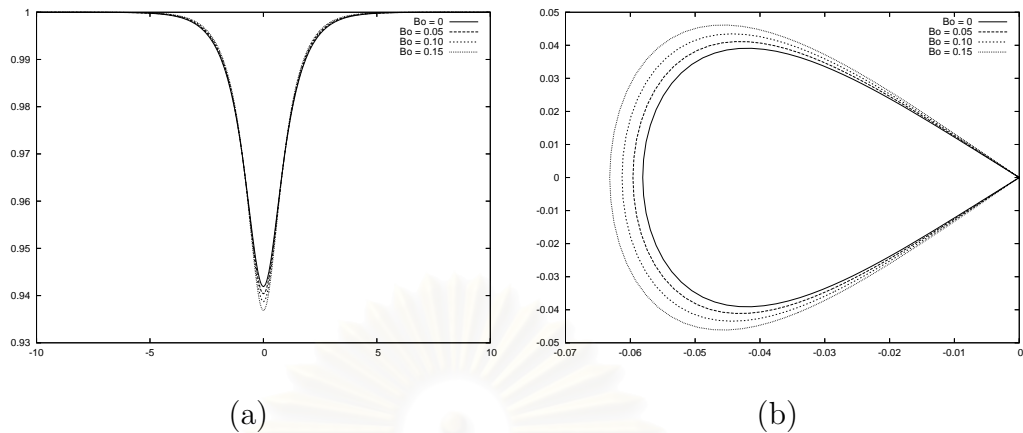
Figure 4.23: Typical free-surface profiles of gravity-capillary supercritical flows over a dip. (a) Fully nonlinear profiles for $F = 1.50$ and $hob2 = -0.40$. (b) Plots of $y - 1$ versus $\frac{dy}{dx} = \tan\theta$ of the fully nonlinear phase trajectories.

4.3   Conclusions

In this chapter, two-dimensional flows of an ideal fluid over a single obstacle are considered. The fluid is subjected to the combined effects of gravity and surface tension. Fully nonlinear solutions and weakly nonlinear solutions are compared for a single bump ($hob2 > 0$) or dip ($hob2 < 0$). Classical and previous solutions are completely recovered, and new solutions are proposed.

For free-surface flows over a bump, there are total of five solution types. First type SUB1 is the subcritical flow which is characterized by a train of nonlinear waves behind the obstacle. Second type SUB2 is the wave-free subcritical flow or drag-free solution which is a new proposed family of solution. Third type SUP1 is the supercritical flow perturbed from a uniform stream. SUP2 solution is another representation of the supercritical flow perturbed from a solitary wave and constitutes the fourth type. It should be noted that both SUP1 and SUP2 profiles are quite similar except the wave amplitude over an obstacle. Last type of solutions is the critical flow which is characterized by a hydraulic fall. The first four
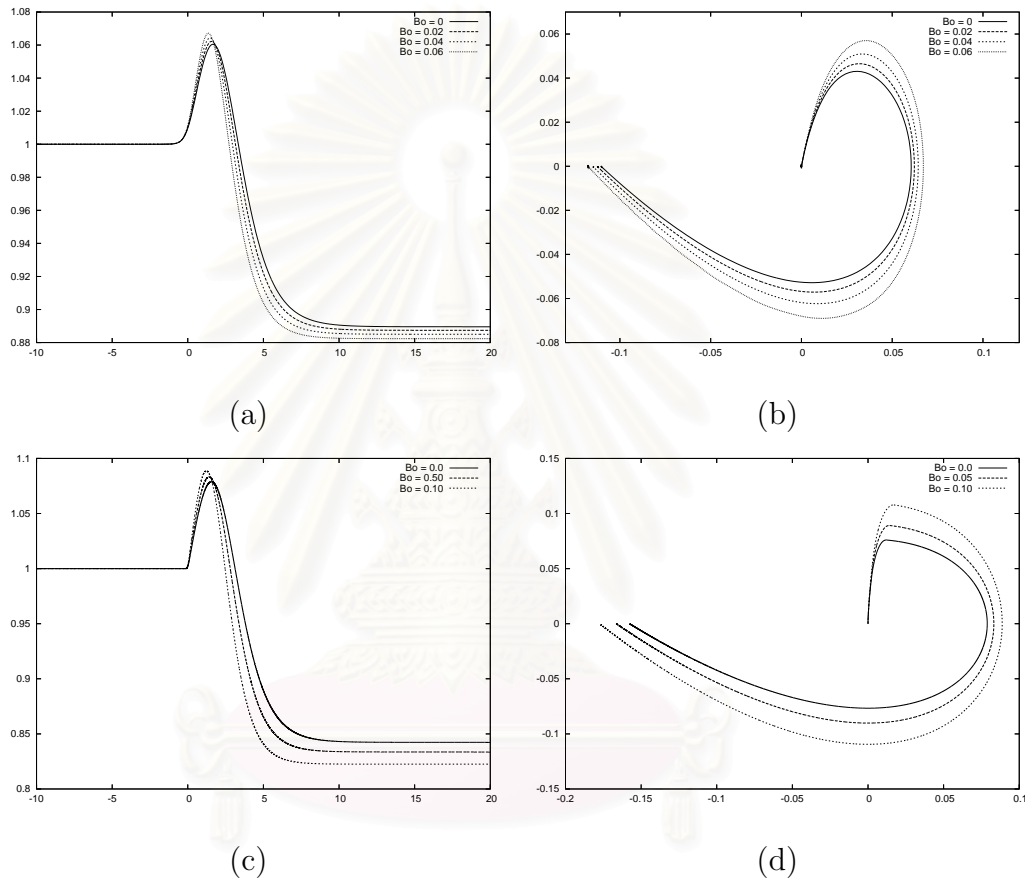
Figure 4.24: Typical free-surface profiles of gravity-capillary critical flow over a dip. (a) Fully nonlinear profiles for $hob2 = -0.20$ and $Bo = 0, 0.02, 0.04$ and 0.06. (b) Plots of $y - 1$ versus $\frac{dy}{dx} = \tan\theta$ of the fully nonlinear phase trajectories. (c) Weakly nonlinear profiles for $hob2 = -0.16$ and $Bo = 0, 0.05,$ and 0.10. (d) Weakly nonlinear phase portraits.
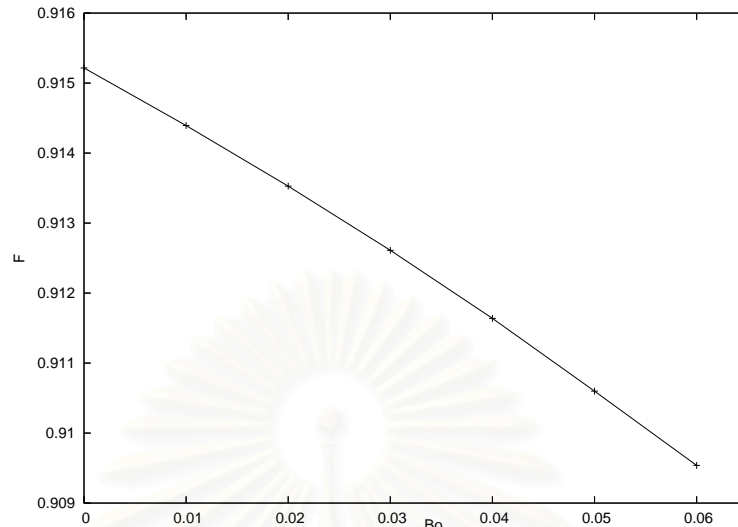
Figure 4.25: Relationship between the Froude number F and the Bond number Bo of critical free-surface flows over a dip for $hob2 = -0.20$.

types are two-parameter family of solutions that depend on the Froude number F and the height of obstacle $hob2$. The hydraulic fall solution is a one-parameter family of solution for which the Froude number F is part of the solution. In addition, if the upstream radiation condition is removed, Dias and Vanden-Broeck [16] found another solution called "generalized hydraulic fall". This solution is characterized by a downstream supercritical flow and a train of nonlinear waves on the upstream side. All solutions except the generalized hydraulic fall are presented in the solution diagram in the $(F, hob2)$-plane.

For free-surface flows over a dip, the computed solutions can be categorized into four different types. First type SUB1 is the subcritical flow characterized by a train of nonlinear waves behind the obstacle with the uplifted free surface in the dip region. Second type SUB2 is the subcritical flow characterized by an elevation wave. Third type is the supercritical flow with a depression wave perturbed from a uniform stream. Last type is the critical flow for which the free surface is elevated in the region of dip followed by a hydraulic fall. The first three types of these

solution are the two-parameter family of solution similar to the case of flow over a bump. The fourth type is a one-parameter family of solution depending on the obstacle height $hob2$. Regions of existence of these numerical solutions in the presence of a dip are summarized in the solution diagram.

While the inclusion of surface tension has direct influence on the wavelength and the wave amplitude in the subcritical flow regime, but it is rather ambiguous in the case of supercritical flow regime. In the critical flow regime over a bump, the upstream free-surface profile changes from the rigid lid to the shape of half wave packet as the obstacle height decreases to its critical value hob^*. When $hob2 < hob^*$, no critical solution can be found. For critical flow over a dip, the maximum free surface elevation right above the dip is an increasing function of the Bond number.

CHAPTER V

FREE-SURFACE FLOWS OVER TWO OBSTACLES

Free-surface flows over two obstacles are considered in this chapter. The isosceles triangular obstacles with acute angles $\theta_1^{up} = \theta_2^{up} = \frac{\pi}{4}$ are chosen. For gravity flows without surface tension, two new solutions of the fully nonlinear problem are proposed in §5.1. In §5.2, free-surface flows in critical regime under gravity and surface tension over two obstacles are considered. There exist two new solution types of this critical flow.

5.1   Flow without Surface Tension ($Bo = 0$)

In this section, we consider free-surface flows without surface tension over two obstacles. Far upstream as $x \to -\infty$, the flow is uniform. There is, in general, a five-parameter family of solutions for flows over two obstacles. These parameters can be chosen as the Froude number F, the Bond number Bo, the obstacle heights hob_1, hob_2 and the distance between the two obstacles x_d. In this thesis, we let the distance between the obstacles be given as a constant in the complex potential f-plane, i.e., $|\phi_{J_2} - \phi_{J_1}| = 20$.

In 1984, Pratt [54] investigated this problem experimentally and partially solved the weakly nonlinear problem. He proposed three stationary critical flow solutions from his experimental results: (1) SUB_HF: Subcritical flow over the leftmost obstacle with a train of nonlinear wave on downstream side trapped between the obstacles and a hydraulic fall over the rightmost obstacle (see Figure

5.1(a)), (2) DF_HF: Depression wave or drag-free over the leftmost obstacle with a hydraulic fall over the rightmost obstacle (see Figure 5.1(b)) and (3) HF_SUP: Hydraulic fall over the leftmost obstacle followed by an elevated profile of supercritical flow over the rightmost obstacle (see Figure 5.1(c)). In his weakly nonlinear calculation, only the SUB_HF solution could be found. It should be noted that the DF_SUP solution does not exist in case of flow without surface tension. In particular, the DF_SUP is the result of using SUB_HF as initial data with the inclusion of surface tension. Further discussion shall be presented in §5.2.

Belward [3] computed fully nonlinear solutions of HF_SUP type. For this solution, free-surface profile at the rightmost obstacle was similar to the solution which was the perturbation of a uniform stream in case of supercritical flow over a single obstacle. This flow configuration had been found experimentally by Pratt [54]. However, Belward's results was inaccurate due to nonphysical waves of small amplitude on the upstream side of the leftmost obstacle. Dias and Vanden-Broeck [19] constructed a "hybrid" flow over two submerged obstacles which can be viewed as the superposition of two basic flows over a single obstacle. They computed numerically fully nonlinear solutions of the subcritical flow over the leftmost obstacle with a train of nonlinear waves on downstream and a hydraulic fall over the rightmost obstacle. This solution is of SUB_HF type. They used this result to describe the behavior of *generalized hydraulic fall* over a single obstacle when the distance between the obstacles was large.

In 2005, Binder, Vanden-Broeck and Dias [9] calculated four types of solutions in subcritical and supercritical flow regimes. Two of these were subcritical flows. (1) SUB_SUB: There were two sets of nonlinear waves with different amplitudes on the free-surface. One was trapped between the two obstacles with larger amplitude than the other that was on downstream of the rightmost obstacle. Typ-

ical profile is shown in Figure 5.2(a). (2) SUB_SYM: The profile was symmetrical with trapped waves between two obstacles of equal height (see Figure 5.2(b)). The remaining two types were supercritical flows. (3) SUP_SUP: An elevation wave over each obstacle characterizes this solution. The fully nonlinear profile is shown in Figure 5.2(c). (4) SUP_TRAP: The flow was supercritical with waves trapped between two obstacles as shown in Figure 5.2(d).

Here we present another solution of SUB_SUB type, that is the amplitude of trapped wave between two obstacles is smaller than those on downstream of the rightmost obstacle for the same values $hob1 = hob2 = 0.10$ as the profile in Figure 5.2(a) with different Froude number F. Typical profile of this solution type is shown in Figure 5.3. If the distance between the obstacles of SUB_HF is sufficiently small, the trapped waves between two obstacles can not be visually seen since the wavelength would be larger than the distance between the obstacles (see Figure 5.4). Our remark to the new type of critical flow of Binder, Vanden-Broeck and Dias [9] as shown in Figure 5.4 (f) is that their solution is actually not the new type. Furthermore, the number of waves trapped between obstacles decreases as the distance between the obstacles decreases. When this distance is small, the free-surface profile over the leftmost obstacle looks like a hydraulic fall and no waves trapped between two obstacles (see Figure 5.4(e)). In this thesis, we have recovered all results of Belward [3]: HF_SUP, Dias and Vanden-Broeck [19] : SUB_HF and Binder, Vanden-Broeck and Dias [9]: SUB_SUB, SUB_SYM, SUP_SUP and SUP_TRAP.

In the followings, we shall present the two new types of solutions of free-surface flows over two obstacles.

1. Depression Waves over the Obstacles (DF_DF)

This subcritical flow solution can be described as depression waves that occur right above the leftmost and the rightmost obstacles. Typical free-surface profile for $hob1 = 0.05, hob2 = 0.10, F = 0.20$ and $x_d = 19.9762$ is shown in Figure 5.5(a). Phase trajectory of the fully nonlinear solution in Figure 5.5(b) can be described as follows. The solution starts at the fixed point $y - 1 = 0$ with a first downward jump onto an inner periodic orbit O_1 (small orbit). After moving clockwise half a circle on O_1, there is a second downward jump back to the same fixed point. Next we have a third downward jump onto an outer periodic orbit O_2 (large orbit) and move clockwise half a circle on this orbit. Finally, there is a fourth downward jump returning to the same fixed point $y - 1 = 0$ again. Since the weakly nonlinear solution can not yet be found, we are unable to compare qualitatively with the corresponding fully nonlinear phase trajectory.

It should be noted that amplitude of the depression waves increases as a function of the height of obstacle (see Figure 5.6). Figure 5.7 shows typical profiles of subcritical flow over two obstacles for various values of the Froude number F. It should be noted that, as F decreases, amplitude of the waves trapped between two obstacles and on downstream of the rightmost obstacle decreases and ultimately vanishes showing similar behavior as in the case of depression waves over a single obstacle.

2. Hydraulic Fall over the Leftmost Obstacle with Supercritical Flow over the Rightmost Obstacle (HF_SUP)

This solution is in the critical flow regime for which hydraulic fall occurs at the leftmost obstacle and $F > 1$ over the rightmost obstacle. There are two types of solution, i.e., (1) HF_SUP_U: The flow is perturbed from a uniform stream and (2)

HF_SUP_S: The flow is perturbed from a solitary wave. Typical fully nonlinear free-surface profiles of HF_SUP_U and HF_SUP_S, for $hob1 = hob2 = 0.10$ and $F = 0.9005$ are shown in Figure 5.8(a). The HF_SUP_U solution was found earlier in Pratt's experiments [54] and by Belward [3] in his computation of fully nonlinear problem. *The HF_SUP_S solution is a new type of solution.* Fully nonlinear trajectories of HF_SUP_U and HF_SUP_S in Figure 5.8(a) are shown in Figure 5.8(b). The trajectory starts at the fixed point $y - 1 = 0$ with a downward jump onto the solitary wave orbit. It then moves clockwise one cycle on this orbit and goes directly to another fixed point $y - 1 = \frac{2}{3}(F^2 - 1)$. It is obvious that the solitary wave orbit of HF_SUP_U is smaller than that of HF_SUP_S.

Computation procedure for the fully nonlinear results of HF_SUP_U consists of two steps.

Step 1 : Use initial data

$$\theta_{\text{initial}} = -0.001 \times \text{sech}^2(\phi - \phi_{hob1})$$

to calculate solution with a hydraulic fall over the leftmost obstacle $(hob1 \neq 0, hob2 = 0)$.

Step 2 : Use solution from step 1 as initial guess to find HF_SUP_U solution for $hob2 \neq 0$.

Here ϕ_{hob1} is the value of ϕ at the apex of the leftmost obstacle.

To obtain the solution of HF_SUP_S type, we need only the first step of the above procedure and set $hob1 = hob2$ in the calculation.

This type of solutions depends only on two parameter $hob1$ and $hob2$. Typical profiles for HF_SUP_U and HF_SUP_S are shown in Figure 5.9(a) and (c), respectively, for various values of the height of the rightmost obstacle $hob2$. As

*hob*2 increases, the maximum free-surface elevation over the rightmost obstacle increases for HF_SUP_U and decreases for HF_SUP_S and ultimately reaches the elevation of the far upstream free surface $y = 1$. Figure 5.9(b) and (d) show the corresponding phase trajectories of Figure 5.9(a) and (c), respectively. As *hob*1 increases, profile between two obstacles decreases and approach same level as $x \to \infty$. In addition, amplitude of the elevation wave over the rightmost obstacle is a decreasing function of *hob*1 for HF_SUP_U; but it is an increasing function of *hob*1 for HF_SUP_S as shown in Figure 5.10. Clearly, these solution behaviors can be seen in the phase trajectories.

In this case, the Froude number F is treated as part of the solution and depends only on the height of the leftmost obstacle *hob*1. Relationship between the Froude number F and the height of the leftmost obstacle *hob*1 is shown in Figure 5.11. Figure 5.12 shows that, for a given *hob*1, the Froude number F is independent of the height of the rightmost obstacle .

Finally, Figure 5.13 summarizes the relationship between the height of the rightmost obstacle *hob*2 and the amplitude $|A|$ of elevation wave over the right-most obstacle, for $hob1 = 0.05, 0.10$ and 0.20. Numerical results show that $|A|$ is an increasing function of *hob*2 for HF_SUP_U solution type but is a decreasing function of *hob*2 for HF_SUP_S. Comparison with the previous results of Dias and Vanden-Broeck [17] indicates that, in the neighborhood of the rightmost obstacle, the free-surface prefile behaves in the exact same way as that of flow over a single obstacle. This comparison provides an alternative check on our results.

Table 5.1 summarizes all solution types of free-surface flows over two obstacles without surface tension. There are 8 types with 9 free-surface profiles. We can completely recover all solution types that obtained by Pratt [54], Belward [3], Dias and Vanden-Broeck [19] and Binder, Vanden-Broeck and Dias [9].
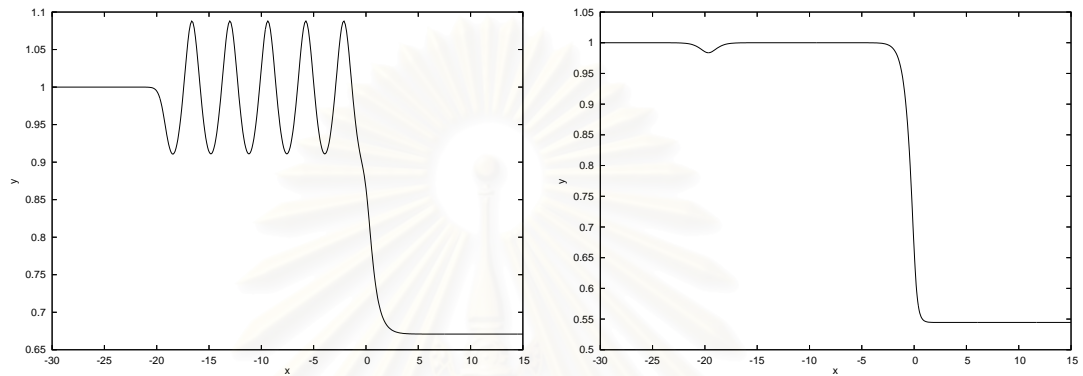
(a) SUB_HF

(b) DF_HF
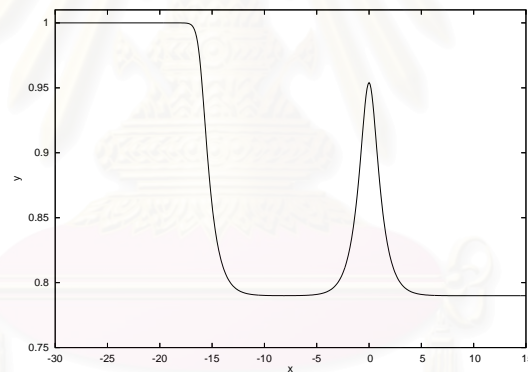
(c) HF_SUP

Figure 5.1: (a) SUB_HF: Subcritical flow over the leftmost obstacle with a train of nonlinear waves and a hydraulic fall over the rightmost obstacle. (b) DF_HF: Drag-free profile over the leftmost obstacle and a hydraulic fall over the rightmost obstacle. (c) HF_SUP: Critical flow with a hydraulic fall over the leftmost obstacle and an elevation wave over the rightmost obstacle.

(a) SUB_SUB

(b) SUB_SYM

(c) SUP_SUP

(d) SUP_TRAP
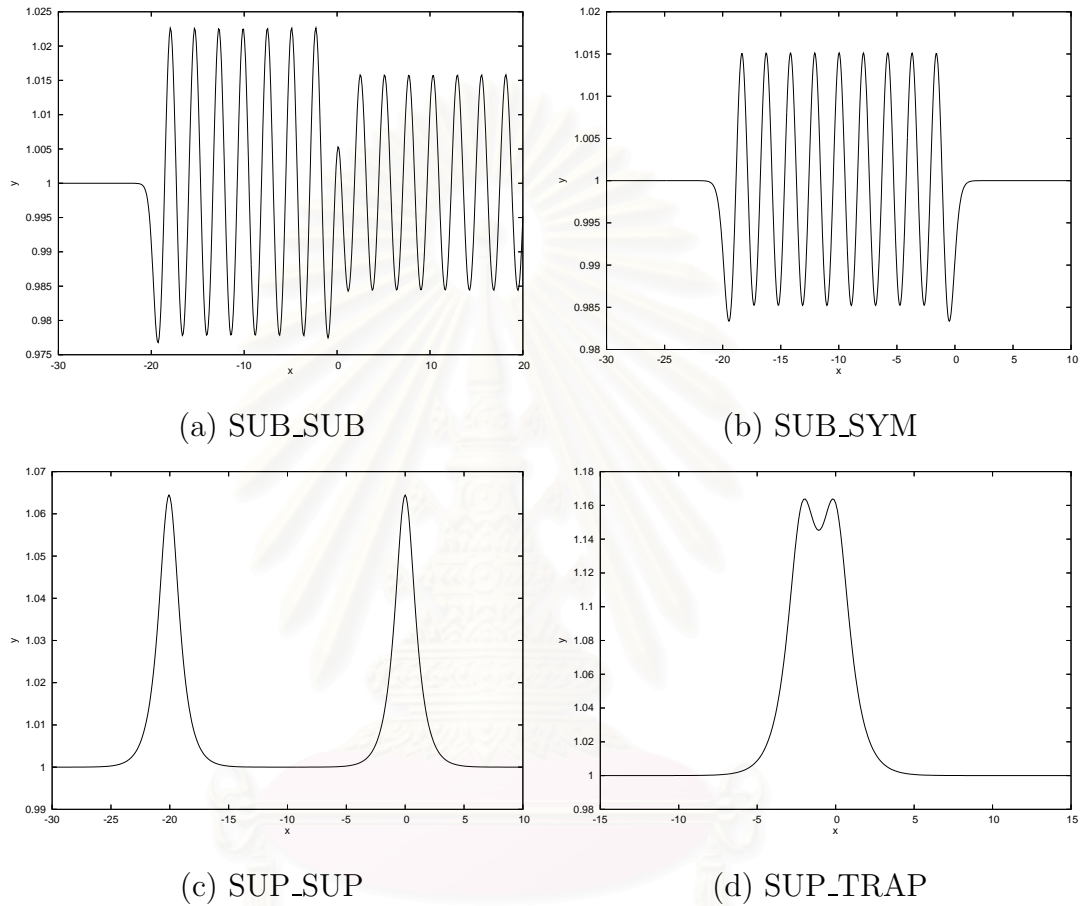
Figure 5.2: (a) SUB_SUB: Nonsymmetric subcritical solution with two sets of nonlinear waves of different amplitudes for $F = 0.640, hob1 = hob2 = 0.10$ and $x_d = 19.9206$. (b) SUB_SYM: Symmetric subcritical solution with waves trapped between the obstacles for $F = 0.5763, hob1 = hob2 = 0.10$ and $x_d = 19.9440$. (c) SUP_SUP: Symmetric supercritical solution with elevation waves for $F = 1.50, hob1 = hob2 = 0.20$ and $x_d = 20.0471$. (d) SUP_TRAP: Supercritical solution with a train of waves trapped between the obstacles for $F = 1.50, hob1 = hob2 = 0.30$ and $x_d = 2.1163$.
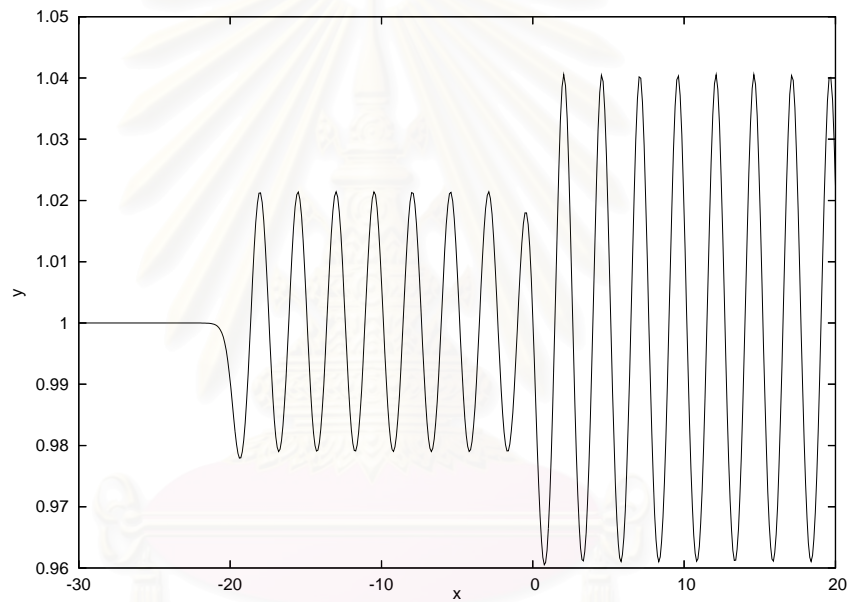
Figure 5.3: SUB_SUB: Nonsymmetric subcritical solution for $F = 0.630, hob1 = 0.10, hob2 = 0.10$ and $x_d = 19.9206$. Amplitude of waves trapped between the obstacles is smaller than that of the downstream waves.

(a) $x_d = 19.6384$

(b) $x_d = 9.9392$

(c) $x_d = 9.3831$

(d) $x_d = 6.7660$

(e) $x_d = 4.8550$

(f)
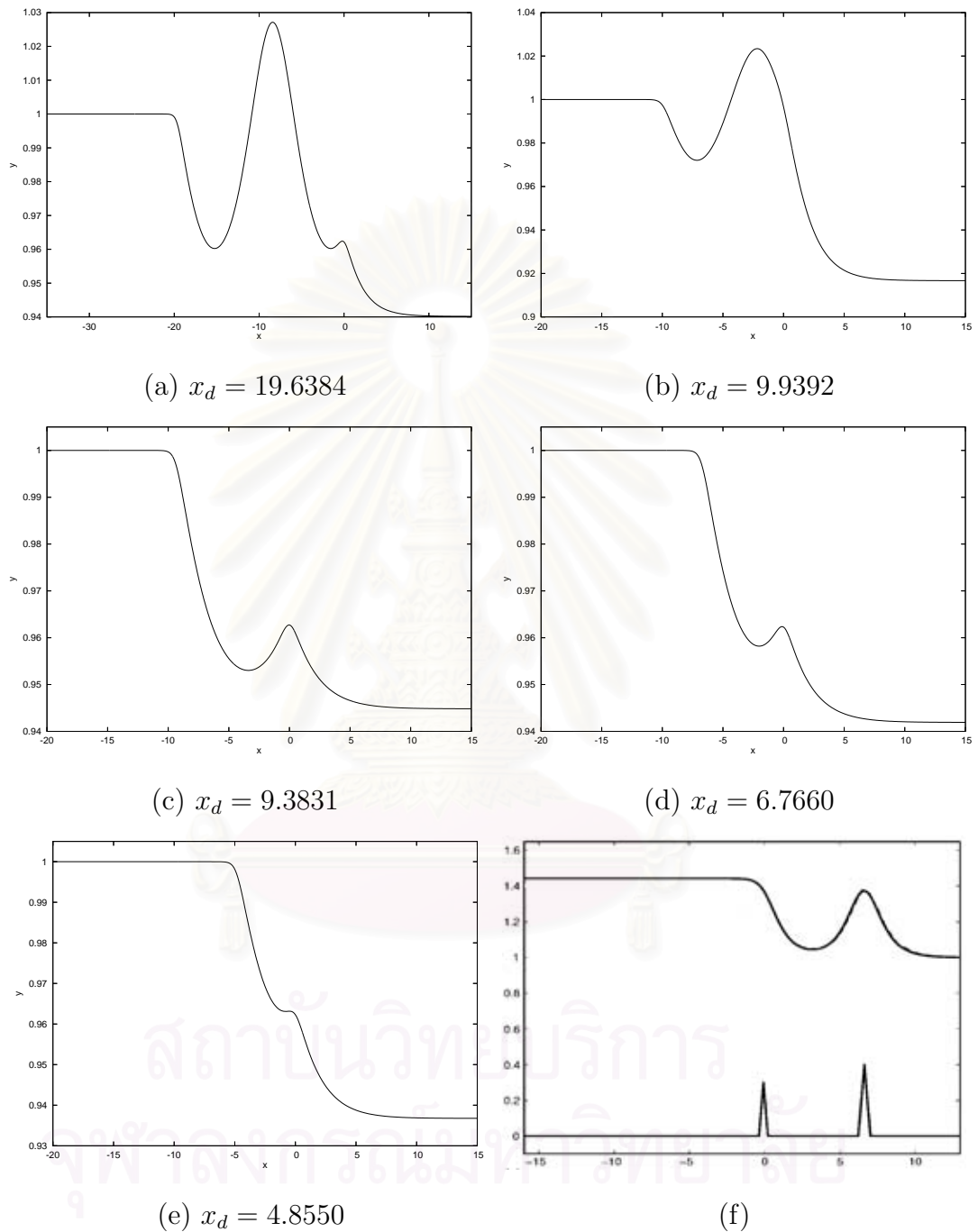
Figure 5.4: Free-surface profiles of critical flow SUB_HF solution for various values of the distance between the obstacles. (a)-(e) $hob1 = hob2 = 0.05$ and $x_d = 19.6384, 9.9392, 9.3831, 6.7660$ and 4.8550, respectively. (f) Solution proposed by Binder, Vanden-Broeck and Dias [9].
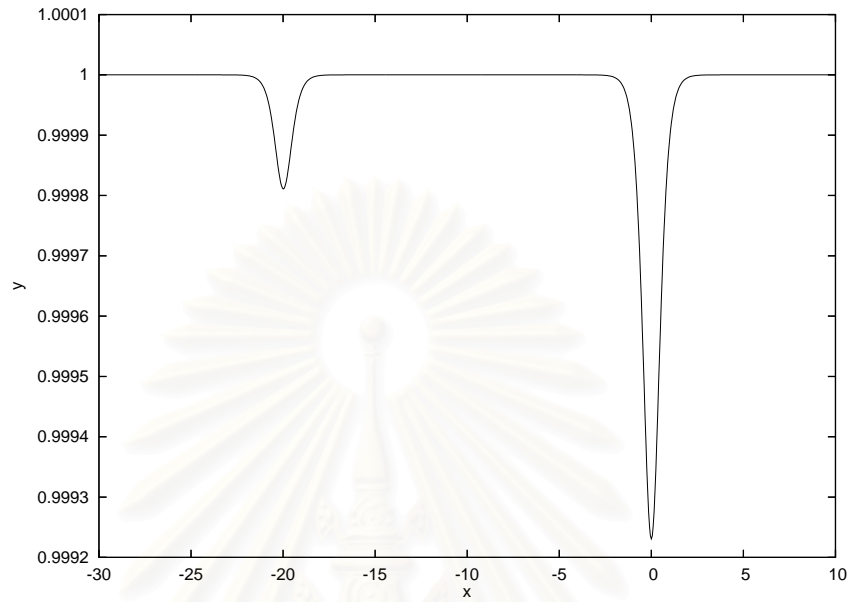
(a)
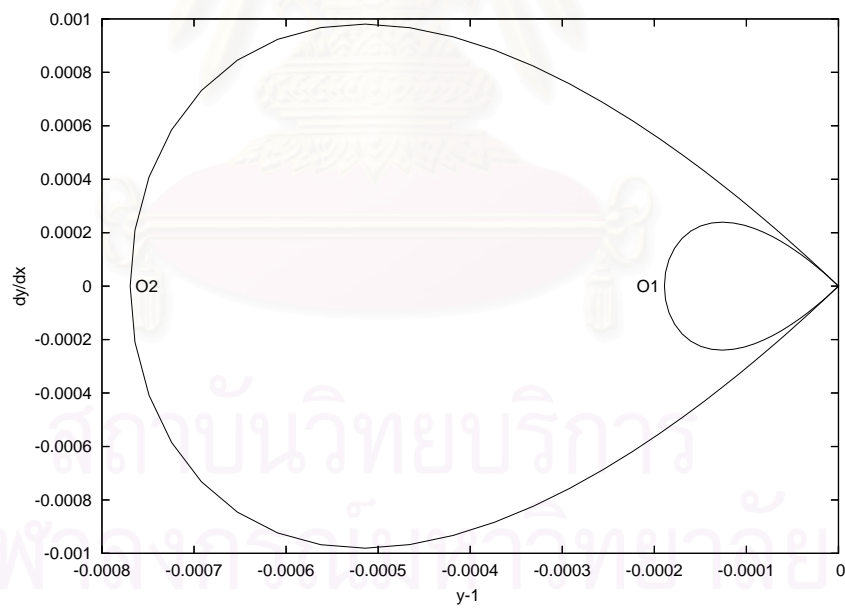
(b)

Figure 5.5: Typical free-surface profile of depression waves or drag-free subcritical solution over each obstacles (DF_DF) for $hob1 = 0.05, hob2 = 0.10, F = 0.20$ and $x_d = 19.9762$. (a) Fully nonlinear profile. (b) Phase trajectory.
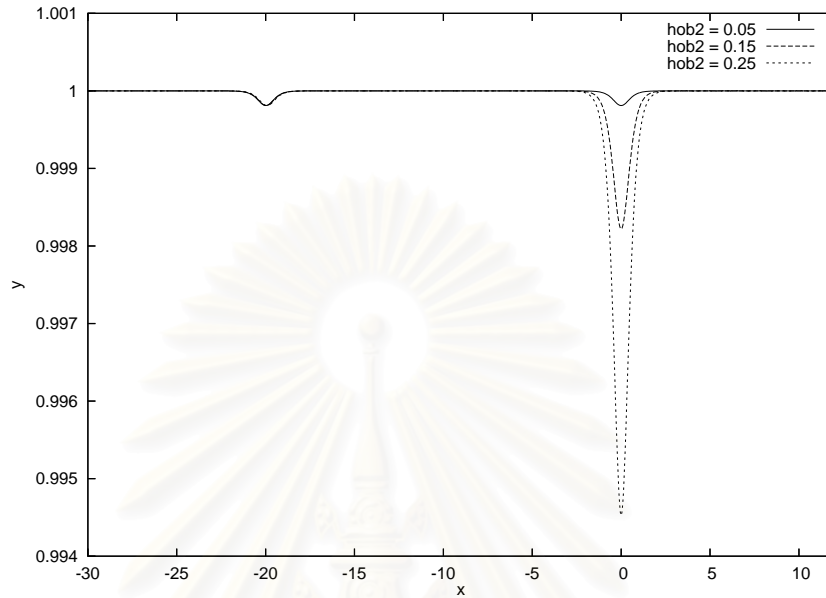
(a)
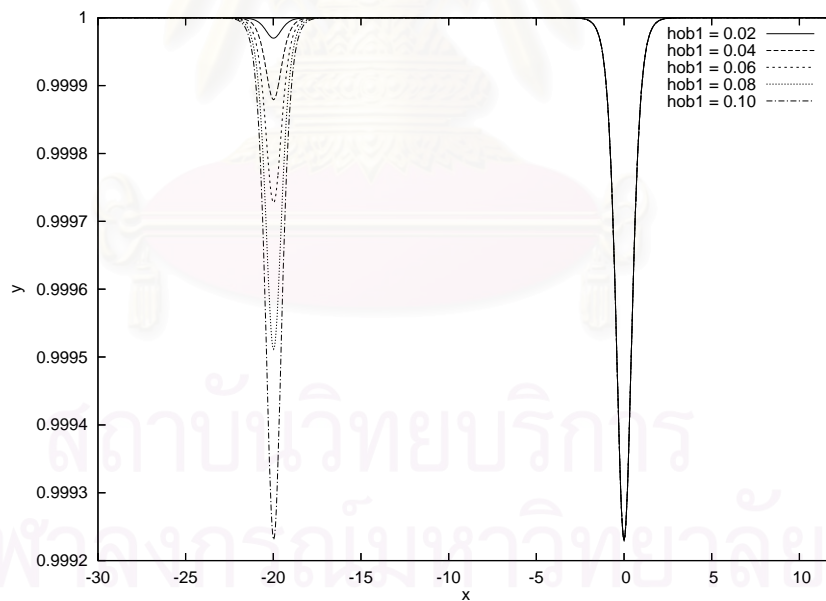
(b)

Figure 5.6: Effect of obstacle heights on the DF_DF solution. (a) Fully nonlinear free-surface profiles for $F = 0.20, hob1 = 0.05$ and various values of $hob2$. (b) Fully nonlinear free-surface profiles for $F = 0.20, hob2 = 0.10$ and various values of $hob1$.

(a) $F = 0.25$ (b) $F = 0.35$

(c) $F = 0.45$ (d) $F = 0.55$
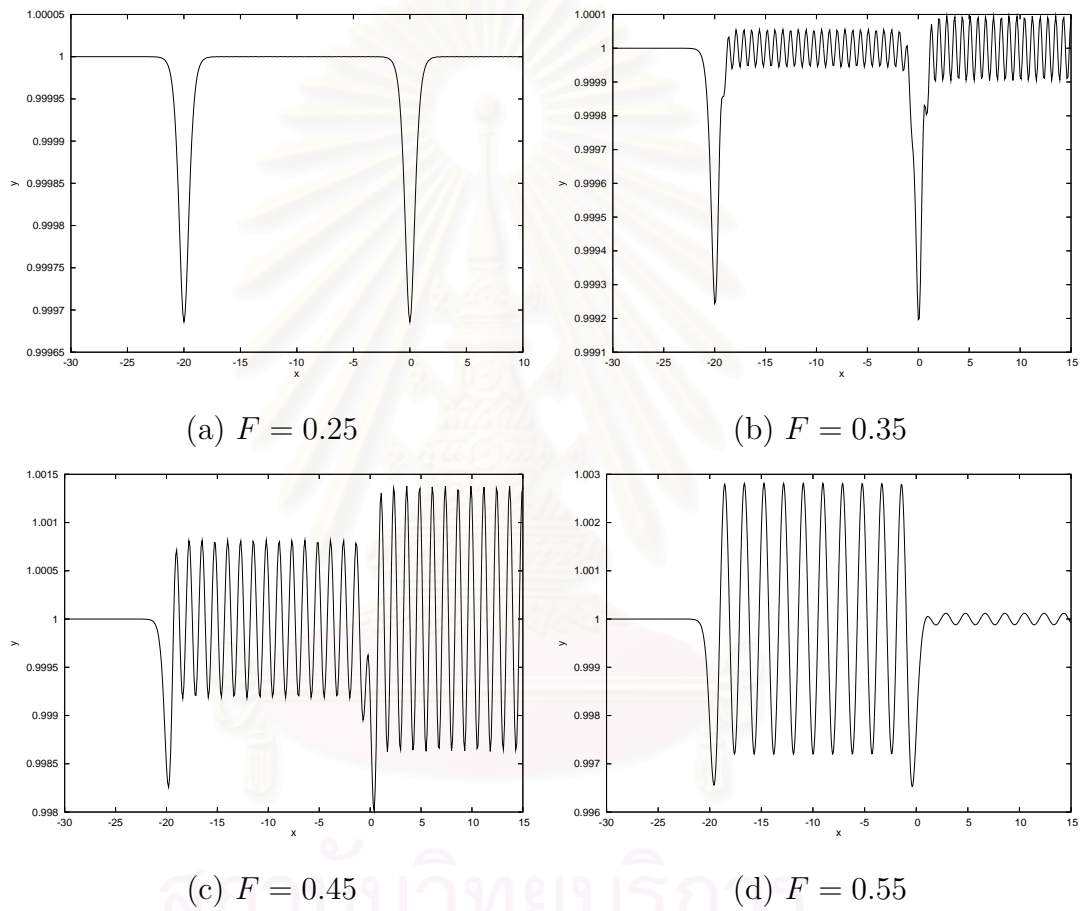
Figure 5.7: Effect of Froude number F on the SUB_SUB solution for $hob1 = hob2 = 0.05$. As F decreases, the SUB_SUB solution profile eventually changes to the DF_DF profile in (a).
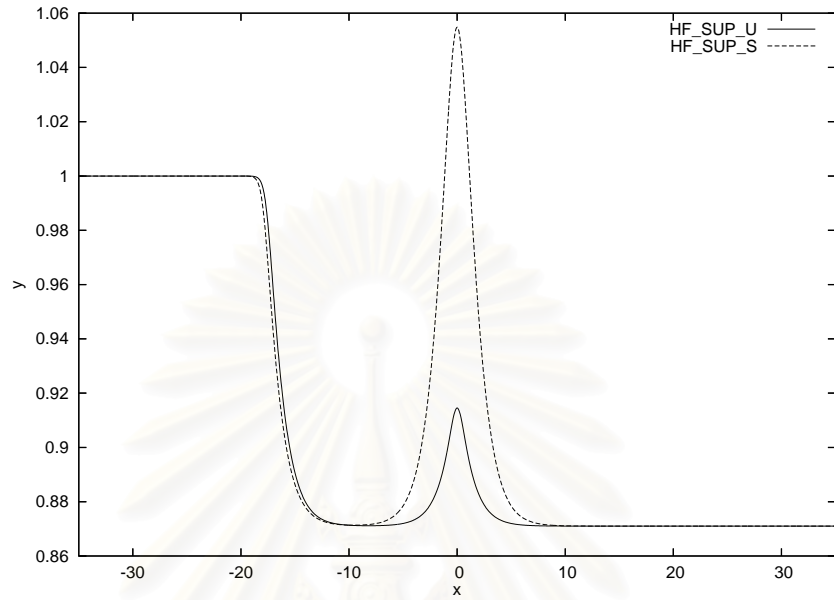
(a)
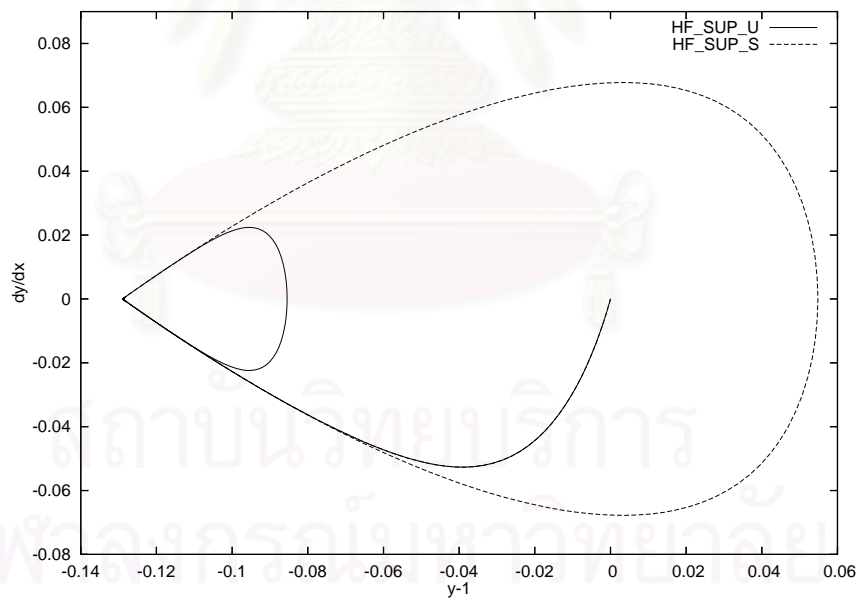
(b)

Figure 5.8: Typical free-surface profiles of HF_SUP_U and HF_SUP_S solutions for $hob1 = hob2 = 0.10$ and $F = 0.9005$. (a) Fully nonlinear profiles. (b) Plots of $y - 1$ versus $\frac{dy}{dx}$ of the fully nonlinear phase trajectory.
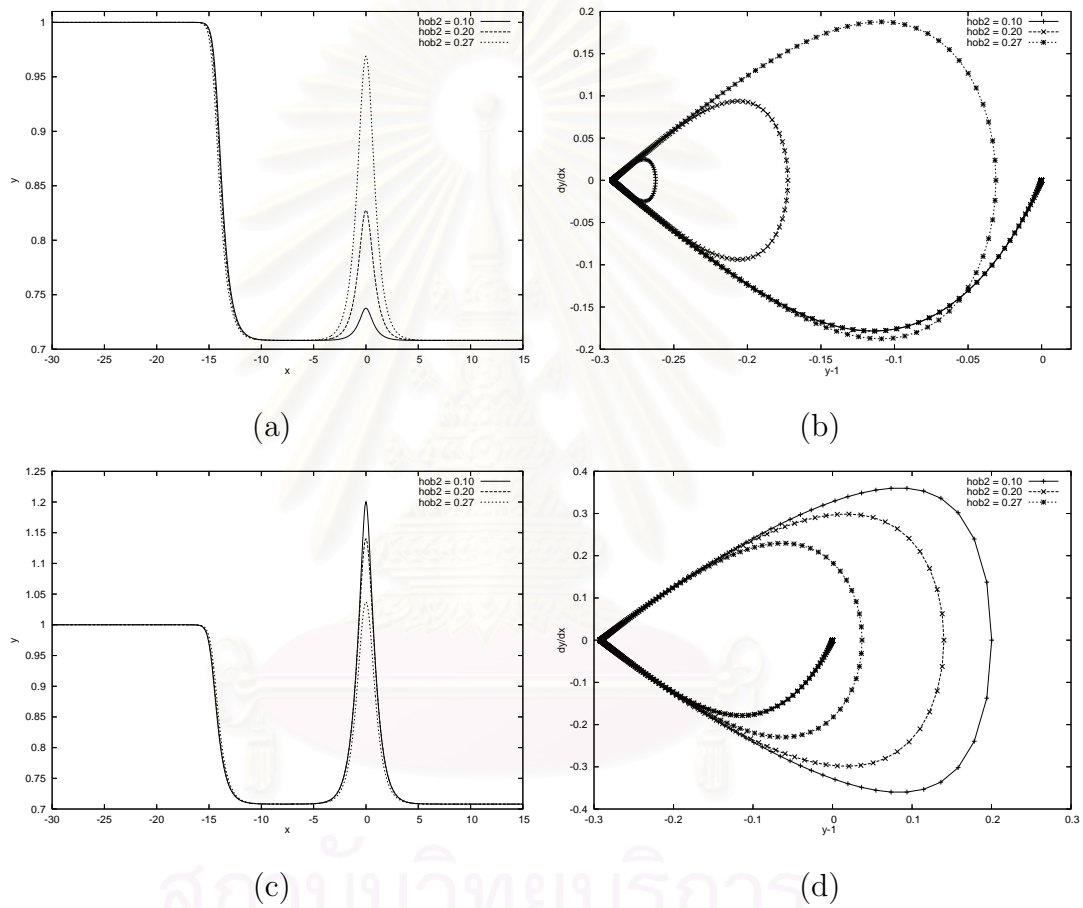
Figure 5.9: Effect of the rightmost obstacle height $hob2$ on HF_SUP_U and HF_SUP_S solutions when $hob1 = 0.20$. (a) Fully nonlinear profiles of HF_SUP_U. (b) Phase trajectories. (c) Fully nonlinear profiles of HF_SUP_S. (d) Phase trajectories.

(a)

(b)

(c)

(d)
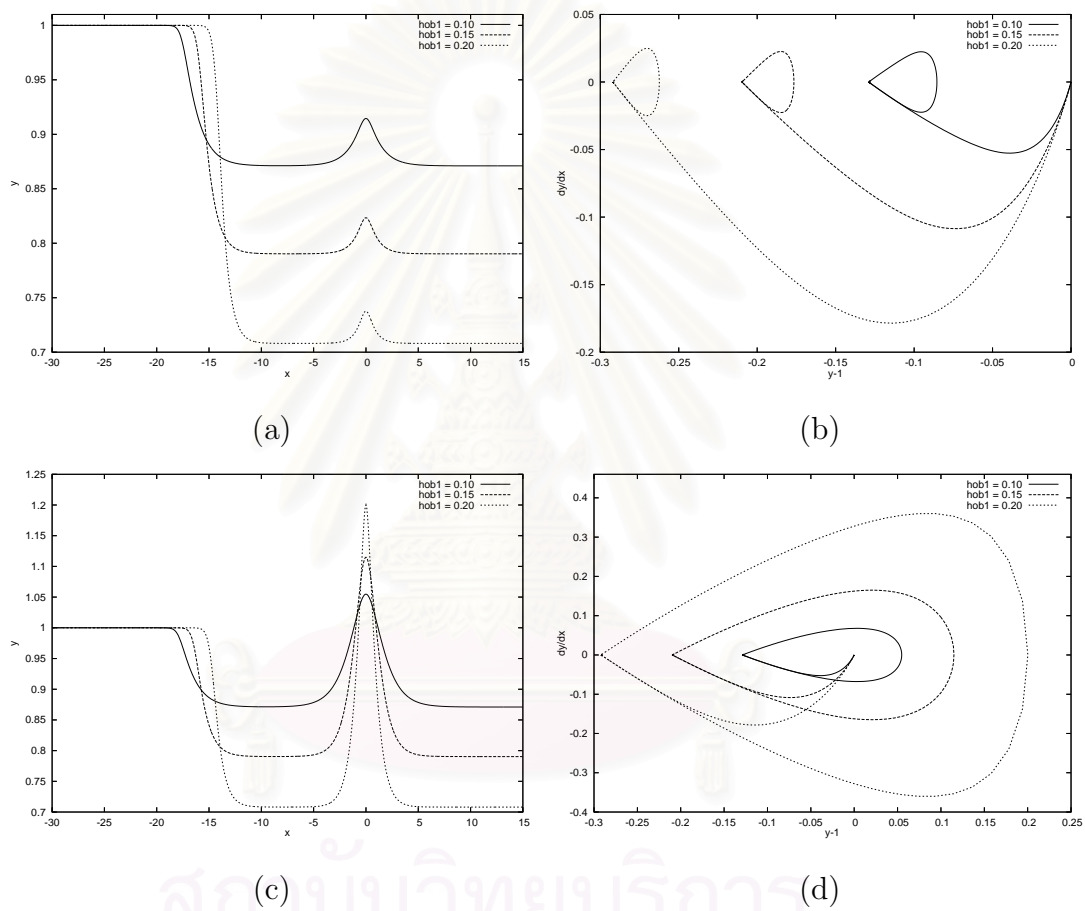
Figure 5.10: Effect of the leftmost obstacle height $hob1$ on HF_SUP_U and HF_SUP_S solutions when $hob2 = 0.10$. (a) Fully nonlinear profiles of HF_SUP_U. (b) Phase trajectories. (c) Fully nonlinear profiles of HF_SUP_S. (d) Phase trajectories.
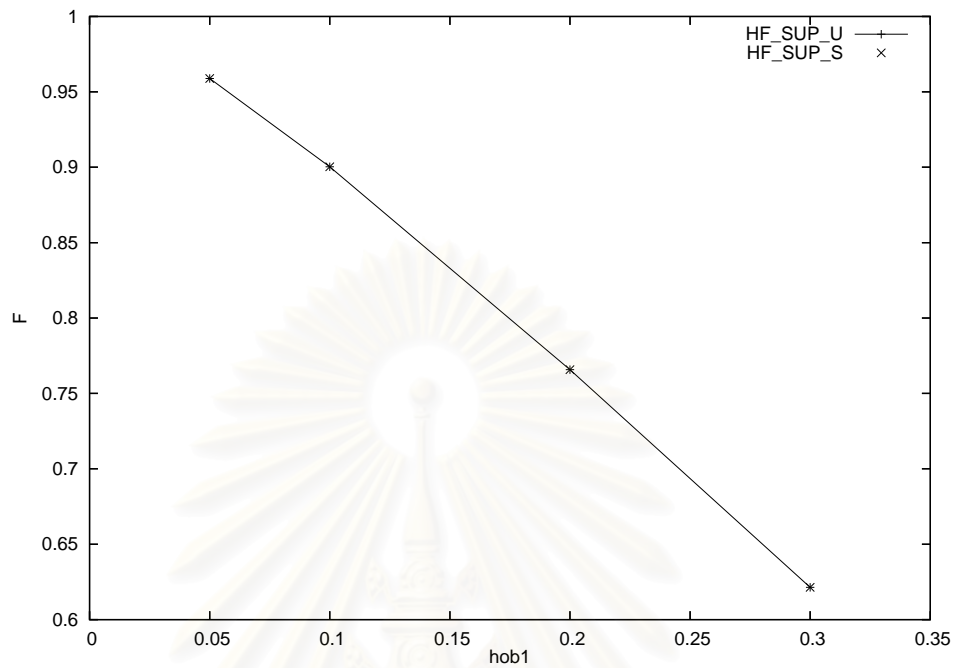
Figure 5.11: Relationship between the height $hob1$ and the Froude number F of HF_SUP_U and HF_SUP_S.
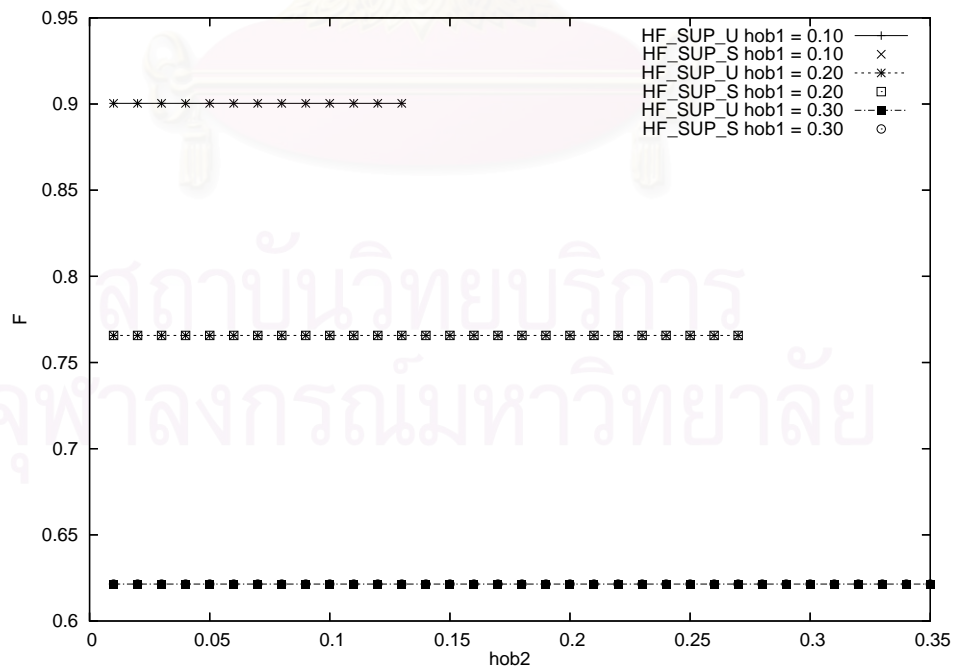
Figure 5.12: Relationship between the height $hob2$ and the Froude number F of of HF_SUP_U and HF_SUP_S for $hob1 = 0.10, 0.20$ and 0.30.
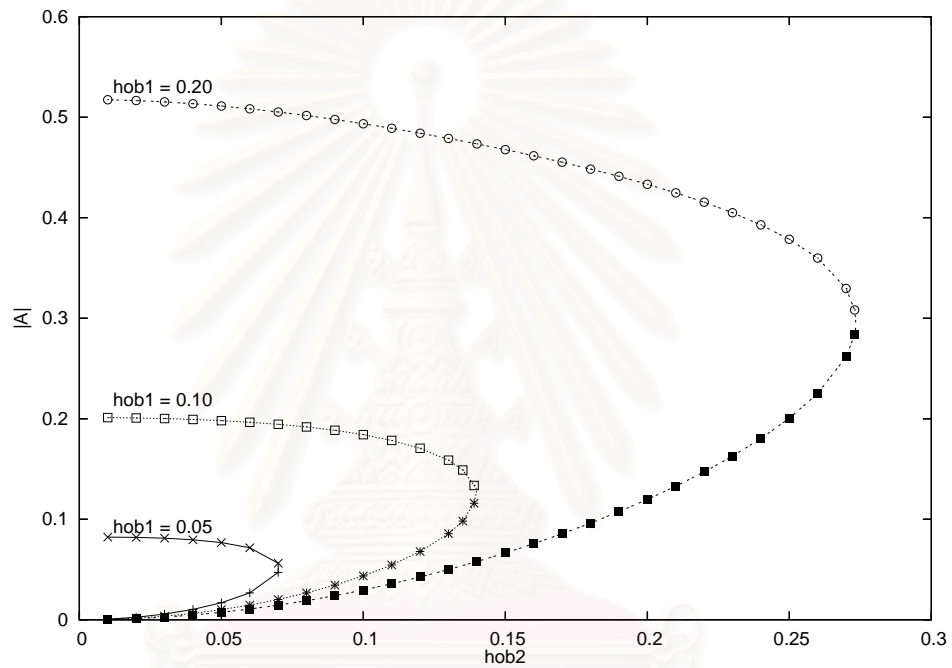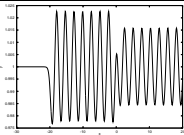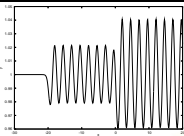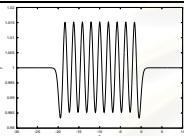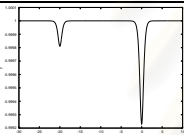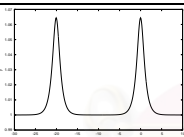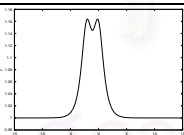
Figure 5.13: Relationship between $hob2$ and $|A|$ for $hob1 = 0.05, 0.10$ and 0.20. Here $|A|$ is the amplitude of elevation wave determined by the distance of maximum level of elevation wave from the far downstream level. The solid line with plus, the dotted line with asterisk, and the dashed with black squared on the lower branch of each curve are solutions of HF_SUP_U. The solid line with cross, the dotted line with square, and the dashed with circle on the upper branch are solutions of HF_SUP_S.

Solution type	P[54]	B[3]	DV[19]	BVD[9]	Present work
1.a SUB_SUB_1				√	√
1.b SUB_SUB_2					√
2 SUB_SYM				√	√
3 DF_DF					√*
4 SUP_SUP				√	√
5 SUP_TRAP				√	√

Continued . . .

Table 5.1: Solution types of free-surface flows over two obstacles without surface tension. The symbol $\sqrt{}$ denotes the existing solutions and $\sqrt{}^*$ denotes a new family of numerical solution. P[54]: Experimental results of Pratt [54], B[3]: Numerical results of Belward [3], DV[19]: Numerical results of Dias and Vanden-Broeck [19], and BVD[9]: Numerical results of Binder, Vanden-Broeck and Dias [9].
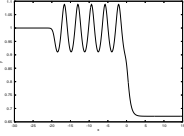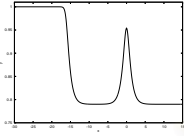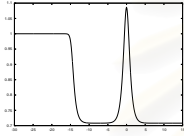
Solution type	P[54]	B[3]	DV[19]	BVD[9]	Present work
 6 SUB_HF	$\checkmark$		$\checkmark$	$\checkmark$	$\checkmark$
 7 HF_SUP_U	$\checkmark$	$\checkmark$			$\checkmark$
 8 HF_SUP_S					$\checkmark^*$

Table 5.1: (continued)

5.2 Flow under Gravity and Surface Tension ($Bo > 0$)

In this section, critical free-surface flows over the two obstacles under gravity and surface tension are considered. We seek solutions that are essentially characterized by a hydraulic fall at either one of these obstacles. In the absence of surface tension, there are three solution types, namely SUB_HF, HF_SUP_U and HF_SUP_S as shown in the previous section.

As we shall see later, when $Bo > 0$, there are two possible cases of critical flow in the presence of two obstacles under the combined effects of gravity and surface tension. The first case corresponds to a situation in which a hydraulic fall occurs at the rightmost obstacle. In this case, the SUB_HF solution of pure gravity flow is used as an initial data in the numerical procedure. There are two types of solution that shall be discussed in §5.2.1. The second case corresponds

(a) $Bo = 0.0, F = 0.9006$

(b) Phase trajectory of (a).

(c) $Bo = 0.04, F = 0.8875$

(d) Phase trajectory of (c).
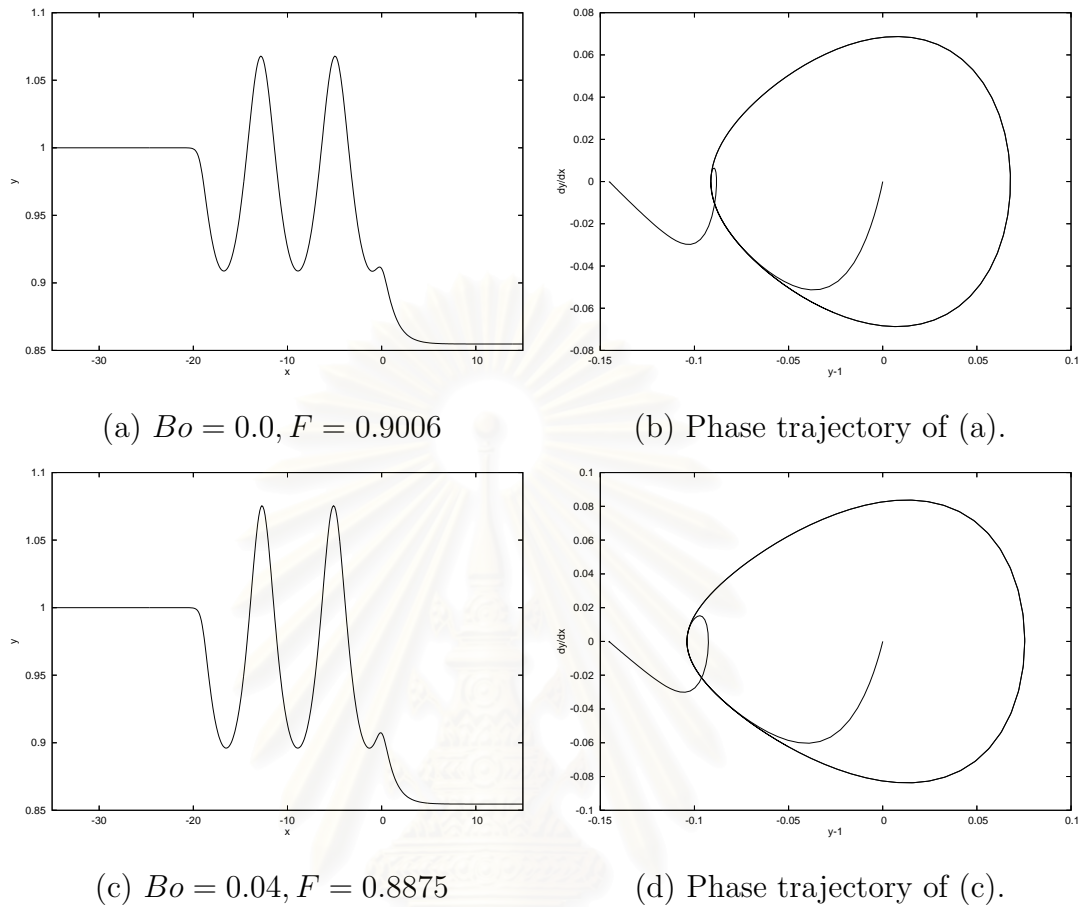
Figure 5.14: Solution profiles of type SUB_HF when $hob1 = hob2 = 0.10$. (a), (c) Fully nonlinear solutions for $Bo = 0.0$ and 0.04, respectively. (b), (d) Phase trajectories of the corresponding solutions (a) and (c).

to the flow in which a hydraulic fall occurs at the leftmost obstacle. Like in the first case, the HF_SUP_U and HF_SUP_S solutions of pure gravity flow are used to find the required numerical solutions. Two types of solution can be found for which one of these is the newly proposed solution. Detail of these solutions are presented in §5.2.2.

5.2.1 Hydraulic Fall at the Rightmost Obstacle

When a hydraulic fall occurs at the rightnost obstacle, there are two possible types of solution: (1) a profile with waves trapped between the obstacles, the so-

called "SUB_HF" and (2) a profile with depression wave right above the leftmost obstacle which shall be called "DF_HF". Free-surface profile of type (2) is similar to the one obtained in the experiments of Pratt [54].

1. Waves Trapped between the Obstacles (SUB_HF)

This type of solution is similar to the case of pure gravity flow $(Bo = 0)$, i.e., there are waves trapped between two obstacles followed by a hydraulic fall right over the rightmost obstacle. Typical free-surface profile for $hob1 = hob2 = 0.10, F = 0.8875$ and $Bo = 0.04$ is shown in Figure 5.14(c). The corresponding fully nonlinear phase trajectory in Figure 5.14(d) can be described as follows. The solution curve starts at a fixed point $y - 1 = 0$ with a first jump onto an inner periodic orbit. After moving clockwise some distance on this periodic orbit, there is a second jump onto a solitary wave orbit which then moves to another fixed point $y - 1 = \frac{2}{3}(F^2 - 1)$. Qualitatively, the phase trajectories of pure gravity problem and gravity-capillary problem do have similar pattern. However, the amplitude and wavelength of trapped waves and the Froude number are different as can be seen from the size of the inner periodic orbit and the a fixed point $y - 1 = \frac{2}{3}(F^2 - 1)$.

This solution type can only be found when for $Bo \leq 0.04$. The amplitude of waves trapped between the obstacles appears to be an increasing function of the Bond number. Figure 5.15 compares different solution profiles for various values of the Bond number. In this case, the Froude number F is treated as part of the solution. When $hob1 \geq hob2$, the Froude number appears to be a decreasing function of the Bond number. On the other hand, if $hob1 < hob2$, the Froude number becomes an increasing function of the Bond number. For example, when $hob1 = hob2 = 0.10$, the Froude number F is $0.9906, 0.8878$ and 0.8875 as $Bo = 0, 0.02$ and 0.04, respectively, but when $hob1 = 0.10, hob2 = 0.20$, the Froude

number F is $0.7469, 0.7594$ and 0.7742 as $Bo = 0, 0.02$ and 0.04, respectively. For given values of Bo and $hob1$, the Froude number decreases as the height of the rightmost obstacle $hob2$ increases as shown in Figure 5.16. However, when the Bond number Bo and the height of the rightmost obstacle $hob2$ are fixed, the relationship between the Froude number F and the height of the leftmost obstacle $hob1$ is no longer a monotone function. It appears that there exists a maximum value of Froude number in each case as shown in Figure 5.17.

For weakly nonlinear problem, the sfKdV model can be used to find the SUB_HF solution type. The weakly nonlinear profiles are shown in Figure 5.18, for $hob1 = 0.05, hob2 = 0.10$ and $Bo = 0, 0.10$ and 0.20. The fully nonlinear phase trajectories in Figure 5.14 (b) and (d) provide a qualitative check on the phase space analytic in Figure 5.18 (b), (d) and (f). It should be noted that weakly nonlinear solutions can be found for the Bond number between 0 and $\frac{1}{3}$.

2. Depression Wave over the Leftmost Obstacle with Hydraulic Fall (DF_HF)

Free-surface flow of this type is of uniform and symmetric depression wave in the neighborhood of the leftmost obstacle with a hydraulic fall right over the rightmost obstacle. Typical free-surface profile for $hob1 = hob2 = 0.10, F = 0.8599$ and $Bo = 0.40$ is shown in Figure 5.19(a). This solution is called the "DF_HF" solution and can be thought of as a hybrid between subcritical and critical flows over each obstacle. Pratt [54] found this DF_HF solution in his experiments when $hob1 < hob2$, but could not find the weakly nonlinear solution. In this thesis, it is shown that this type of solution can be found for the fully nonlinear problem with no restrictions on the values of $hob1$ and $hob2$. The phase trajectory in Figure 5.19(b) starts at a fixed point $y - 1 = 0$ with a negative vertical jump onto an

inner periodic orbit. After moving half cycle clockwise, it jumps back to the same fixed point. Then, there is a negative jump onto the solitary wave orbit and goes directly to another fixed point $y - 1 = \frac{2}{3}(F^2 - 1)$.

For given values of $hob1$ and $hob2$, amplitude of the depression wave at the leftmost obstacle decreases as the Bond number increases (see in Figure 5.20). As $Bo \downarrow \tilde{Bo}$, the upstream free-surface profile over the rightmost obstacle behaves in a similar manner as the case of hydraulic fall over a single obstacle (see Figure 4.18(c)), and the portion of depression wave at the rightmost obstacle tends to the shape of symmetric wave packet. Typical free-surface profiles are shown in Figure 5.21 (a)-(f) for $hob1 = hob2 = 0.10$ and $Bo = 0.40, 0.35, 0.30, 0.25, 0.23$ and 0.21, respectively. Here $\tilde{Bo}$ is the minimum value of the Bond number which depends on the obstacle heights $hob1$ and $hob2$. For example, $\tilde{Bo} = 0.21$ for $hob1 = hob2 = 0.10$.

Again, the Froude number F is part of the solution and appears to be functions of the Bond number Bo and the height of the rightmost obstacle $hob2$. Figure 5.22 (a)-(c) show the dependence of the Froude number F and the amplitude of depression wave over the leftmost obstacle $|A|$ on the Bond number Bo for given values of $hob1$ and $hob2$. Let $\hat{Bo}$ be a value of Bond number such that the Froude number takes on its minimal. For example, $\hat{Bo}$ is 0.40, when $hob1 = hob2 = 0.20$. The amplitude $|A|$ is small when Bo is close to $\hat{Bo}$ with a small variation as Bo increases.

5.2.2 Hydraulic Fall at the Leftmost Obstacle

In case of pure gravity flow ($Bo = 0$), there are two types of solution: HF_SUP_U and HF_SUP_S. The first type is a solution with hydraulic fall at the leftmost obstacle followed by an elevation wave which is perturbed from a uniform stream

over the rightmost obstacle. The other type is similar to the HF_SUP_U except that the elevation wave over the rightmost obstacle is perturbed from a solitary wave.

In this consideration, we use both solutions, HF_SUP_U and HF_SUP_S, from pure gravity flow as initial data for computing the corresponding solution types. It is found that, when HF_SUP_U is used as an initial profile, a new family of capillary-gravity waves can be found for *large Bond number*. As for HF_SUP_S initial data, there exists solution only for small Bond number for which the solution profile is similar to HF_SUP_S.

1. HF_SUP_S Initial Data.

Solution in this case is characterized by a hydraulic fall at the leftmost obstacle followed by an elevation wave right above the rightmost obstacle which is the perturbation of a solitary wave. This solution can be found only for small Bond numbers, $0 \leq Bo \leq 0.04$. Free-surface profile is similar to the case of pure gravity problem. Typical free-surface profiles with the phase trajectories are shown in Figure 5.23. Each trajectory starts at a fixed point $y - 1 = 0$ with a negative jump onto the solitary wave orbit. It then moves clockwise one cycle on this orbit and goes directly to another fixed point $y - 1 = \frac{2}{3}(F^2 - 1)$.

Size of the above solitary wave orbit depends on the value of Bond number Bo and clearly relates to the maximum level of an elevation wave over the rightmost obstacle. This maximum level of an elevation wave over the rightmost obstacle increases as the Bond number increases and ultimately approaches the limiting configuration of a $120°$ angle at the crests (see in Figure 5.24). The fixed point $y - 1 = \frac{2}{3}(F^2 - 1)$ moves to the left in the phase trajectory as the Bond number increases. This implies that the Froude number F is a decreasing function

of the Bond number Bo. A relationship between the Bond number Bo and the Froude number F is shown in Figure 5.25.

Figure 5.26 shows that amplitude of the elevation wave over the rightmost obstacle $|A|$ is an increasing function of Bo for given values of $hob1$ and $hob2$. In addition, as $hob1$ and $hob2$ increases, the solution can be found only for small values of the Bond number Bo. A comparison of free-surface profiles for various values of $hob2$ is shown in Figure 5.27. The behavior of free-surface profile is same in case of pure gravity problem, i.e., the maximum level of an elevation wave over the rightmost obstacle decreases as the $hob2$ increases and ultimately approaches the far upstream level.
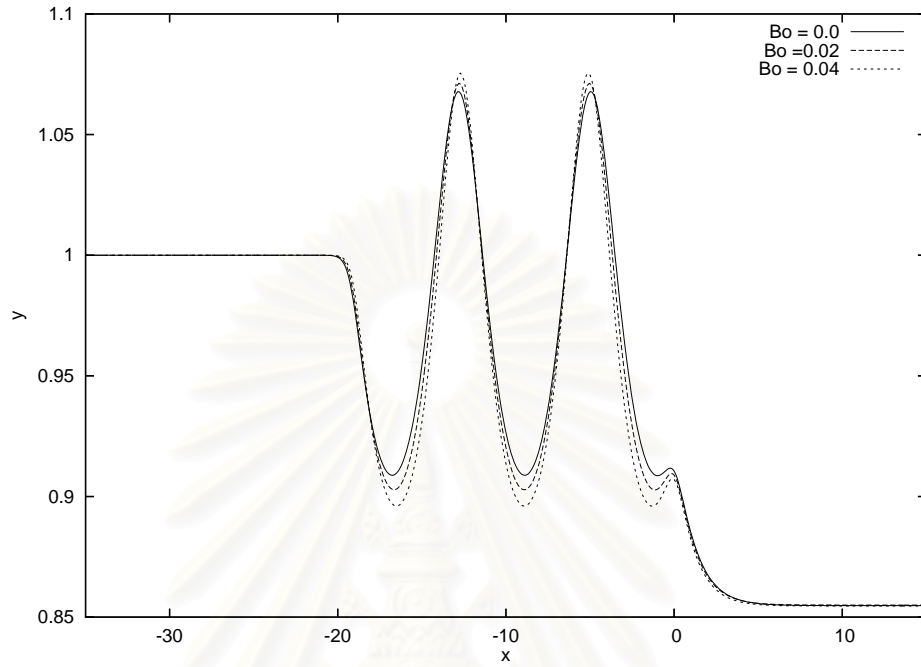
(a) $hob1 = hob2 = 0.10$
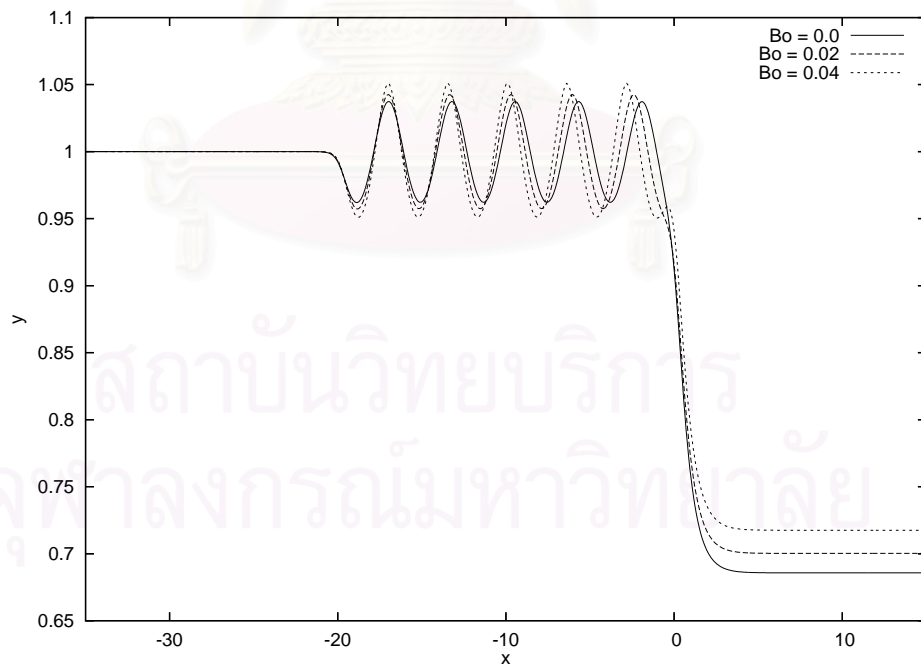
(b) $hob1 = 0.10, hob2 = 0.20$

Figure 5.15: Typical free-surface profiles of SUB_HF for $Bo = 0.0, 0.02$ and 0.04.
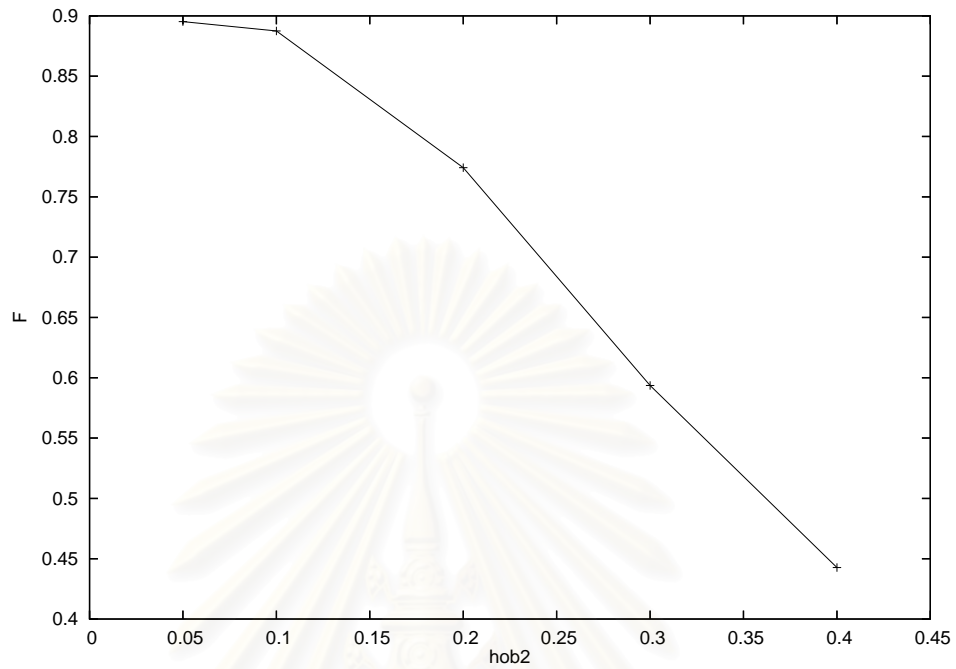
Figure 5.16: Relationship between the rightmost obstacle height $hob2$ and the Froude number F for $hob1 = 0.10$ and $B = 0.04$.
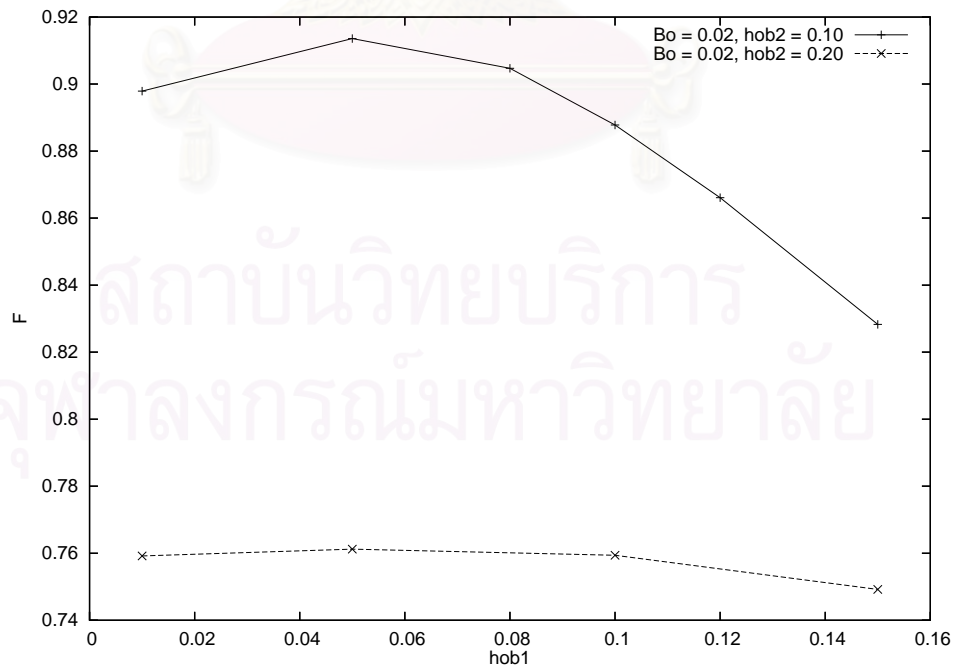
Figure 5.17: Relationship between the leftmost obstacle height $hob1$ and the Froude number F.
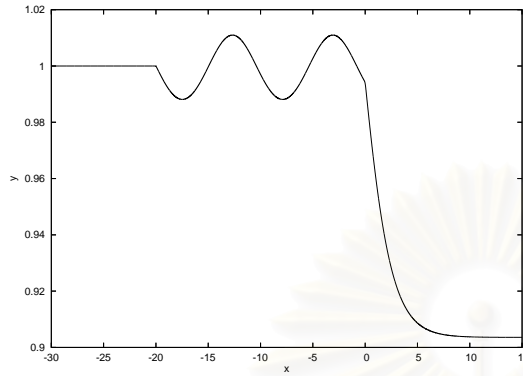
(a) $Bo = 0.0, F = 0.9248$
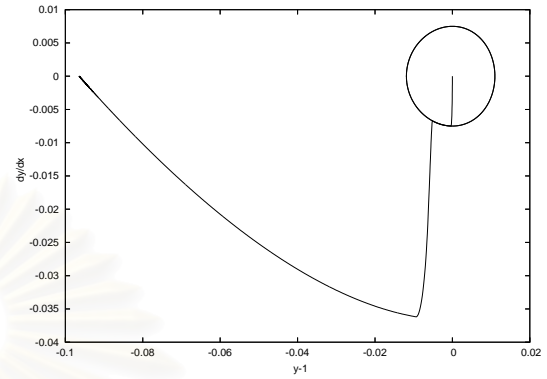
(b) Phase trajectory of (a).
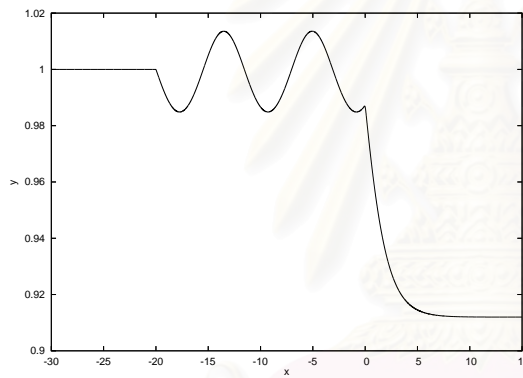
(c) $Bo = 0.10, F = 0.9317$
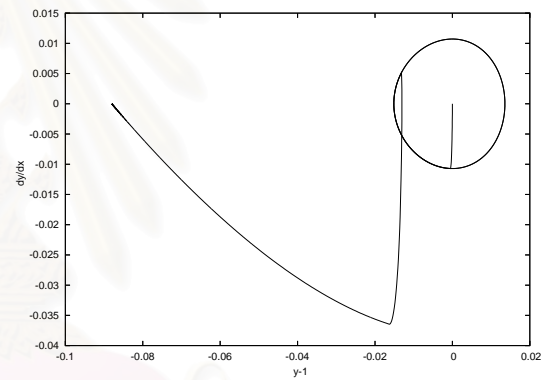
(d) Phase trajectory of (c).
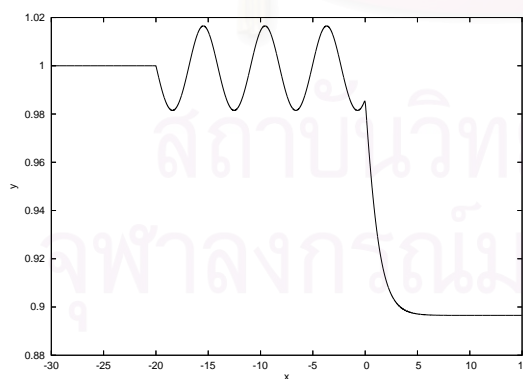
(e) $Bo = 0.20, F = 0.9191$
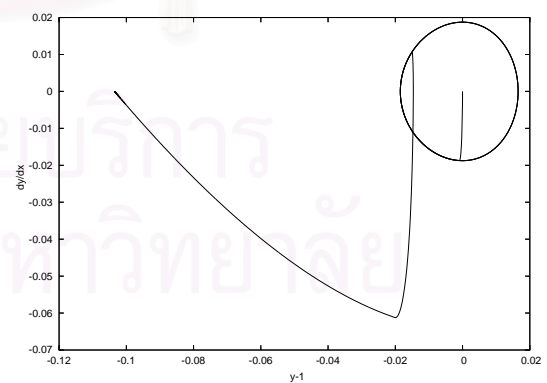
(f) Phase trajectory of (e).

Figure 5.18: Typical free-surface profiles of the weakly nonlinear problem of SUB_HF solution for $hob1 = 0.05, hob2 = 0.10$ and $x_d = 20.0$.
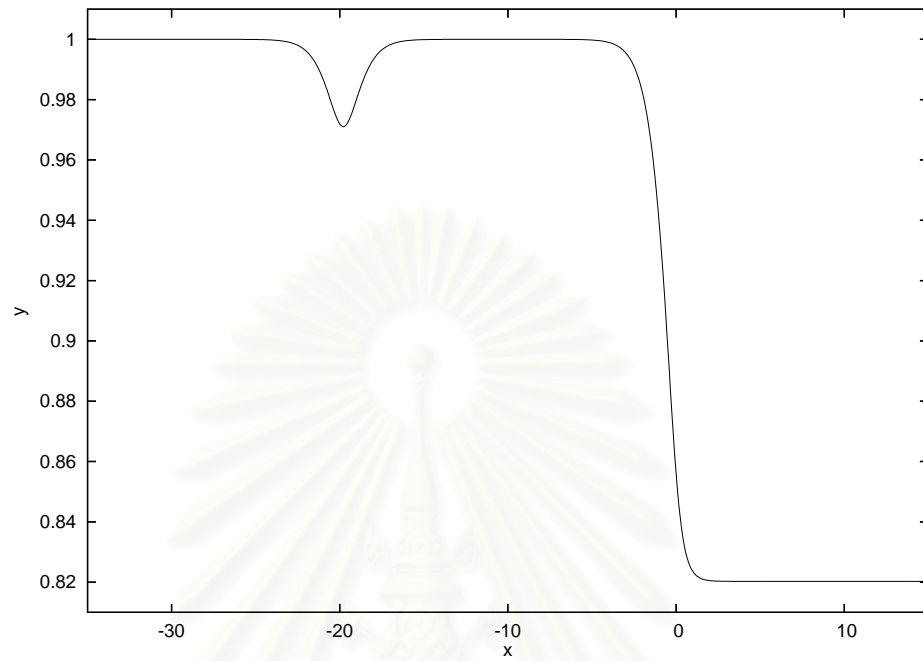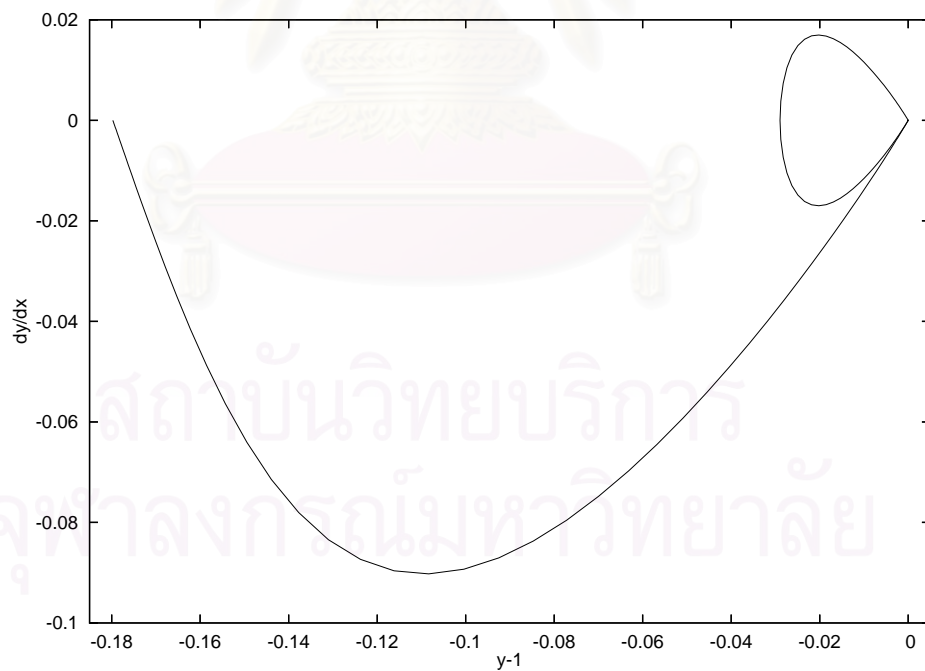
Figure 5.19: Typical free-surface profile of DF_HF solution for $hob1 = hob2 = 0.10, F = 0.8599$ and $Bo = 0.40$. (a) Fully nonlinear profile. (b) Phase trajectory.
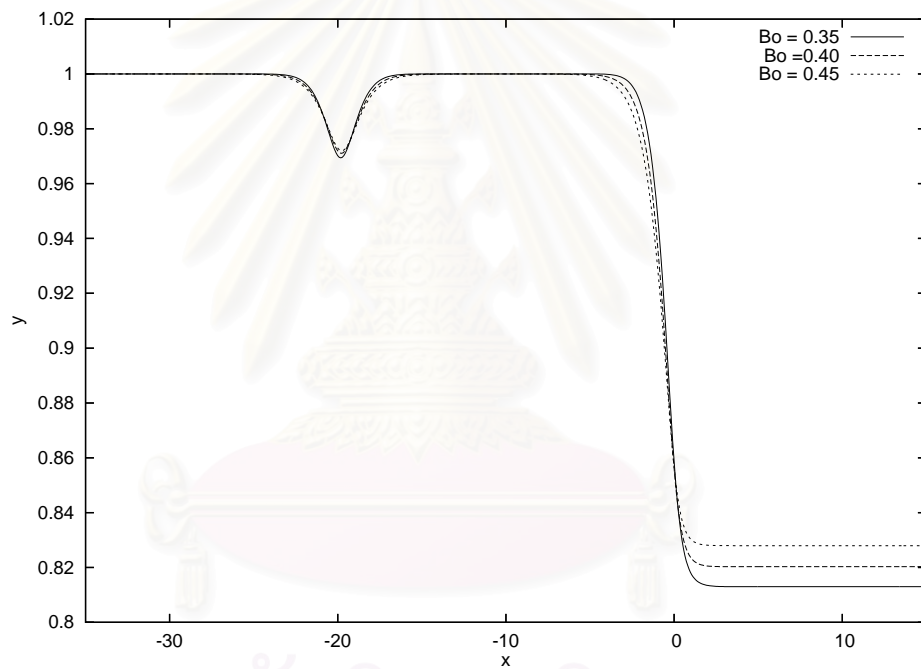
Figure 5.20: Typical free-surface profiles of DF_HF solution for $hob1 = hob2 = 0.10$.

(a) $Bo = 0.40$

(b) $Bo = 0.35$

(c) $Bo = 0.30$

(d) $Bo = 0.25$

(e) $Bo = 0.23$

(f) $Bo = 0.21$
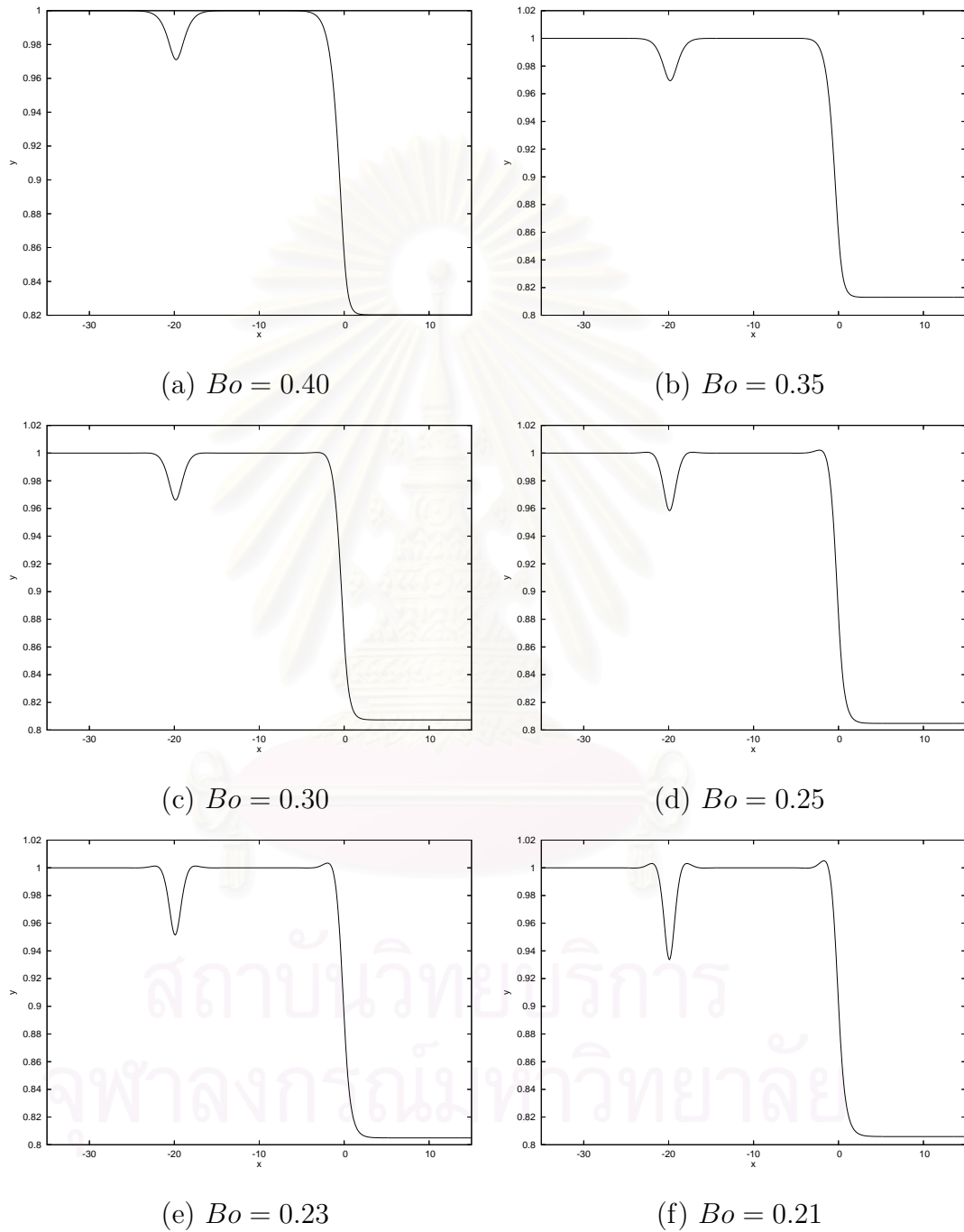
Figure 5.21: Typical free-surface profiles of DF_HF solution for $hob1 = hob2 = 0.10$ and various values of Bo.
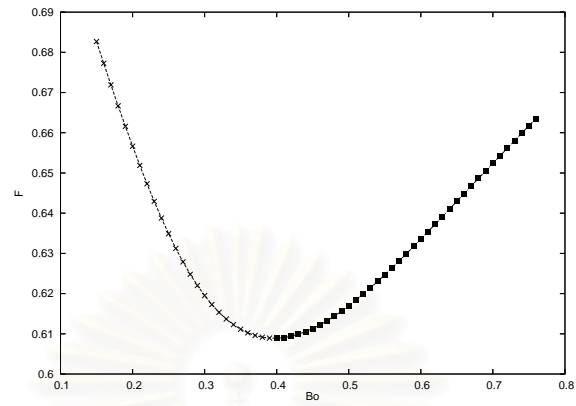
(a)
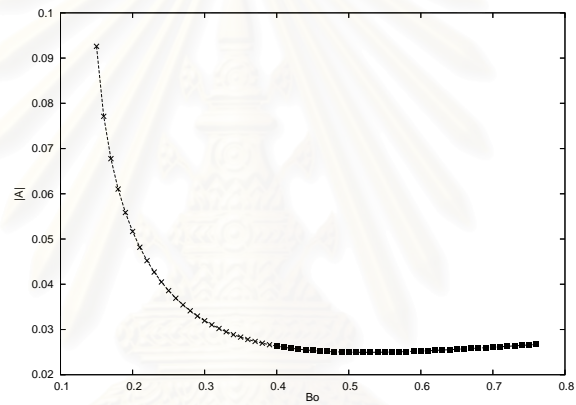
(b)
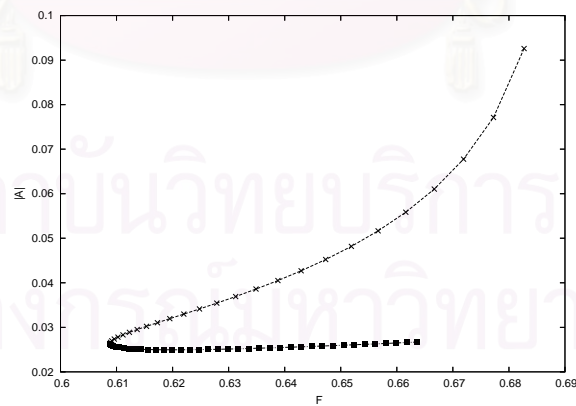
(c)

Figure 5.22: Relationships between (a) the Bond number Bo and the Froude number F, (b) Bo and the amplitude of depression wave over the leftmost obstacle $|A|$, and (c) F and $|A|$ of the DF_HF solution type for $hob1 = hob2 = 0.20$.
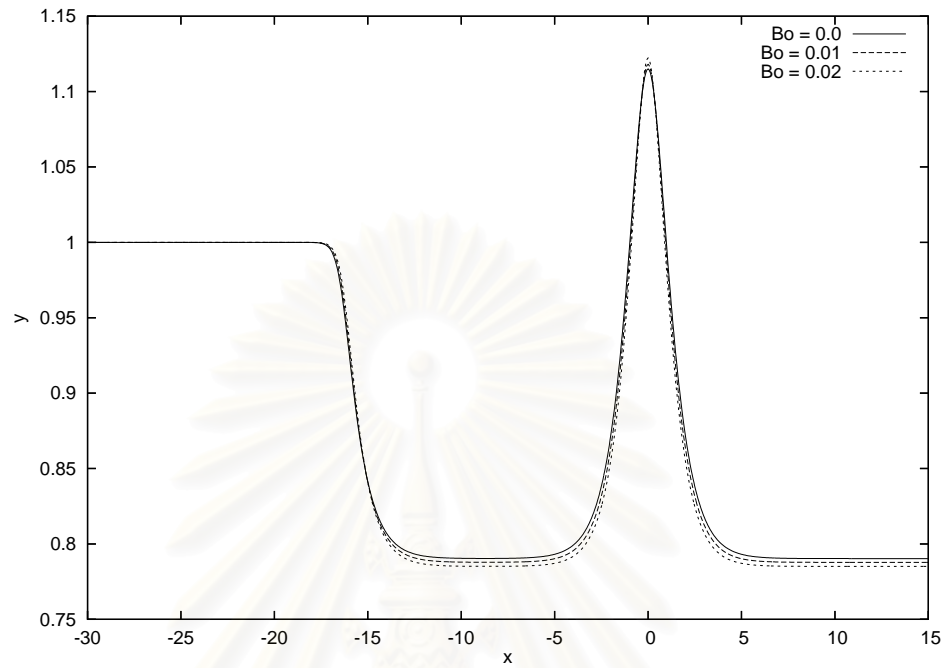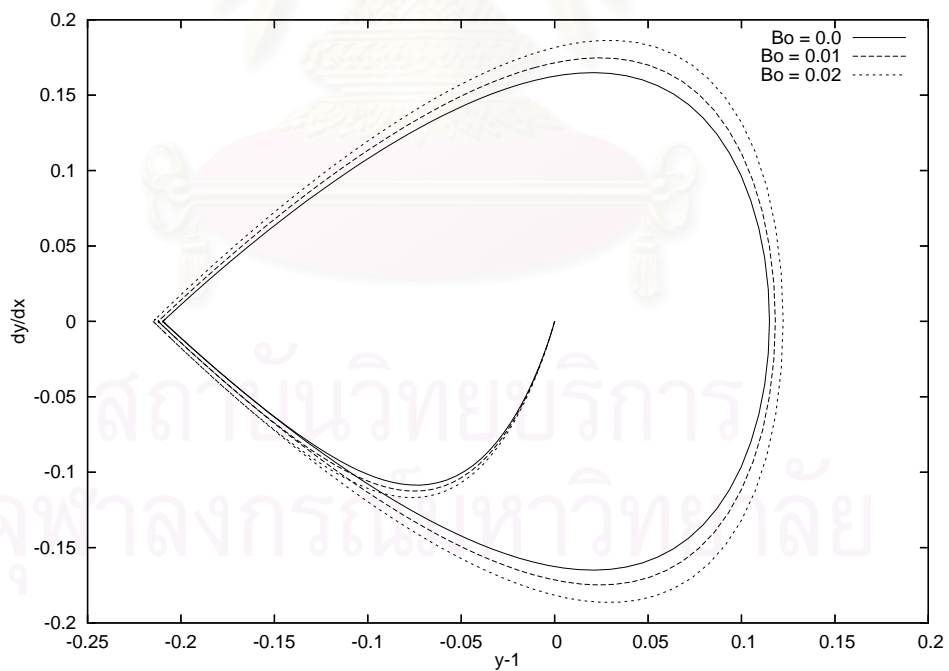
Figure 5.23: Typical free-surface profiles of HF_SUP_S solution for $hob1 = 0.15, hob2 = 0.10$. (a) Fully nonlinear profiles. (b) Phase trajectories.
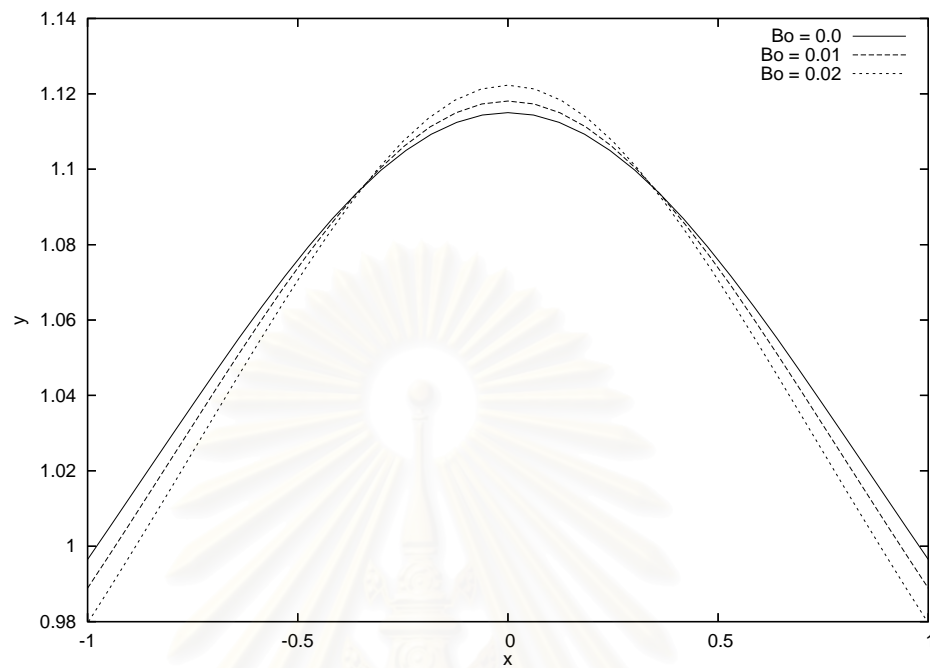
Figure 5.24: Free-surface profiles in the vicinity of the rightmost obstacle of HF_SUP_S

solution for $hob1 = 0.15, hob2 = 0.10$.
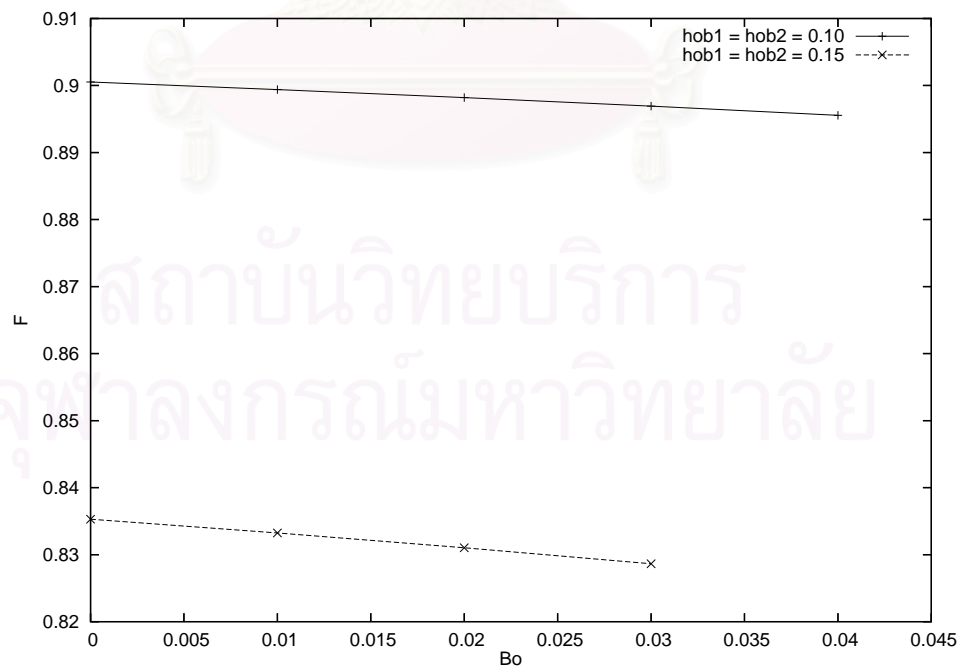
Figure 5.25: Relationship between the Bond number Bo and the Froude number F for

HF_SUP_S solution.
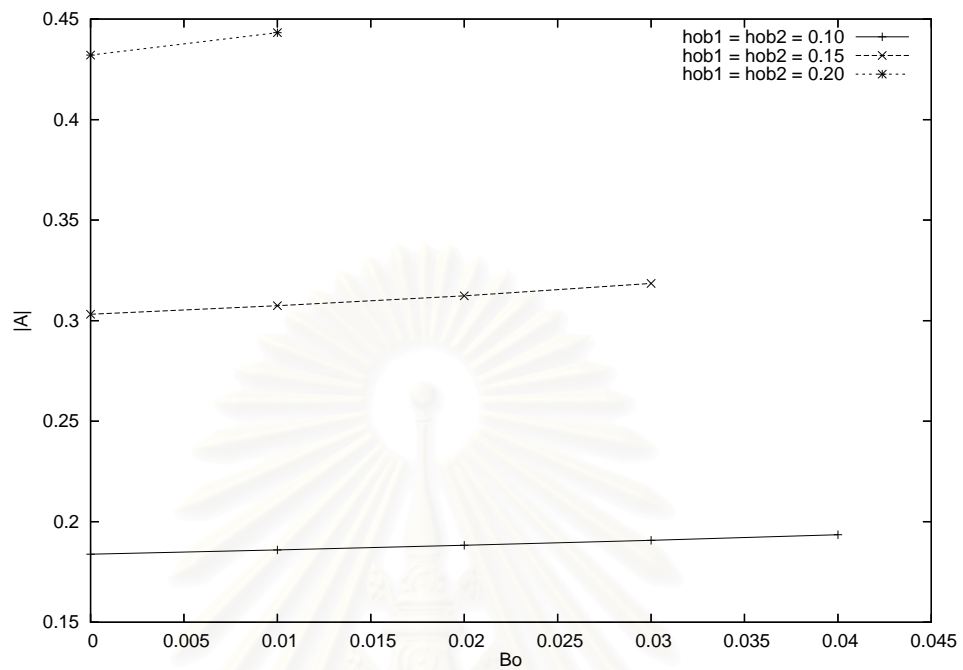
Figure 5.26: Relationship between the Bond number Bo and the amplitude $|A|$ of elevation wave over the rightmost obstacle for HF_SUP_S solution.
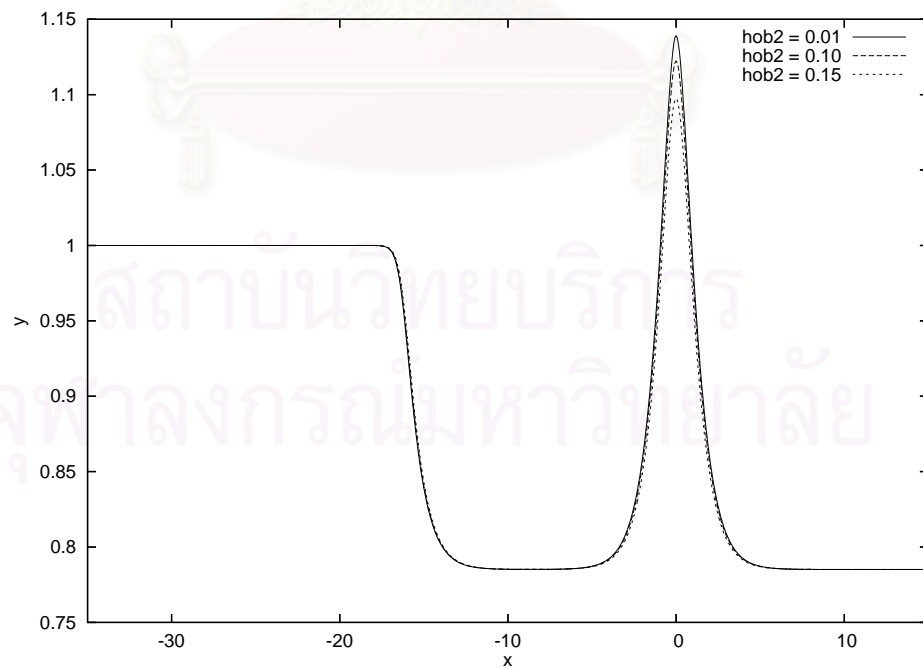
Figure 5.27: Typical free-surface profiles of HF_SUP_S solution for $hob1 = 0.15, F = 0.8310, Bo = 0.02$ and various values of $hob2$.

2. HF_SUP_U Initial Data

When the HF_SUP_U solution of pure gravity problem is used as an initial guess for $Bo > 0$, there are two possible types of solution such that a hydraulic fall occurs at the leftmost obstacle. First type of solution can be found for small Bond number and does have similar profile as in the case of HF_SUP_S. The other is a new type of solution which can be found only when $Bo > 0.04$. This solution is characterized by a hydraulic fall followed by waves trapped between the obstacles.

The implication of small Bond number is that gravity is a dominant force. So, as we may expect, the solution profile is similar to the case of pure gravity problem. From the numerical calculations, this solution can be found only for small value of the Bond number, i.e., $0 \leq Bo \leq 0.04$. Typical fully nonlinear free-surface profiles are shown in Figure 5.28(a) for $hob1 = 0.15, hob2 = 0.10$ and $Bo = 0.0, 0.02$ and 0.04. The phase trajectories in Figure 5.28(b) show similar patterns to the case of flows without surface tension. At the fixed point $y - 1 = \frac{2}{3}(F^2 - 1)$, we can see that the Froude number depends on the Bond number Bo. This relationship is shown in Figure 5.29. In addition, amplitude of the elevation wave over the rightmost obstacle $|A|$ is merely an increasing function of the Bond number Bo (see Figure 5.30). These behaviors are also found in the previous case that used HF_SUP_S as the initial data.

For given values of $hob1$ and Bo, in the neighborhood of the rightmost obstacle, the profile is symmetric with respect to the obstacle for all values of $hob2$. In particular, the effect of $hob2$ is solely on the amplitude of elevation wave over the rightmost obstacle $|A|$ (see Figure 5.31).

The above numerical solution ceases to exist when $Bo > 0.04$. However, when Bo is chosen to be sufficiently large, there is a new type of solution. This solution is characterized by a hydraulic fall at the leftmost obstacle, and an elevation

wave over the rightmost obstacle with waves trapped between them. From this characteristic, it shall be denoted by "HF_SUP_UT". Typical free-surface profile is shown in Figure 5.32(a) for $hob1 = 0.20, hob2 = 0.15, F = 0.4978$ and $Bo = 0.35$. Its trajectory in Figure 5.32(b) starts at a fixed point $y - 1 = 0$ with a negative jump onto the solitary wave orbit and moves to another fixed point. Then, there is a positive jump to the periodic orbit around the second fixed point. After moving clockwise some distance on this orbit, there is another positive jump back to the second fixed point. So far, *this solution type can be found only in the fully nonlinear problem.*

As the Bond number increases, the number of waves trapped between the obstacles decreases while the values of Froude number change intermittently. Profiles in Figure 5.33 (a)-(f) are shown for various values of Bond number. For given values of Bo and $hob1$, amplitude of the waves trapped between the obstacles increases as the obstacle size $hob2$ gets bigger (see Figure 5.34). This may lead to a conjecture that these waves would ultimately approach a limiting configuration with a bubble at the trough (Aider and Debiane [1]). Due to the limitation of our present numerical technique, we are unable to calculate these bubble solutions. The relationship between $hob2$ and F for $Bo = 0.40$ and $hob1 = 0.10$ is shown in Figure 5.35.

Table 5.2 summarizes the solution types of free-surface flows over two submerged obstacles with gravity and surface tension. In this case, there are 5 types of solution: SUB_HF, DF_HF, HF_SUP_U, HF_SUP_S and HF_SUP_UT. The DF_HF solution is the newly discovered numerical solution, and the HF_SUP_S and HF_SUP_UT are also the two new solutions of free-surface flows over two obstacles.

5.3   Conclusions

Free-surface flow over two obstacles under the influence of gravity and surface tension is considered in this chapter. For pure water at 25°C, the surface tension T is 0.07197 N/m and the density is 998 km/m^3. The corresponding values of Bond number in this case are 0.0736 and 0.2943 when the water depth is 1.0 and 0.5 cm, respectively. In case of seawater, the water density is 1025 km/m^3 ("Ocean - Density and Pressure". Encyclopedia Britannica., USA, 1965.). For water in the Gulf of Thailand whose average depth is 45 m, the flow is gravity-dominated since the Bond number is very small (approximately 7.96×10^{-11}). Fully nonlinear problem is solved numerically by using the boundary integral equation technique. Previous solutions obtained by Pratt [54], Belward [3], Dias and Vanden-Broeck [19] and Binder, Vanden-Broeck and Dias [9] are completely recovered and new types of solution are proposed for both pure gravity and gravity-capillary flows.

In the case of pure gravity problem, all possible flow regimes (subcritical, supercritical and critical flows) are considered. There are 8 types of solution as depicted in Table 5.1 : SUB_SUB, SUB_SYM, DF_DF, SUP_SUP, SUP_TRAP, SUB_HF, HF_SUP_U, and HF_SUP_S with 9 free-surface profiles. For SUB_SUB type, there are two different flow patterns. First, the amplitude of waves trapped between the obstacles is *larger than* those on downstream of the rightmost obstacle. This solution was found earlier by Binder, Vanden-Broeck and Dias [9]. For the other solution of this type, the amplitude of waves trapped between the obstacles is *smaller than* those on downstream of the rightmost obstacle. It should be noted that these solutions correspond to the same values of *hob*1 and *hob*2 but for different values of the Froude number.

In summary, the main results concern new solutions of the gravity and gravity-capillary waves over two obstacles. For gravity waves, there are two new

types of solution, DF_DF and HF_SUP_S. The DF_DF solution of subcritical flow is characterized by the depression wave or drag-free profile over each obstacle. This can be found only when the Froude number F and the height of the obstacles $hob1$ and $hob2$ are small. The HF_SUP_S solution of the critical flow regime is characterized by a hydraulic fall over the leftmost obstacle with an elevation wave over the rightmost obstacle. This solution type can be found for the same set of parameters as the HF_SUP_U solution. To obtain HF_SUP_S solution, the choice of the initial data is important as suggested on page 70.

For critical flows of the gravity-capillary waves, this study focuses on the case in which the flow is uniform on both far upstream and far downstream. There are 5 types of solution: SUB_HF, DF_HF, HF_SUP_U, and HF_SUP_S, and HF_SUP_UT. Among these, HF_SUP_UT is a new solution which is the perturbation of HF_SUP_U solution. This solution can be found for larger Bond number. The other new solution DF_HF is the case in which there is a depression wave over the leftmost obstacle and a hydraulic fall over the rightmost obstacle. It was first discovered in the experiments of Pratt [54] when $hob1 < hob2$. Our numerical solutions confirm the existence of this flow pattern.

Next question to be answered in the future study should concern the stability of these solutions. One of the several approaches is to solve numerically the time-dependent solutions of this fully nonlinear problem by using, for example, a semi-Lagrangian approach.
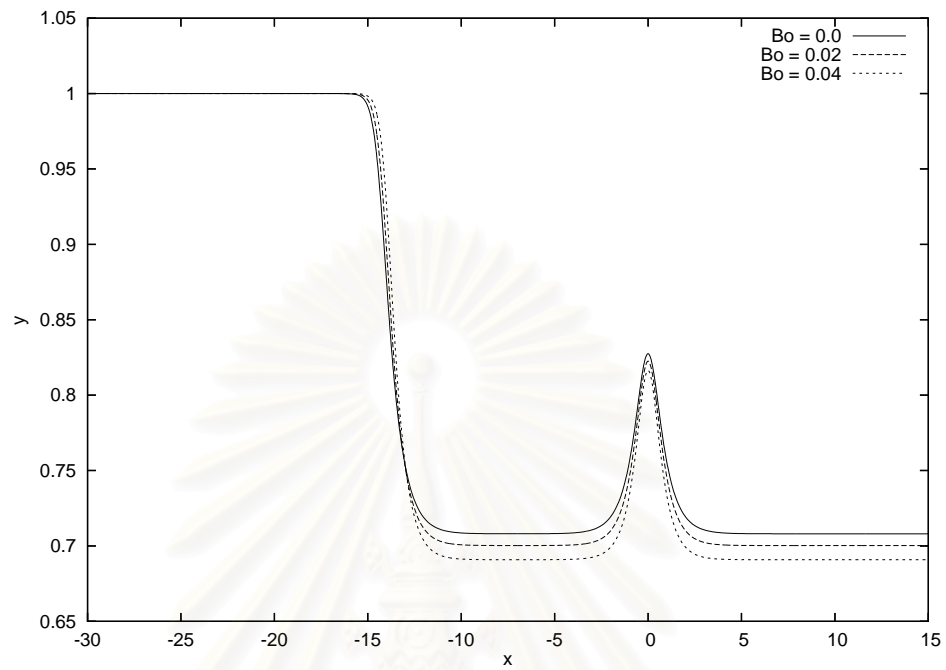
(a)
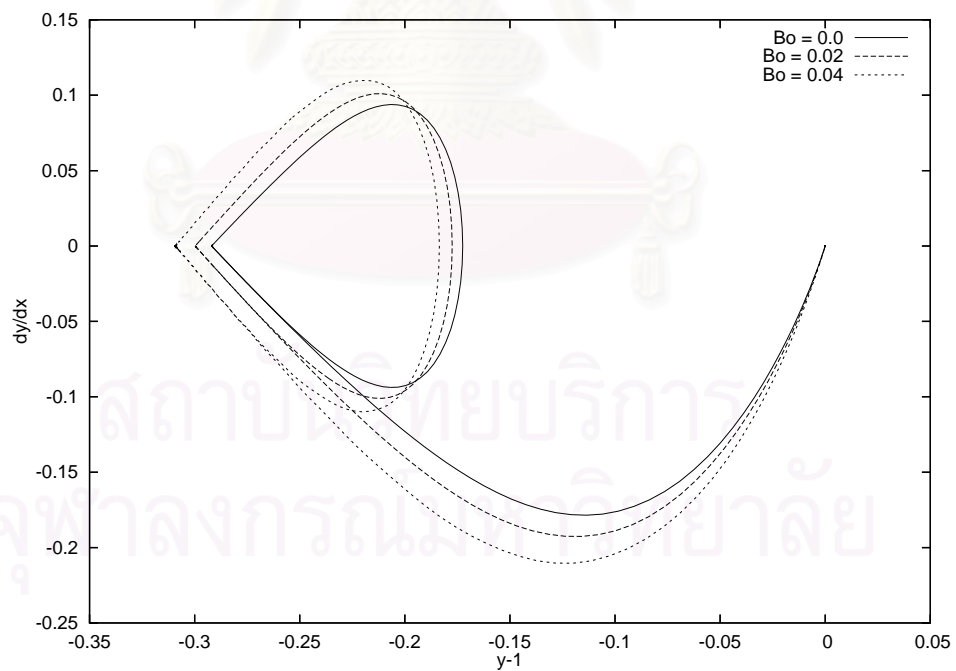
(b)

Figure 5.28: Typical free-surface profiles of HF_SUP_U solution for $hob1 = 0.15$ and $hob2 = 0.10$. (a) Fully nonlinear profiles. (b) Phase trajectories.
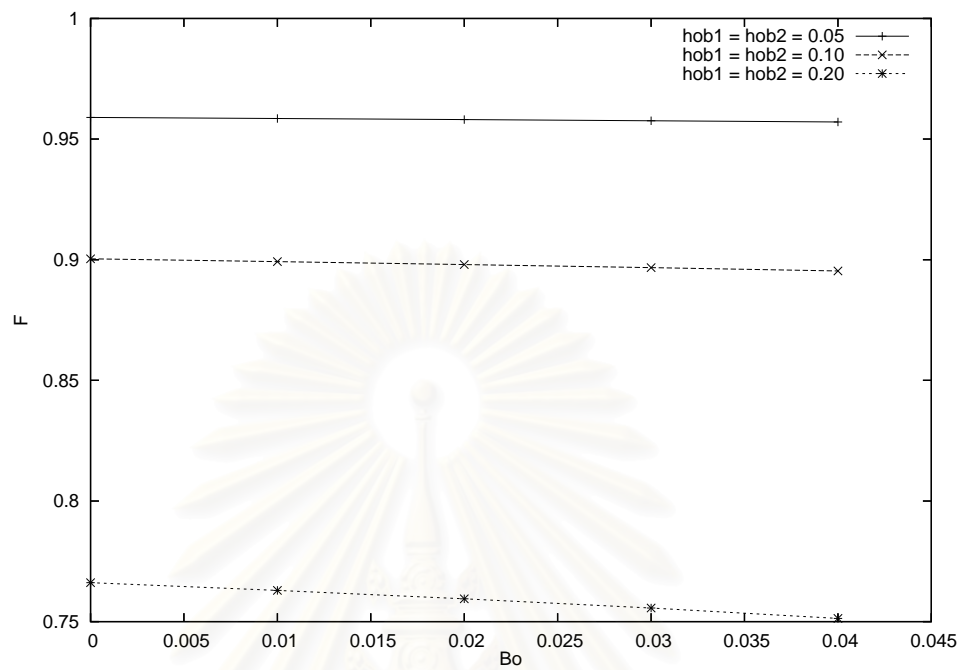
Figure 5.29: Relationship between the Bond number Bo and the Froude number F of HF_SUP_U solution.
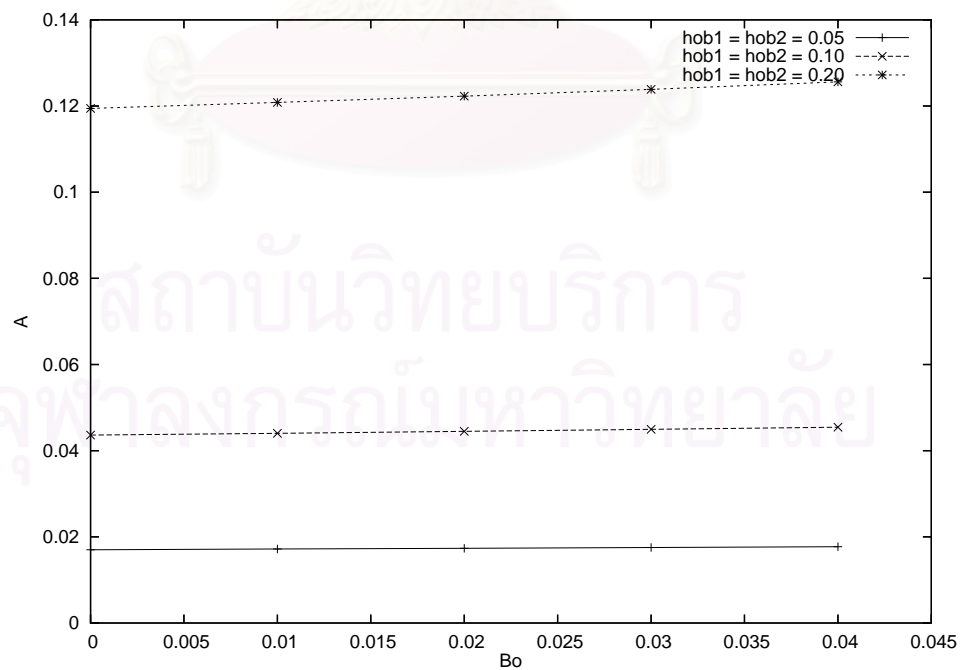
Figure 5.30: Relationship between the Bond number Bo and the amplitude $|A|$ of elevation wave over the rightmost obstacle of HF_SUP_U solution.
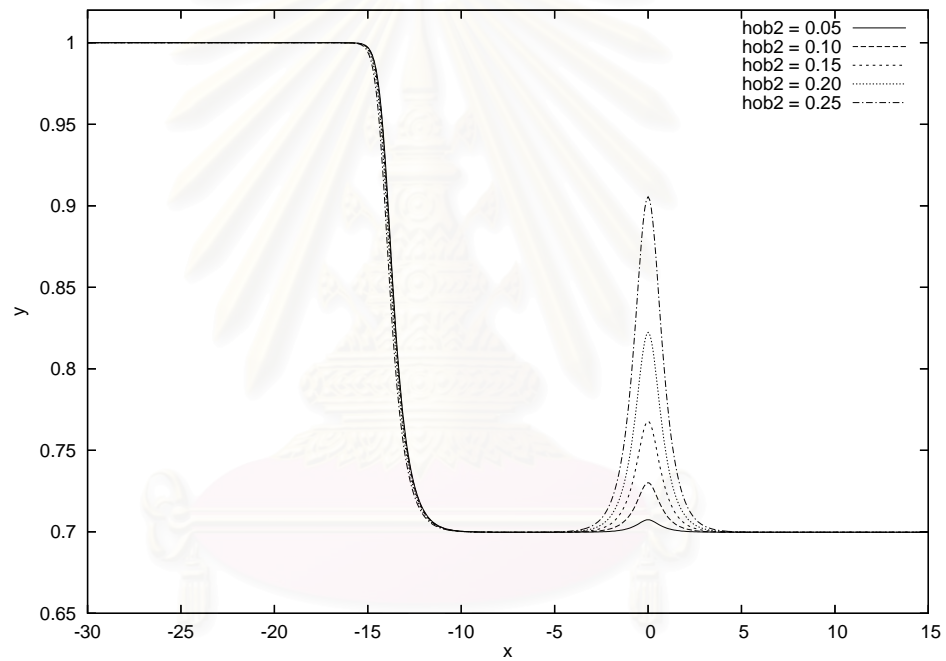
Figure 5.31: Typical free-surface profiles of HF_SUP_U solution, for $hob1 = 0.20, F = 0.7590, Bo = 0.02$, and various values of $hob2$.
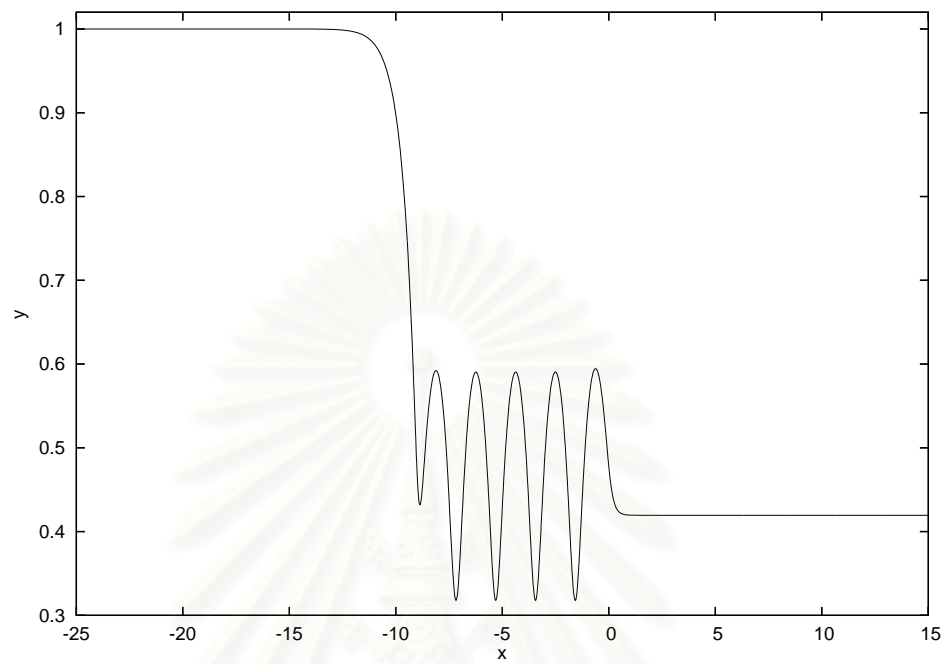
(a)
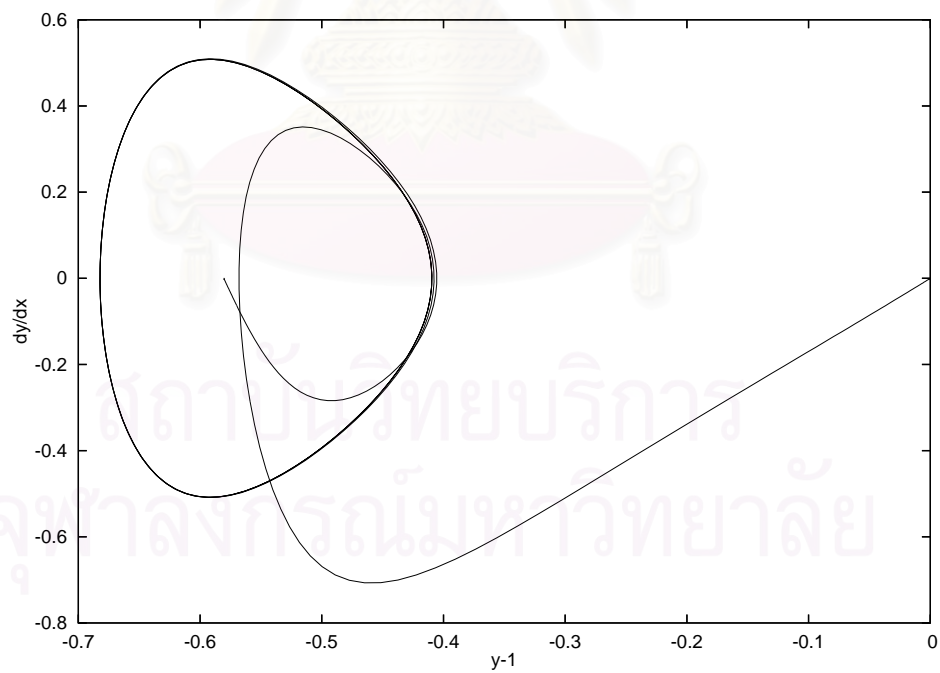
(b)

Figure 5.32: Typical free-surface profiles of HF_SUP_U solution for $hob1 = 0.20, hob2 = 0.15, F = 0.4978$ and $Bo = 0.35$. (a) Fully nonlinear profiles. (b) Phase trajectories.

(a) $Bo = 0.30, F = 0.5407$

(b) $Bo = 0.35, F = 0.4822$

(c) $Bo = 0.40, F = 0.7081$

(d) $Bo = 0.50, F = 0.5555$

(e) $Bo = 0.55, F = 0.7286$

(f) $Bo = 0.60, F = 0.6717$
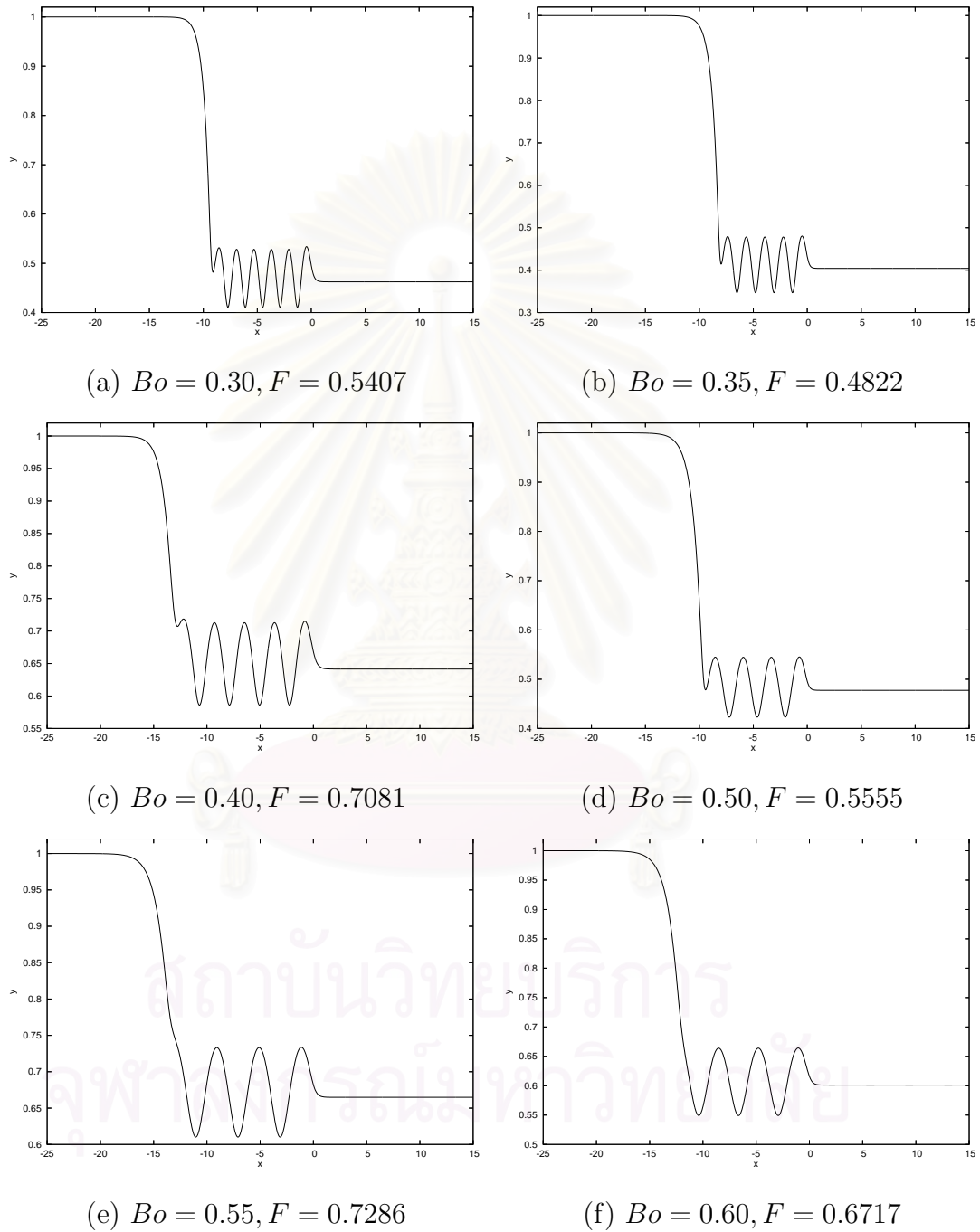
Figure 5.33: Typical free-surface profiles of HF_SUP_U solution for $hob1 = 0.20, hob2 = 0.10$ and various values of Bo.

(a) $hob2 = 0.01, F = 0.8598$

(b) $hob2 = 0.05, F = 0.8533$

(c) $hob2 = 0.10, F = 0.8084$

(d) $hob2 = 0.15, F = 0.7079$

(e) $hob2 = 0.18, F = 0.5918$
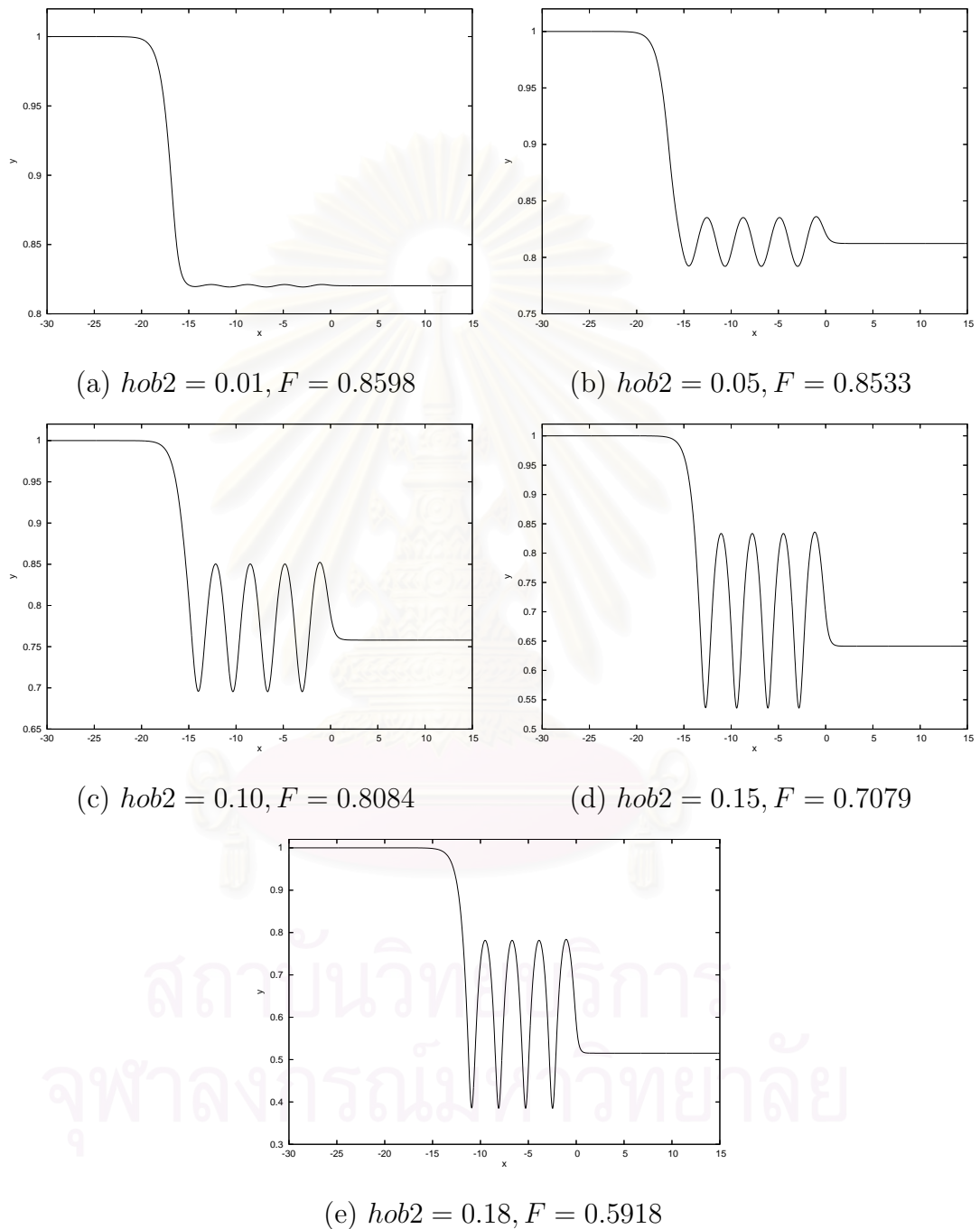
Figure 5.34: Typical free-surface profiles of HF_SUP_U solution for $hob1 = 0.10, Bo = 0.40$ and various values of $hob2$.
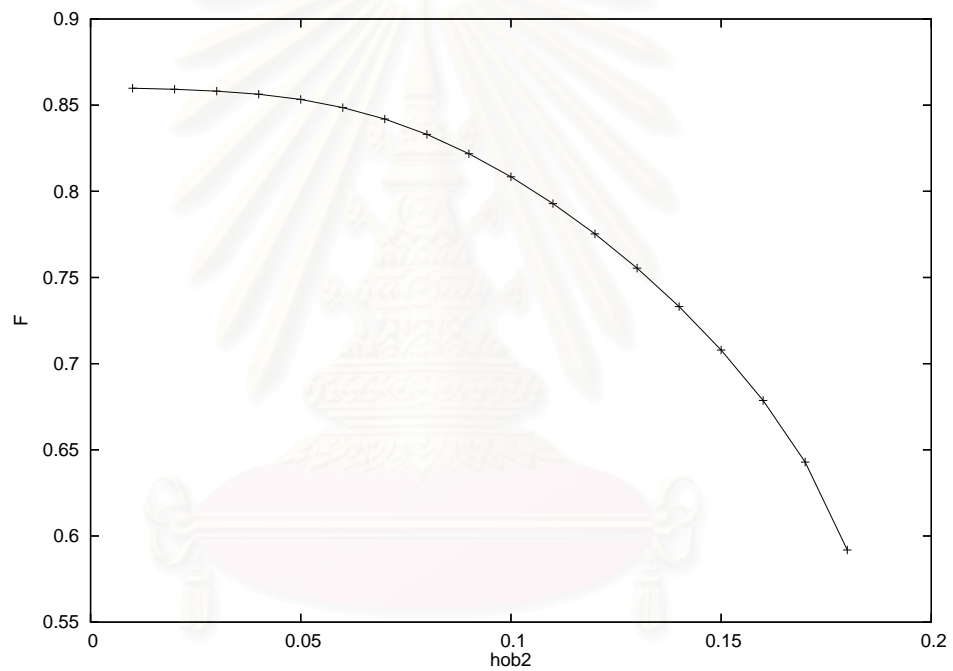
Figure 5.35: Relationship between the rightmost obstacle height $hob2$ and the Froude number F for $Bo = 0.40$ and $hob1 = 0.10$.
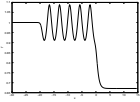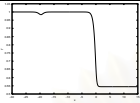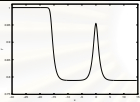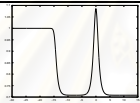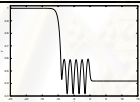
Solution type	P[54]	Present work
1 SUB_HF	$\checkmark$	$\checkmark$
2 DF_HF	$\checkmark$	$\checkmark^*$
3 HF_SUP_U	$\checkmark$	$\checkmark$
4 HF_SUP_S		$\checkmark^*$
5 HF_SUP_UT		$\checkmark^*$

Table 5.2: Solution types of free-surface flows over two obstacles under gravity and surface tension. The symbol $\checkmark$ denotes the existing solutions and $\checkmark^*$ denotes a new family of numerical solutions. P[54]: Experimental results of Pratt [54].

REFERENCES

[1] Aider, R., Debiane, M.: A method for the calculation of nonsymmetric steady periodic capillary-gravity waves on water of arbitrary uniform depth, *C. R. Mecanique* **334**, 387-392 (2006).

[2] Akylas, T. R.: On the excitation of long nonlinear water waves by a moving pressure distribution, *J. Fluid Mech.* **141**, 455-466 (1984).

[3] Belward, S. R.: Fully nonlinear flow over successive obstacles: hydraulic fall and supercritical flows, *J. Austral. Math. Soc. Ser. B.* **40**, 447-458 (1999).

[4] Belward, S. R., Forbes, L. K.: Fully nonlinear two-layer flow over arbitrary topography, *J. Eng. Math.* **27**, 419-432 (1993).

[5] Belward, S. R., Forbes, L. K.: Interfacial waves and hydraulic falls: some applications to atmospheric flows in the lee of mountains, *J. Eng. Math.* **29**, 161-179 (1995).

[6] Belward, S. R., Read, W. W., Higgins, P. J.: Efficient series solutions for non-linear flow over topography, *ANZIAM J.* **44**(E), C96-C113 (2003).

[7] Belward, S. R., Higgins, P. J., Read, W. W.: Optimising series solution methods for flow over topography - Part 2, *ANZIAM J.* **46**(E), C1286-C1295 (2005).

[8] Binder, B. J., Vanden-Broeck, J.-M.: The effect of disturbances on the flows under a sluice gate and past an inclined plate, *J. Fluid Mech.* **576**, 475-490 (2007).

[9] Binder, B. J., Vanden-Broeck, J.-M., Dias, F.: Forced solitary waves and fronts past submerged obstacles, *Chaos* **15**, 037106 (2005).

[10] Champneys, A. R., Vanden-Broeck, J.-M., Lord, G. J.: Do true elevation gravity-capillary solitary waves exist? a numerical investigation, *J. Fluid Mech.* **454**, 403-417 (2002).

[11] Choi, J. W., An, D., Lim, C, Park, S.: Symmetric surface waves over a bump, *J. Korean Math. Soc.* **40**(6), 1051-1060 (2003).

[12] Choi, J. W., Sun, S. M., Shen, M. C.: Steady capillary-gravity waves on the interface of a two layer fluid over an obstruction - forced modified KdV equation, *J. Eng. Math.* **28**, 193-210 (1994).

[13] Choi, J. W., Sun, S. M., Whang, S. I.: Supercritical surface gravity waves generated by a positive forcing, *Eur. J. Mech. B Fluids* **27**, 750-770 (2008).

[14] Debnath, L.: Some nonlinear evolution equations in water waves, *J. Math. Anal. Appl.* **251**, 488-503 (2000).

[15] Dias, F., Kharif, C.: Nonlinear gravity and capillary-gravity waves, *Annu. Rev. Fluid Mech.* **31**, 301-346 (1999).

[16] Dias, F., Vanden-Broeck, J.-M.: Generalised critical free-surface flows, *J. Eng. Math.* **42**, 291-301 (2002).

[17] Dias, F., Vanden-Broeck, J.-M.: Open channel flows with submerged obstructions, *J. Fluid Mech.* **206**, 155-170 (1989).

[18] Dias, F., Vanden-Broeck, J.-M.: Steady two-layer flows over an obstacle, *Phil. Trans. R. Soc. Lond. A* **360**, 2137-2154 (2002).

[19] Dias, F., Vanden-Broeck, J.-M.: Trapped waves between submerged obstacles, *J. Fluid Mech.* **509**, 93-102 (2004).

[20] Dias, F., Vanden-Broeck, J.-M.: Two-layer hydraulic falls over an obstacle, *Eur. J. Mach. B/Fluids.* **23**, 879-898 (2004).

[21] Faltas, M. S., Hanna, S. N., Abd-el-Malek, M. B.: Linearised solution of a free-surface flow over a trapezoideal obstacle, *Acta Mech.* **78**, 219-233 (1989).

[22] Forbes, L. K.: Free-surface flow over a semicircular obstruction, including the influence of gravity and surface tension, *J. Fluid Mech.* **127**, 283-297 (1983).

[23] Forbes, L. K.: Critical free-surface flow over a semi-circular obstruction, *J. Eng. Math.* **22**, 3-13 (1988).

[24] Forbes, L. K.: Non-linear, drag-free flow over a submerged semi-elliptical body, *J. Eng. Math.* **16**, 171-180 (1982).

[25] Forbes, L. K.: On the wave resistance of a submerged semi-elliptical body, *J. Eng. Math.* **15**, 287-298 (1981).

[26] Forbes, L. K.: Two-layer critical flow over a semi-circular obstruction, *J. Eng. Math.* **23**(4), 325-342 (1989).

[27] Forbes, L. K., Schwartz, L. W.: Free-surface flow over a semicircular obstruction, *J. Fluid Mech.* **114**, 299-314 (1982).

[28] Fornberg, B.: *A Practical Guide to Pseudospectral Methods*, Cambridge University Press, New York, 1998.

[29] Goh, K. H. M., Tuck, E. O.: Thick waterfalls from horizontal slots, *J. Eng. Math.* **19**, 341-349 (1985).

[30] Gong, L., Shen, S. S. P.: Non-linear, multiple supercritical solitary waves solutions of the stationary forced Korteweg-de Vries equation and their stability, *SIAM J. Appl. Math.* **54**(5), 1268-1290 (1994).

[31] Grandison, S., Vanden-Broeck, J.-M.: Truncation approximations for gravity-capillary free-surface flows, *J. Eng. Math.* **54**, 89-97 (2006).

[32] Grimshaw, R. H. J., Chan, K. H., Chow, K. W.: Transcritical flow of a stratified fluid: the forced extended Korteweg-de Vries modely, *Phys. Fluids* **14**(2), 755-774 (2002).

[33] Grimshaw, R. H. J., Smyth, N.: Resonant flow of a stratified fluid over topography, *J. Fluid Mech.* **169**, 429-464 (1986).

[34] Gyüre, B., Jánosi, I. M.: Stratified flow over asymmetric and double bell-shaped obstacles, *Dyn. Atmos. Oceans* **37**, 155-170 (2003).

[35] Hanna, S. N.: Free-surface flow over a polygonal and smooth topography, *Acta Mech.* **100**, 241-251 (1993).

[36] Hanna, S. N., Abdel-Malek, M. N., Abd-el-Malek, M. B.: Super-critical free-surface flow over a trapezoidal obstacle, *J. Comput. Appl. Math.* **66**, 279-291 (1996).

[37] Higgins, P. J., Belward, S. R., Read, W. W.: Optimising series solution methods for flow over topography - Part 1, *ANZIAM J.* **46**(E), C1272-C1285 (2005).

[38] Higgins, P. J., Read, W. W., Belward, S. R.: A series solution method for free-boundary problems arising from flow over topography, *J. Eng. Math.* **54**, 345-358 (2006).

[39] Hocking, G. C., Vanden-Broeck, J.-M.: Draining of a fluid of finite depth into a vertical slot, *Appl. Math. Modelling* **21**, 643-649 (1997).

[40] Holmås, H., Clamond, D., Langtangen, H. P.: A pseudospectral Fourier method for a 1D incompressible two-fluid model, *Int. J. Numer. Math. Fluids* **58**, 639-658 (2008).

[41] Jiang, L., Lin, H.-J., Schultz, W. W.: Unsteady ripple generation on steep gravity-capillary waves, *J. Fluid Mech.* **386**, 281-304 (1999).

[42] Lamb, H.: *Hydrodynamics*, 4th ed., Cambridge University Press, London, 1932.

[43] Lane-serff, G. F., Beal, L. M., Hadfield, T. D.: Gravity current flow over obstacles, *J. Fluid Mech.* **292**, 39-53 (1995).

[44] Lee, S. J., Yates, G. T., Wu, T. Y.: Experiments and analyses of upstream - advancing solitary waves generated by moving disturbances, *J. Fluid Mech.* **199**, 569-593 (1989).

[45] Li, Y. A., Hyman, J. M., Choi, W.: A numerical study of the exact evolution equations for surface waves in water of finite depth, *Stud. Appl. Maths* **113**, 303-324 (2004).

[46] Lowery, K., Liapis, S.: Free-surface flow over a semi-circular obstruction, *Int. J. Numer. Math. Fluids* **30**, 43-63 (1999).

[47] Milewski, P. A.: A formulation for water waves over topography, *Stud. Appl. Maths* **100**, 95-106 (1998).

[48] Milewski, P. A.: The forced Korteweg-de Vries equation as a model for waves generated by topography, *CUBO* **6**(4), 33-51 (2004).

[49] Milewski, P. A., Tabak, E. G.: A pseudospectral procedure for the solution of nonlinear wave equations with examples from free-surface flows, *SIAM J. Sci. Comput.* **21**(3), 1102-1114 (1999).

[50] Milewski, P. A., Vanden-Broeck, J.-M.: Time dependent gravity-capillary flows past an obstacle, *Wave Motion* **29**, 63 - 79 (1999).

[51] Nadiga, B. T., Margolin, L. G., Smolarkiewicz, P. K.: Different approximations of shallow fluid flow over an obstacle, *Phys. Fluids* **8**(8), 2066-2077 (1996).

[52] Naghdi, P. M., Vongsarnpigoon, L.: The downstream flow beyond an obstacle, *J. Fluid Mech.* **162**, 223-236 (1986).

[53] Perlin, M., Schultz, W. W.: Capillary effects on surface waves, *Annu. rev. Fluid Mech.* **32**, 241-274 (2000).

[54] Pratt, L. J.: On nonlinear flow with multiple obstructions, *J. Atmos. Sci.* **41**, 1214-1225 (1984).

[55] Shen, S. S.-P.: On the accuracy of the stationary forced Korteweg-de Vries equation as a model equation for flows over a bump, *Q. Appl. Math.* **53**, 701-719 (1995).

[56] Shen, S. S.-P., Shen, M. C.: Notes on the limit of subcritical free-surface flow over an obstruction, *Acta Mech.* **82**, 225-230 (1990).

[57] Shen, S. S.-P., Shen, M. C., Sun, S. M.: A model equation for steady surface waves over a bump, *J. Eng. Math.* **23**(4), 315-323 (1989).

[58] Tooley, S., Vanden-Broeck, J.-M.: Waves and singularities in nonlinear capillary free-surface flows, *J. Eng. Math.* **43**, 89-99 (2002).

[59] Vanden-Broeck, J.-M.: Elevation solitary waves with surface tension, *Phys. Fluids A* **3**(11), 2659-2663 (1991).

[60] Vanden-Broeck, J.-M.: Free-surface flow over an obstruction in a channel, *Phys. Fluids* **30**(8), 2315-2317 (1987).

[61] Vanden-Broeck, J.-M.: Numerical calculations of the free-surface flow under a sluice gate, *J. Fluid Mech.* **330**, 339-347 (1997).

[62] Vanden-Broeck, J.-M.: Wilton ripples generated by a moving pressure distribution, *J. Fluid Mech.* **451**, 193-201 (2002).

[63] Wen, X., Manik, K.: A boundary integral method for gravitational fluid flow over a semi-cricular obstruction using an interpolative technique, *Engng. Anal. Boundary Elem.* **24**, 31-41 (2000).

[64] Wu, T. Y.: Generation of upstream advancing solitons by moving disturbances, *J. Fluid Mech.* **184**, 75-99 (1987).

[65] Zeytounian, R. Kh.: Nonlinear long waves on water and solitons, *Physics of our days* **38**(12), 1333-1382 (1995).

[66] Zhang, Y., Zhu, S.: Open channel flow past a bottom obstruction, *J. Eng. Math.* **30**, 487-499 (1996).

[67] Zhu, S., Zhang, Y.: On nonlinear transient free-surface flows over a bottom obstruction, *Phys. Fluids* **9**(9), 2598-2604 (1997).

[68] Zhu, Y.: Resonant flow of a fluid past a concave topography, *Appl. Math. Mech.* **18**(5), 479-482 (1997).

APPENDIX

APPENDIX

Monacella (1961) proved that a singularity in the Cauchy principal value integrals can be ignored in the numerical integration. This is achieved by spacing the mesh points symmetrically with respect to the pole. We show here by using the trapezoidal rule to compute the Cauchy principal value integral. We can also use the Simpson's rule to approximate such integral.

Let f be a continuous function. We approximate the integral of f over a finite interval $[a, b]$ by partitioning $[a, b]$ into N subintervals with $t_0 = a$ and $t_N = b$. Thus

$$\int_a^b f(t)dt \approx \sum_{i=0}^N f(t_i)hw_i. \tag{A.1}$$

Here $h = \frac{b-a}{N}$ and

$$w_i = \begin{cases} \frac{1}{2} & , i = 0 \text{ and } N \\ 1 & , \text{otherwise.} \end{cases} \tag{A.2}$$

We consider a function $\frac{f(t)}{t-x}$ with $f(x) \neq 0$ and $x \in (a, b)$. The integral of $\frac{f(t)}{t-x}$ over the variable t is of Cauchy principal value form. For any $\epsilon > 0$, we can write this integral as

$$\int_a^b \frac{f(t)}{t-x}dt = \lim_{\epsilon \to 0} \left[\int_a^{x-\epsilon} \frac{f(t)}{t-x}dt + \int_{x+\epsilon}^b \frac{f(t)}{t-x}dt \right]. \tag{A.3}$$

To compute this integral, we rewrite the integral on the left hand side of (A.3) as

$$\int_a^b \frac{f(t)}{t-x}dt = \int_a^b \frac{f(t) - f(x)}{t-x}dt + f(x) \int_a^b \frac{1}{t-x}dt. \tag{A.4}$$

Next we consider $N + 1$ equally spaced mesh point $t_i, i = 0, \ldots, N$. Thus x is the midpoint between t_i and t_{i+1} for $i = 0, 1, \ldots, N - 1$. There are two possible cases to be taken into account: (i) $x = \frac{b-a}{2}$ and (ii) $x \neq \frac{b-a}{2}$.

Case (i) $x = \frac{b-a}{2}$.

It can easily be shown that $\int_a^b \frac{1}{t-x}dt = 0$. Thus (A.4) becomes

$$\int_a^b \frac{f(t)}{t-x}dt = \int_a^b \frac{f(t)-f(x)}{t-x}dt. \qquad (A.5)$$

Using the trapezoidal rule, we approximate the integral on the right hand side of (A.5) by

$$\int_a^b \frac{f(t)}{t-x}dt \approx \sum_{i=0}^N \frac{f(t_i)-f(x)}{t_i-x}hw_i$$
$$= \sum_{i=0}^N \frac{f(t_i)}{t_i-x}hw_i - f(x)\sum_{i=0}^N \frac{1}{t_i-x}hw_i$$
$$= \sum_{i=0}^N \frac{f(t_i)}{t_i-x}hw_i. \qquad (A.6)$$

$\sum_{i=0}^N \frac{1}{t_i-x}hw_i = 0$ because x is midpoint of the interval $[a,b]$. Equation (A.6) suggests that the Cauchy principal value integral can be approximated as if it were an ordinary integral.

Case (ii) $x \neq \frac{b-a}{2}$.

Assuming that x is a midpoint on any interval $[c,d] \subset [a,b]$. We now rewrite (A.3) as

$$\int_a^b \frac{f(t)}{t-x}dt = \int_a^c \frac{f(t)}{t-x}dt + \int_c^d \frac{f(t)}{t-x}dt + \int_d^b \frac{f(t)}{t-x}dt. \qquad (A.7)$$

The first and third integrals on the right hand side of (A.7) are not Cauchy principal values. Thus they can be approximated by trapezoidal rule. The second integral is a Cauchy principal value with x as a midpoint of the interval $[c,d]$. The discussion in case (i) shows that it can also be evaluated by the trapezoidal rule. Therefore

$$\int_a^b \frac{f(t)}{t-x}dt \approx \sum_{i=0}^N \frac{f(t_i)}{t_i-x}hw_i$$

Which is the same as (A.6). Thus, the singularity is subtracted from the Cauchy principal value integral leaving nonsingular integrals to evaluate as claimed.

VITA

Acting Lt. Panat Guayjarernpanishk was born on February 16, 1976 in Ubonratchathani, Thailand. He received a Bachelor of Science in Mathematics (2nd Class Degree Honours) from Department of Mathematics, Faculty of Science, Chaing Mai University in 1996 and a Master of Science in Computational Science from Department of Mathematics, Faculty of Science, Chulalongkorn University in 2003. He had worked for four years at Faculty of Science, Ubonratchathani University before he started of master at Chulalongkron University and by the University Development Commission (U.D.C.) Scholarship. He is interested in numerical analysis and computational fluid dynamics related to the free-surface flow problems.